The Dissertation Committee for Omar Dario Lopez Mejia
certifies that this is the approved version of the following dissertation:

Computational Study of a NACA4415 airfoil using synthetic jet control

Committee:

Robert D. Moser, Supervisor

David Bogard

Ofodike Ezekoye

Venkatramanan Raman

Robert Bishop

Computational Study of a NACA4415 airfoil using synthetic jet control

by

Omar Dario Lopez Mejia, B.S.; M.S.

DISSERTATION

Presented to the Faculty of the Graduate School of

The University of Texas at Austin

in Partial Fulfillment

of the Requirements

for the Degree of

DOCTOR OF PHILOSOPHY

THE UNIVERSITY OF TEXAS AT AUSTIN

May 2009

Dedicated to my parents and my wife Monica.

Acknowledgments

Computational Study of a NACA4415 airfoil using synthetic jet control

Publication No. ⎯⎯⎯⎯⎯⎯⎯

Omar Dario Lopez Mejia, Ph.D.
The University of Texas at Austin, 2009

Supervisor: Robert D. Moser

Synthetic jet actuators for flow control applications have been an active topic of experimental research since the 90's. Numerical simulations have become an important complement of that experimental work, providing detailed information of the dynamics of the controlled flow. This study is part of the AVOCET (Adaptive VOrticity Control Enabled flighT) project and is intended to provide computational support for the design and evaluation of closed-loop flow control with synthetic jet actuators for small scale Unmanned Aerial Vehicles (UAVs). The main objective is to analyze active flow control of a NACA4415 airfoil with tangential synthetic jets via computational modeling. A hybrid Reynolds-Averaged Navier-Stokes/Large Eddy Simulation (RANS/LES) turbulent model (called Delayed Detached-Eddy Simulation-DDES) was implemented in CDP, a kinetic energy conserving Computational Fluid Dynamics (CFD) code. CDP is a parallel unstructured grid incompressible flow solver, developed at the Center for Integrated Turbulence Simulations (CITS) at Stanford University.

Two models of synthetic jet actuators have been developed and validated. The first is a detailed model in which the flow in and out of the actuator cavity is modeled. A second less costly model (RSSJ) was also developed in which the Reynolds stress produced by the actuator is modeled, based on information from the detailed model. Several static validation test cases at different angle of attack with modified NACA 4415 and Dragon Eye airfoils were performed. Numerical results show the effects of the actuators on the vortical structure of the flow, as well as on the aerodynamic properties. The main effect of the actuation on the time averaged vorticity field is a bending of the separation shear layer from the actuator toward the airfoil surface, resulting in changes in the aerodynamic properties. Full actuation of the suction side actuator reduces the pitching moment and increases the lift force, while the pressure side actuator increases the pitching moment and reduces the lift force. These observations are in agreement with experimental results. The effectiveness of the actuator is measured by the change in the aerodynamic properties of the airfoil in particular the lift (ΔC_l) and moment (ΔC_m) coefficients. Computational results for the actuator effectiveness show very good agreement with the experimental values (over the range of $-2°$ to $10°$). While the actuation modifies the global pressure distribution, the most pronounced effects are near the trailing edge in which a spike in the pressure coefficient (C_p) is observed. The local reduction of C_p, for both the suction side and pressure side actuators, at $\frac{x}{c} = 0.96$ (the position of the actuators) is about 0.9 with respect to the unactuated case. This local reduction of the pressure is associated with the trapped vorticity and flow acceleration close to the trailing edge.

The RSSJ model is designed to capture the synthetic jet time averaged be-

havior so that the high actuation frequencies are eliminated. This allows the time step to be increased by a factor of 5. This ad hoc model is also tested in dynamic simulations, in which its capacity to capture the detail model average performance was demonstrated. Finally, the RSSJ model was extended to a different airfoil profile (Dragon Eye) with good results.

Table of Contents

List of Tables

List of Figures

xviii

xix

Nomenclature

α Angle of attack in degrees

$\bar{\Delta p}$ Δp moving average

β NS discretization parameter (convective term)

ΔC_l Actuator effectiveness based on lift coefficient

ΔC_m Actuator effectiveness based on moment coefficient

ΔC_p Pressure coefficient increment at synthetic jet outlet

Δp Change of pressure along the actuator ramp

Δ LES filter

δ Boundary layer thickness

Δ_o Characteristic mesh size in LES region

ϵ Solid and wake blockage correction parameter

η Wall interference correction parameter

γ NS discretization parameter (convective term)

Γ_i RSSJ model numerical parameter (strength)

$\hat{t}$ Moving average time constant

κ Karman constant

λ_i RSSJ model numerical parameter (size)

ν Molecular viscosity

ν_t Eddy viscosity

Ω Actuation frequency

ω_i RSSJ model numerical parameter (size)

$\overline{P}$ Averaged or filtered pressure field

$\overline{U_i}$ Averaged or filtered velocity field

Φ NS discretization parameter (convective term)

ψ NS discretization parameter (diffusive term)

σ Turbulent Prandtl number

τ_{ij} Reynolds stress tensor (RANS) or SubGrid-Scale stress tensor (LES)

θ_i RSSJ model numerical parameter (orientation)

$\tilde{\nu}$ Spalart-Allmaras model variable

$\tilde{U}$ Time and spatial averaged synthetic jet outlet velocity

ξ Solid and wake blockage correction parameter

ζ Infinite aspect ratio correction parameter

A Boundary condition amplitude (detail model)

A_f Face area used in NS discretization

A_{jet} Synthetic jet outlet area

A_{pf} Airfoil plan form area

C Wind tunnel sectional test area

c Airfoil chord

C_d Drag coefficient

C_l Lift coefficient

C_m Moment coefficient

C_p Pressure coefficient

C_μ Momentum coefficient

d Distance to the wall

F^+ Non-dimensional frequency of actuation or actuation Strouhal number based on the chord

F_h^+ Actuation Strouhal number based on the synthetic jet slot height

f_{shed} Shedding frequency

h Synthetic jet lot height

Ma Mach number

Re Reynolds number based on c

S Strain rate magnitude

S_t Vortex shedding Strouhal number based on the chord

T Nondimensional time $\left(\frac{tU_\infty}{c}\right)$

t Time

U_∞ Free stream velocity

U_{rms} RMS velocity at the synthetic jet outlet

x x coordinate

X_i RSSJ model numerical parameter (x location)

y y coordinate

Y_i RSSJ model numerical parameter (y location)

z z or spanwise coordinate

CDP   Computational Fluid Dynamics code

CFD   Computational Fluid Dynamics

CFL   Courant-Friedrich-Lewis number

JS   Jet Strength

LES   Large Eddy Simulation

PIV   Particle Image Velocimeter

PS   Pressure side of the airfoil

RANS   Reynolds Averaged Navier-Stokes

RSSJ   Reynolds Stress Synthetic Jet model

SS   Suction side of the airfoil

Chapter 1

Introduction

During the last decade, there has been a growing interest in small active flow control devices that affect the flow field and modify forces and moments over lifting surface, particularly for low-Reynolds number applications such as Unmanned Aerial Vehicles (UAV). Extensive experimental work has demonstrated that the synthetic jet actuators are an effective way to modify the aerodynamic properties of a lifting surface by manipulating the vorticity near the trailing edge[38][37][36][35], giving the potential to replace conventional control surfaces such as flaps, spoilers and deflectors[4]. An Air Force-funded Multidisciplinary University Research Initiative (MURI) project called AVOCET (Adaptive VOrticity Control Enabled flighT) was initiated to develop a closed-loop flow control system using synthetic jet actuators for maneuvering small scale UAVs. The research reported in this dissertation was undertaken as part of the AVOCET project to develop computational models of flow over a lifting surface controlled by such actuators. Such models are needed to provide detailed data for the development of reduced order models (ROM's) for use in the controller and to analyze the characteristics of the controlled flow. Below is a brief overview of flow control, synthetic jets and the avocet project.

1.1 Flow Control

1.1.1 Definition and classification

Flow control is simply a process to modify a flow field by some external means to meet some objective. A variety of methods can be used to achieve different effects such as: delay or promote transition to turbulence, prevent or induce separation; or suppress or enhance turbulence[45]. Common flow control goals include drag reduction, lift enhancement, mixing improvement and noise suppression. These goals need not be mutually exclusive but in many cases, pursuing one goal can compromise another[44].

Flow control can be classified in two broad categories: passive and active [44][45]. Passive flow control does not require energy to drive an actuator while active flow control an energy input is required. Passive flow control generally involves geometry modifications to achieve a goal. For example, Large-eddy breakup devices (LEBU)[58], riblets [131] and wavy walls have been proposed for drag reduction. More details about these passive techniques can be found on references [44] and [57]. In low-Reynolds-number aerodynamics, modifications of airfoil geometries (e.g: reshaping, turbulators, blunt trailing edges and wavy leading edges) are commonly employed to control separation and lift enhancement[39][5]. Active flow control techniques can be further subdivided into predetermined (open-loop) and reactive flow control [44]. In predetermined active control actuators operate without regard of the state of the flow, thus no sensors are needed. An example of this type of control is circulation control of wings, in which lift enhancement is achieved by blowing a jet over a rounded trailing edge creating a coanda effect and changing the airfoil Kutta condition[68][41][42]. In

reactive flow control, the actuators are controlled based on information from sensors. The control loop in a reactive technique can be open-loop or closed-loop and most flow control applications use the latter. The research described here involves predetermined active flow control, but the AVOCET project is primarily concerned with reactive flow control technique. Jee et al [66] have already used the implementation developed here to perform numerical simulations of a controlled airfoil.

1.1.2 History and role of CFD in flow control

The origin of flow control is associated with the origins of the boundary layer theory attributed to Ludwig Prandtl in 1904. He was able to show the influence of suction on the delay of boundary layer separation[93]. His research thus began the development of theory based flow control. In 1910, Henry Coanda discovered the coanda effect which was later the base of circulation control[93]. During and after world war II (1940-1970) passive and active control were mainly focused on laminar flow control and polymer drag reduction[44]. During this period it was also shown that blowing and suction on an airfoil surface can affect the pressure distribution over the airfoil, through addition/removal of momentum to/from the boundary layer. From 1950 to 1970, flow control research on aerodynamic applications such as: suction-type laminar-flow control [12] and circulation control (based on the coanda effect) [68] was active. Between 1970-1990, drag reduction was the focus of flow control research, for example: Large-Eddy Breakup Devices (LEBU) and riblets were widely investigated during this period[58][60]. Since 1990 active flow control to manipulate coherent structures in turbulent and transitional flow has been actively pursued.

Micro-ElectroMechanical Systems (MEMS), surface plasmas and new control algorithms (such as neural networks and genetic algorithms) are playing important roles in the improvement and progress of flow control techniques[44][45]. One application in which flow control appears to be very attractive is the modification of aerodynamic properties of airfoils using microsurface effectors and fluid devices such as synthetic jets. Practical implementation of such control applications is complemented by the development of experimental control systems (open and closed-loop) for flight vehicles.

Numerical and computational tools have been extensively used recently for flow control simulation due to increases in computer speed and storage capacity[45][50]. Computational Fluid Dynamics (CFD) can provide insight in to physics of the controlled flow that is difficult to obtain from experiments. Experimental measurements and CFD are thus complementary, and the use of both can speed the development of flow control techniques in real applications. In most aeronautical flow control applications, including the UAV application pursued here, the flows involved are turbulent, requiring that CFD application to flow control employ a turbulent treatment. In the last 20 years Direct Numerical Simulations (DNS), Large-Eddy Simulations (LES) and Reynolds Averaged Navier Stokes (RANS) turbulent treatments have been used extensively in such applications, for both wall-bounded and external flows. RANS is the predominant turbulence model approach, but use of LES and DNS has been increasing[100][50]. For example, DNS has been used to study the influence of riblets in turbulent flow [24] and active flow control in wall bounded flows [25]. A big effort in flow control CFD has been focused on active flow control applications that involve

blowing (steady and unsteady), suction or both (as in synthetic jets) in external flows (especially around airfoils) [61] [129] [50] [100]. In recent years, CFD has played an important role in flow control problem of low-Reynolds number aerodynamic applications like Unmanned Aerial Vehicles (UAV). The majority of the CFD research in low-Reynolds number applications is towards separation control at high angle of attack [61] [40] [117] [133] so that little work has been done towards the simulation control to modify aerodynamic properties [129] and commanded maneuvers such as pitching or plunging at low angle of attack. That is the area in which this numerical study is focused, also contributing to the application of CFD to low-Reynolds number aerodynamics.

1.2 Synthetic Jet Actuators

1.2.1 Definition and applications

A synthetic jet actuator is a zero-net mass-flux device that alternately injects and removes fluid through a small orifice or slot at a given frequency. Figure 1.1[1] shows a schematic of a typical synthetic jet actuator. It is basically a cavity sealed by a diaphragm, with a small orifice on one side forming what is commonly called a Helmholtz resonator [59]. The diaphragm is normally driven by a piezoelectric actuator but it can also be driven by electromechanical or even just mechanical devices depending on the actuation frequency[101][48]. When the piezoelectric actuator is excited with an alternating voltage, it makes the diaphragm oscillate and consequently, fluid is periodically entrained into and ejected from the cavity. During the outflow, as

---

[1]`http://www.img.ufl.edu/projectfiles/SynJet.gif`
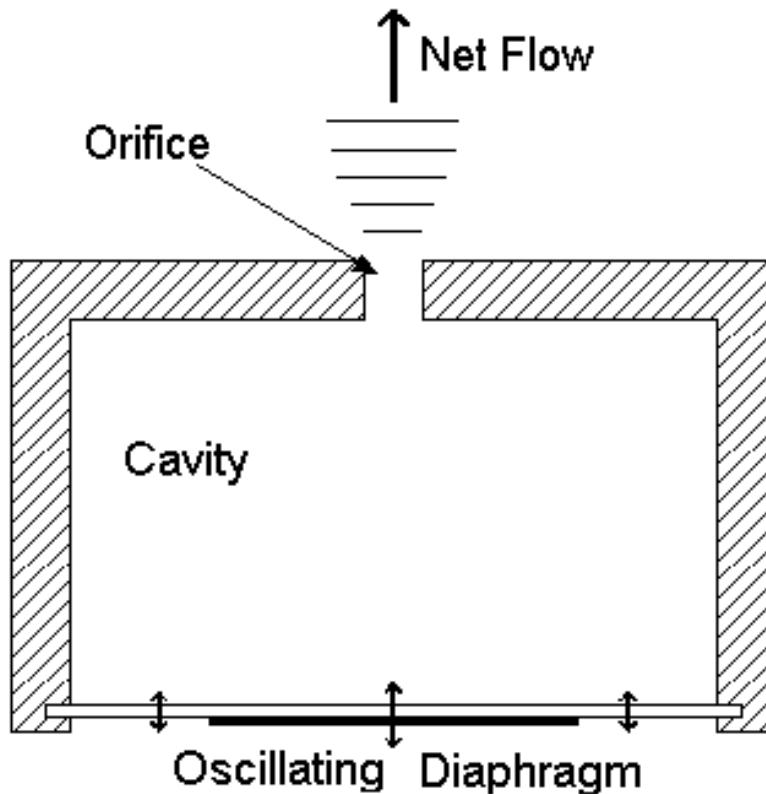
Figure 1.1: Schematic of a synthetic jet actuator

the fluid is expelled through the orifice, the flow separates and creates vortex sheets that roll up into vortices [101]. These vortices can be convected in to the external flow far away from the synthetic jet orifice, if the strength of the jet (determined by amplitude and frequency) is high enough, otherwise the vortices are ingested back into the synthetic jet cavity [59]. Thus, when the strength is high enough, the net momentum flux through in the jet is not zero though the net mass flux is identically zero. A jet is then synthesized due to the entrainment of fluid from the external environment[110].

The discovery and first application of synthetic jet actuators in engineering was in 1953 by Ingard, who applied it to acoustic problems[63]. During the 50's, research on synthetic jets was focused on performance and not on applications in different external flows[48]. It was not until the 90's that a variety of synthetic jet applications were studied. One of the first applications was the interaction of a synthetic jet with different types of flows[111]. Synthetic jets actuators have also been used in flow control applications such as separation control [28] [15], small scale control of turbulence [130], mixing [23] and heat transfer enhancement [10]. One relevant application of synthetic jet actuators related to this dissertation is the modification of aerodynamic characteristics of bluff bodies and airfoils [3] [90]. A synthetic jet actuator placed on a lifting surface is capable of modifying the streamlines around a body, as if the shape had been modified, making the synthetic jet useful for the manipulation of the aerodynamic properties of a body. Dr Glezer's group at Georgia Tech has shown that synthetic jet actuators are an effective way to enhance the lift and modify the moments of wings and airfoils [38]. Effective control has been achieved with actuation frequencies an order of magnitude larger than the natural shedding frequency of the body [4].

1.2.2 Simulation and models

Numerical and computational tools have been used extensively for the simulation and modeling of synthetic jets and synthetic jet applications [73] [59] [83] [100] [61] [129]. The numerical simulation of synthetic jets is still an active research field in particular because of the wide range of spatial and temporal scales involved

in such a simulation. For example, a synthetic jet orifice diameter or slot width is normally $O(10^{-2})$ to $O(10^{-4})$ times the characteristic length scale of the flow while the actuation period for effective control is $O(10^{-1})$ times the convective time scale or smaller, which would be $O(10^{-4})$ of the maneuvering time scale in a typical UAV application. Several types of models of synthetic jets can be used in simulations of controlled flow: detailed models, reduced-order models or a simple periodic surface boundary condition. A detailed model resolves all the spatial and temporal scales of the synthetic jet actuator, and are normally fully three dimensional, though they can be simplified to two dimensions. In such models the flow in the synthetic jet cavity is included in the computational domain, and the actuation frequency is resolved temporally, making it expensive. Nevertheless, this is one of the most used synthetic jet models[100][59]. Reduced-order models (ROM) simplify the physics of the synthetic jet actuator (reducing the complexity of the simulation) and are suitable for flow control applications. Examples include: discrete vortex models [125], lumped element models (LEM)[46] and Euler [132] or Bernoulli [105] solvers inside the cavity. Finally, a simple periodic surface boundary condition model is simply the application of a periodic inlet/outlet boundary condition at the synthetic jet outlet, without representing the details of the cavity [83]. Though this model is attractive, it is highly dependent on the details of the imposed velocity profile at the synthetic jet outlet.

One of the important characteristics of synthetic jet actuators used in this numerical study, is the fact that they are tangential. The majority of experimental and computational studies on synthetic jets deal with normal actuators with the

Model	Advantages	Disadvantages
Detailed	Fully captures the dynamics of the synthetic jet actuator.	Increase the complexity of the simulation (geometry and boundary conditions). Time stepping limited by the synthetic jet frequency (expensive).
Low-order	Reduce the complexity of the simulation. Time stepping limited by stability/accuracy	Highly dependent on the interaction with the wall and the cross flow.
Simple periodic surface BC	Simple to implement.	Time stepping limited by the synthetic jet frequency (expensive). Requires a priori detailed knowledge of the velocity profile at the SJ outlet. Fails to capture the complex flow and vorticity field close to the SJ outlet.

Table 1.1: Synthetic jet models

exception of studies related to circulation control of airfoils [68]. The simulation and modeling of a tangential synthetic jet implies an extra difficulty since such a model would be highly dependent on modeling the interaction with the wall and with the cross flow [125]. Table 1.1 summarizes the advantages and disadvantages (in the context of the current study) of the different synthetic jet models used by the CFD community.

1.3   AVOCET project

The research reported here is part of the AVOCET (Adaptive VOrticity Control Enabled flighT) project[2] which is sponsored by the Air Force Office of Scientific Research (AFOSR) under the Multidisciplinary University Research Initiative (MURI). The main objective of the AVOCET project is to design and build a closed-loop flow control system using synthetic jet actuators for flight maneuvering small scale Unmanned Aerial Vehicles (UAVs).

Experimental and theoretical approaches are employed to achieve AVOCET objectives. Controlling the synthetic jet requires an adaptive control architecture with a closed-loop feedback from pressure and flow direction sensors mounted on the UAVs surface. Experimental work is focused on the design and implementation of this architecture, in the design and construction of micro sensors and on wind tunnel/flight experiments which are being pursued at Georgia Tech. This adaptive control architecture uses the forces and moments acting over the airfoil and a low order model for purposes of feedback design[89]. Wind tunnel and flight experiments will provide the dynamic evolution of the forces and moments during dynamic tests with and without controlled actuation. One important aspect that the experiments address is the study of the strong coupling between the vehicle and the flow dynamics during dynamic maneuvers, so that the dynamics of the controlled flow is affected by the airfoil (rigid body) dynamics [89]. A low order model is required as a reference model in the design and implementation of the closed-loop controller. Two different low-

---

[2]`http://www.avocet.gatech.edu/`

order models are being developed: one based on discrete-vortex (pursued at California Institute of Technology) and the other is based on Proper Orthogonal Decomposition (pursued at the University of Illinois at Urbana-Champaign) [122] [9]. This is one of the first studies in which closed-loop flow control is designed based on flow physics rather than experience or intuition[122].

Another component of the AVOCET project is high-fidelity models based on CFD simulation, which can provide detailed information on the physics and response of the flow being controlled. CFD simulations address several important aspects of the AVOCET development such as: it supports the experimental work (both wind tunnel and fight tests) by providing details of the controlled flow that can not be observed directly from experimental techniques; it provides detailed three dimensional flow field data and integral quantities relevant to the low-order model design and calibration; it serves as a test for controller development; and, it helps in the refinement of sensor and actuator placement. This is the framework in which the research described here was undertaken.

1.4   Objectives

The aim of this dissertation is to analyze active flow control of a NACA4415 airfoil with tangential synthetic jets via numerical modeling. Achieving this primary objective implies several secondary objectives and challenges such as:

- Development of integrated CFD tools for flow control.

- Implementation of a hybrid RANS-LES model in a state of the art parallel

unstructured grid incompressible Navier-Stokes solver (CFD code).

- Development of hybrid grids that satisfy the requirements of the turbulence model.

- Development and implementation of synthetic jet models.

- Validation of CFD and synthetic jet models with available experimental data.

- Analysis of the phenomenological effects of tangential synthetic jets on the flow field and on the aerodynamic properties.

- Tests of the synthetic jet models on a moving airfoil and on a second airfoil geometry being used in the experiments: the Dragon Eye airfoil.

1.5   Dissertation layout

The remainder of this dissertation is organized as follows: Chapter 2 provides an overview of the experimental set-up at Georgia-Tech including the characteristics of the wind tunnel, a complete description of the hardware used to simulate flight maneuvers in the wind tunnel and a description of the airfoil model and the tangential synthetic jets used. Details of simulation approach, techniques and models used in this research are given in chapter 3. Numerical results for the different simulations performed are included in chapter 4, including validation and calibration of the synthetic jet models, and evaluation of a proposed new model, the Reynolds Stress Synthetic Jet Model. Finally, conclusions and future work are summarized in chapter 5. Appendices give supplemental information such as: discretization details of the

CFD code, script file for grid generation and numerical parameters for the synthetic jet model implementation.

Chapter 2

Experimental background information

This chapter provides insight into the experimental research done at Georgia Tech, which is the basis for the problem this dissertation is modeling. Initially a brief description of the hardware used in the experimental set up is presented. Then important aspects of the modified NACA4415 model are shown, finally some details of the synthetic jet actuators used in the experiments are given.

2.1 Experimental Set-up

This computational study complements the experimental study being pursued at Georgia Tech, with the models developed here designed to simulate the experimental configuration. The facility consists of an open-return low-speed wind tunnel with a square test section of $1m \times 1m$ with wind speed up to $30m/s$ [15]. Experiments are conducted in this wind tunnel with a modified NACA4415 two-dimensional airfoil model. Since the primary objective of this facility is to simulate free flight in the wind tunnel, the airfoil model is mounted on a traverse structure that allows the model to have three degrees of freedom i.e. pitch, plunge and roll. Figure 2.1[1] shows a CAD layout of the traverse mechanism, showing the important elements.

---

[1]Courtesy of Brzozowski and Muse (GA Tech)
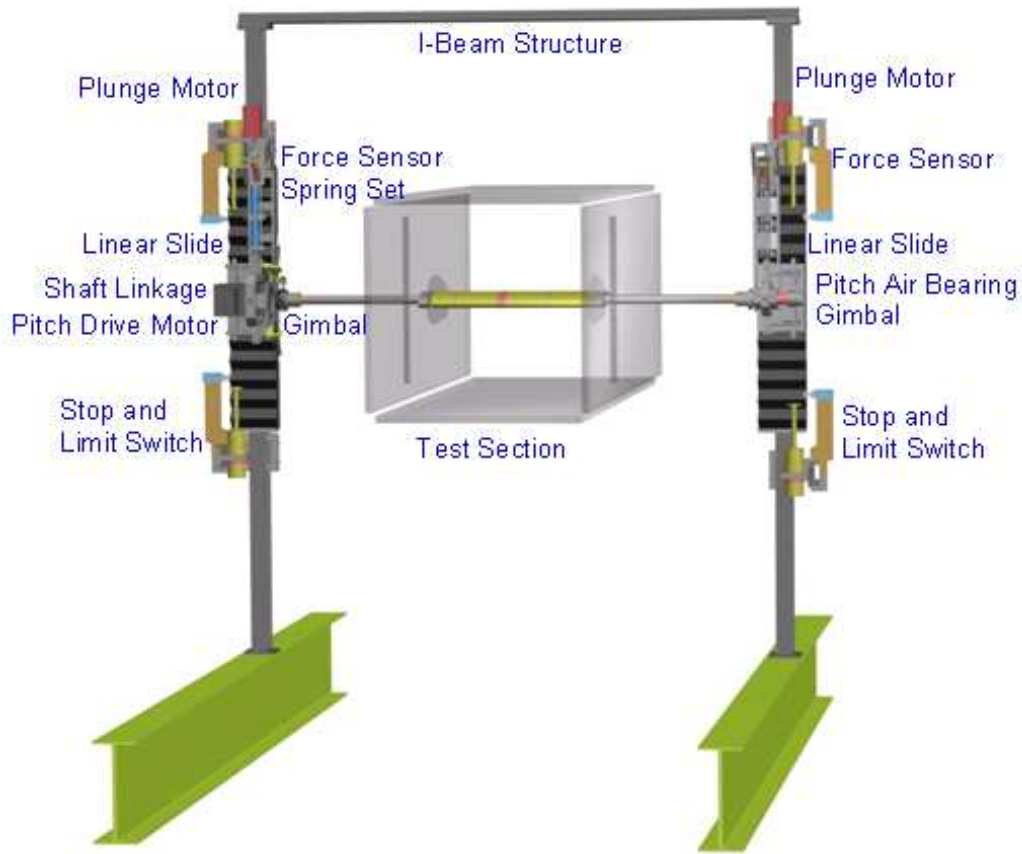
Figure 2.1: Layout of the 3-DOF traverse structure used in the experimental set-up.

The motion of the airfoil on the traverse is controlled by a dedicated feedback controller. The pitching motion is controlled using a servo motor that is connected to the airfoil through a shaft. The servo motor also works as a moment transducer to indirectly measure the aerodynamic moment[74]. Plunging and rolling is achieved by two linear slides mounted on each side of the test section. Plunging is executed by synchronizing the vertical motion of the two slides, while rolling is achieved by independent motion of the slides [89]. The force sensor shown in Figure 2.1 measures

15

Figure 2.2: Experimental set-up.

the vertical forces that act on the model and are used to indirectly measure the lift[17]. Figure 2.2[2] shows a picture of the assembly used in the experiments, with the elements described above evident.

This traverse system is driven by a feedback controller designed and implemented by Dr Calise's group at GA Tech and, though the objective of this dissertation does not include dynamic simulations with the controller, it is briefly described here for context. For a 2-DOF motion the entire control system consists of three basic

---

[2]Courtesy of Brzozowski and Muse (GA Tech)
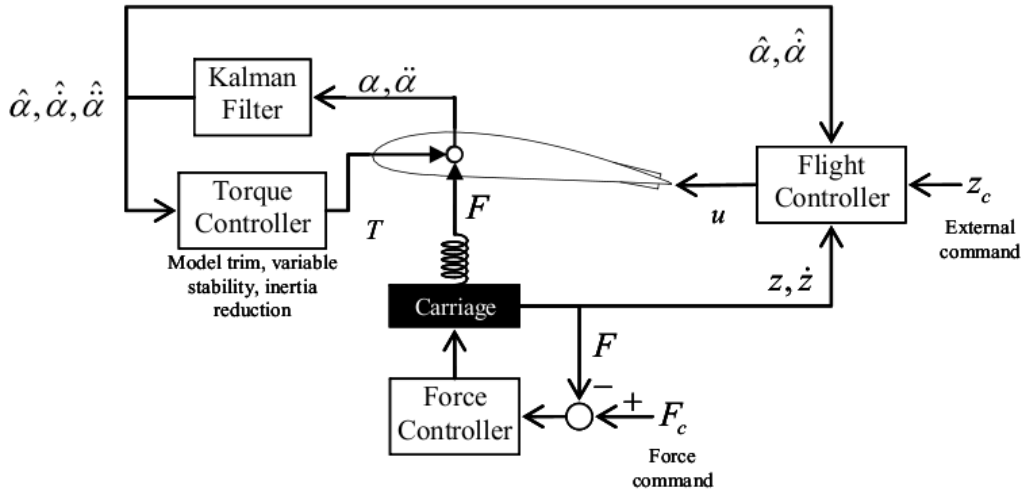
Figure 2.3: Controller architecture for experimental set-up

parts (see Figure 2.3[3]): torque, force and flight controllers. As described by Muse et al [89], the torque controller (also known as inner controller) is a PID controller in series with a linear dynamic compensator. The inner controller regulates the pitching motion of the airfoil by means of the servomotor. The force controller operates in the plunging maneuvers and is responsible of simulating the vertical free flight of the model by compensating for the weight of the model [17]. Finally, the flight controller (also known as the outer loop controller) regulates the plunge and pitch of the airfoil in a similar way to a conventional flight control by means of the synthetic jet actuators and it consists of a PID controller augmented by an adaptive neural network that increases its robustness and stability [17] [89].

The wind tunnel is also equipped with a Particle Image Velocimeter (PIV)

---

[3]Courtesy of Brzozowski(GA Tech)

system that includes a $100mJ$ dual Nd:YAG laser and two 1008×1016 pixel CCD cameras[89]. Seeding is done with micron-size smoke particles injected upstream of the model into the test section at a spanwise position aligned with the laser sheet[17]. The facility described in this section is designed to perform several free flight experiments such as:

- Static experiments: In this case, for a given angle of attack, the servo motor balances the aerodynamic moment to keep the airfoil at the desired angle of attack[17].

- Forced 1DOF maneuvers: Plunge (using the two linear slides) or pitch (using the servomotor or the synthetic jet actuators) following a prescribed trajectory[74].

- Forced 2DOF maneuvers: Plunge and pitch using the synthetic jet actuators following a prescribed trajectory[89].

- Disturbance rejection maneuvers. In this case a momentary external force is applied to the model in order to simulate a sudden gust and the rejection of this disturbance is accomplished by the synthetic jet actuators [17].

More details about the experimental set-up, the facilities and the different experiments performed on it can be found in references [74], [17] and [89]. More details about the controller and its configuration can be found in references [17] [89] [75] [74].

2.2 Modified NACA4415

The model mounted in the wind tunnel is a modified NACA4415 airfoil. In its actual configuration and design and with the purpose of making the model as light as possible, the airfoil consists of modular and interchangeable spanwise segments[17]. The model also has around 70 static pressure ports along the airfoil surface and located in the mid-span of the model[15]. Figure 2.4 shows the difference between a NACA4415 (left) and the modified (right) version used as baseline for this computational study. The primary difference is in the trailing edge of the airfoil where the tangential synthetic jet actuators, used to control the pitching moment of the airfoil, are mounted. In the detail at the bottom of figure 2.4, the dashed blue lines show the location of the pressure side (PS) and suction side (SS) of the unmodified airfoil. Also shown is the cavity of the actuator which will be explained in detail in the following section.

A NACA4415 has a maximum thickness to chord ratio of 0.15, but as shown in Figure 2.4, this thickness changes for the modified airfoil in the region close to the trailing edge at $\frac{x}{c} > 0.8$ where x is the distance along the chord and c is the chord length. The maximum thickness in this region due to the actuators is approximately $0.04c$. These actuators cover the airfoil surface from a position of $\frac{x}{c} \approx 0.8$ to $\frac{x}{c} \approx 0.98$, with the synthetic jet outlet located at $\frac{x}{c} \approx 0.96$. In the experimental set-up, the model has a chord length of $0.457m$ and a span of about $0.8m$. The Reynolds number based on the chord length and a free stream air velocity of $30m/s$ is $\approx 9 \times 10^5$. Finally, the shaft used to pitch the airfoil is located at $\frac{x_s}{c} = 0.272$ and $\frac{y_s}{c} = 0.036$ [89]

19
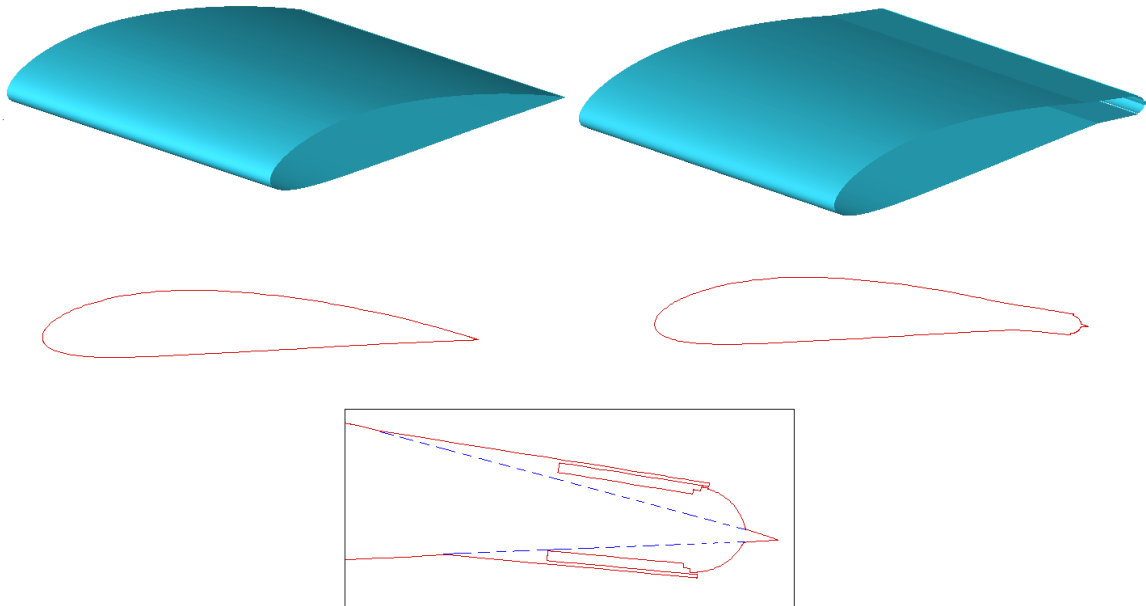
Figure 2.4: Comparison between a NACA4415 and the modified model used in the experimental set-up.

as shown in Figure 2.5[4].

2.3 Synthetic jet actuators

To control the motion of the model similar to the control a conventional wing, two tangential synthetic jet actuators are used closed to the trailing edge. These actuators have a characteristic height of $0.017c$ and they cover about $0.7m$ of the total airfoil span [89]. Each actuator consist of: a ramp, cavity, diaphragm, outlet

---

[4]Courtesy of Brzozoswki (GA Tech)

20
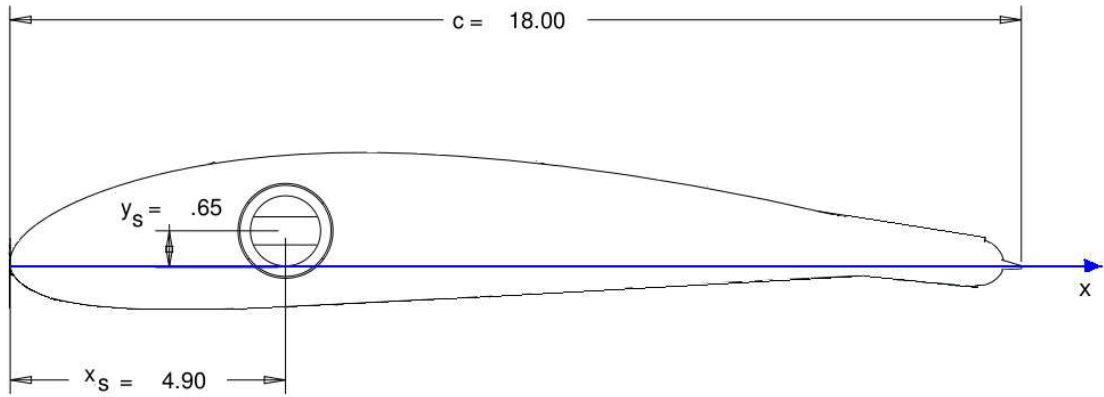
Figure 2.5: Modified NACA4415 section with shaft detail. Units in inches

and a Coanda surface as it is shown in figure 2.6[5]. The primary objective of the Coanda surface is to create a Coanda effect so that the synthetic jet attaches to its surface. The cavity has an aspect ratio $O(10^2)$ and the diaphragm is placed in its lower side (see Figure 2.6).

The diaphragm is a metallic disk attached to a piezoelectric element that is driven by an oscillatory voltage input from the controller. In practice, the actuators are excited at an off-resonance frequency between $1800Hz$ and $2400Hz$ [17]. The synthetic jet outlet is rectangular with its long side parallel to the trailing edge. The height of the outlet is $8.4 \times 10^{-4}c$ or $0.4mm$ [17]. The actuators are designed and built in a modular way so that each module has 4 piezoelectric disks with four modules mounted on each side of the airfoil [89]. Because of the discrete piezoelectric disks and the structure of the actuators, the strength of the synthetic jet varies along its

---

[5]Courtesy of Brzozoswki (GA Tech)

21
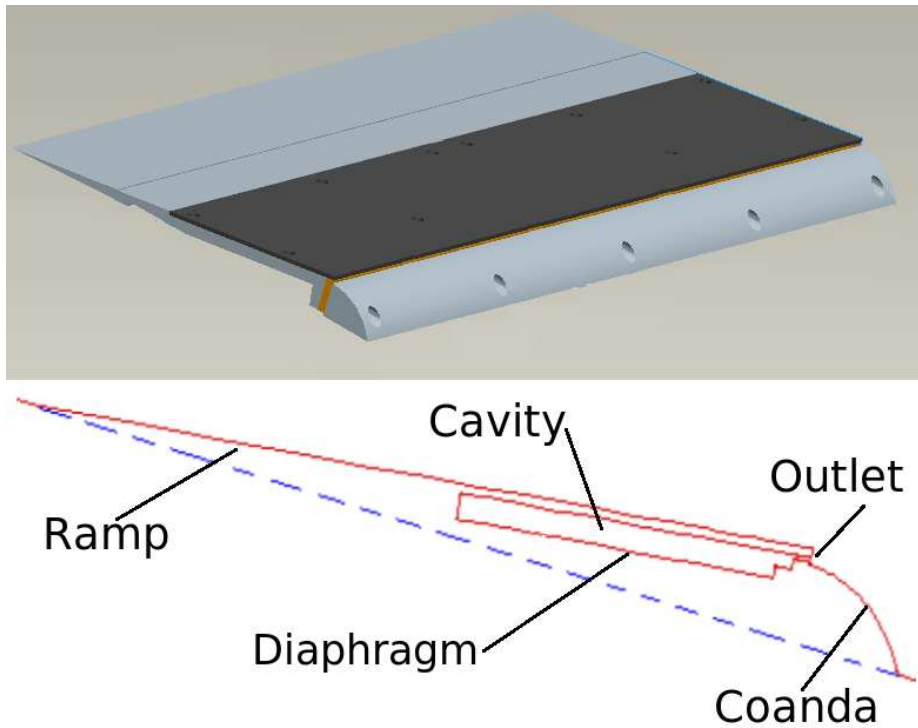
Figure 2.6: Detail of the actuator. 3D CAD view (Top). Sectional view with parts (Bottom)

length, introducing three dimensionality into the flow. The RMS velocity at the center of the synthetic jet outlet actuated in quiescent air is approximately $40\frac{m}{s}$. Hotwire measurements at the synthetic jet outlet show that the velocity has a small variation in the spanwise direction. Figure 2.7 shows the evolution of the velocity at two different spanwise locations: the center of the synthetic jet outlet and close to the boundary between two actuators mounted in the same module when the actuator is operated in quiescent air. It is clear that there is a difference of about 20 percent in the peak velocity.
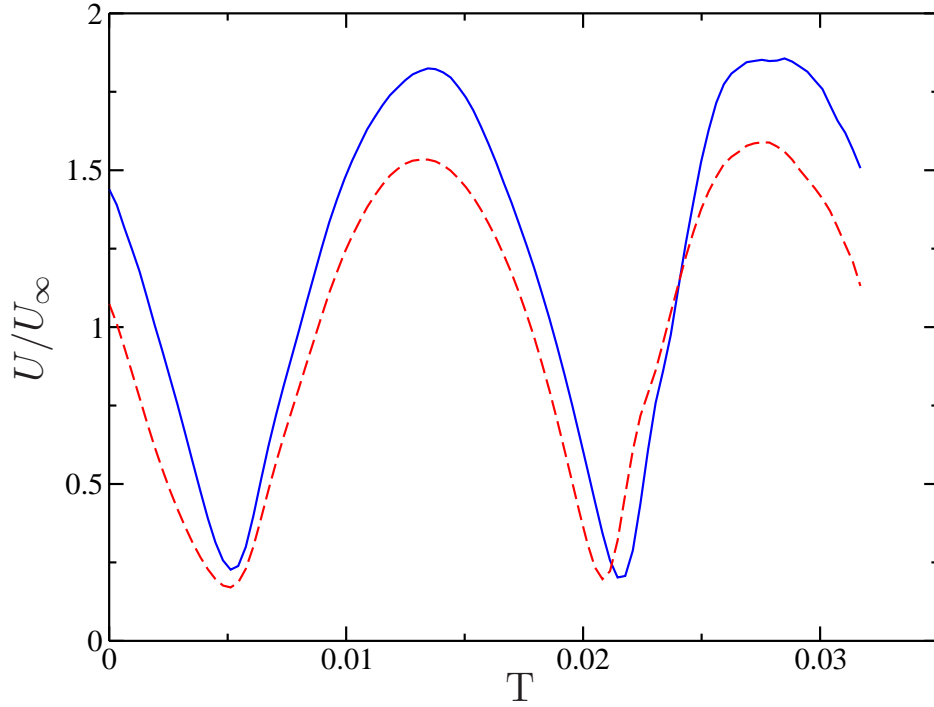
Figure 2.7: Hotwire measurement of the synthetic jet outlet velocity at two different spanwise positions. Center — Edge – –

An important non-dimensional parameter that characterizes the synthetic jet is the momentum coefficient (C_μ), given by

$$C_\mu \equiv \frac{U_{rms}^2 A_{jet}}{0.5 U_\infty^2 A_{pf}} \tag{2.1}$$

Where U_{rms} represents the RMS velocity at the synthetic jet outlet, A_{jet} is the area of the synthetic jet outlet and A_{pf} is the plan form area of the airfoil. In the experiments, the momentum coefficient is $O(10^{-3})$. The Reynolds number based on the slot height and the RMS velocity is $O(10^3)$. The tangential synthetic jet actuator configuration used here is intended to control the concentration of vorticity formed close to the

23

Figure 2.8: Dragon Eye wing section

trailing edge. By manipulating this trapped vorticity, the flow close to the trailing edge is modified so that the Kutta condition and the pressure distribution changes, leading to changes in the aerodynamic properties of the airfoil [38] [36] [37]. Though experimental tests of the synthetic jet actuators have so far been performed on the modified NACA4415 airfoil, the UAV on which the actuators are to be used is a Dragon Eye. An important characteristic of the Dragon Eye airfoil is its reflexed camber line (see Figure 2.8), which determines the longitudinal static stability of the wing[6] and the expected $\frac{\partial C_m}{\partial \alpha}$ to be negative. Planned experimental tests include the Dragon Eye with and without three actuators: two tangential actuators near the trailing edge used to control the airfoil pitching (similar to the NACA4415) and one normal actuator located in the suction side of the wing and near the suction peak intended to control boundary layer separation. The cavity of this normal-issuing actuator has the same geometrical configuration as the tangential ones [34]. The maximum thickness to chord ratio in the Dragon Eye airfoil is about 0.11 and a smaller thickness distribution in comparison to the NACA4415 airfoil.

---

[6]The actual Dragon eye UAV is tailless

Chapter 3

Approach, Techniques and Models

In this chapter, the computational approach, techniques and models used to perform numerical simulations of the airfoil and solved the proposed problem are described. The first part of this chapter includes the description of the governing equations, the turbulent model, the numerics of the flow solver and the way the turbulent model was implemented in the CFD code. This is followed by a discussion of the grid generation, as well as the boundary and initial conditions. Finally, two models for the synthetic jet simulation are presented and explained. By the end of this chapter, the reader should fully understand the problem and the way it was approached, so a section describing the importance and contribution of this work is included at the end of this chapter.

3.1 Governing Equations

The low speed flow in the Georgia Tech wind tunnel ($Ma = 9 \times 10^{-2}$) is represented by the constant density incompressible Navier-Stokes (NS) equations, describing conservation of mass and momentum. In the computational model developed here, the variables of the NS equations are considered to be filtered(LES) or averaged(RANS) so that an additional term appears in the equations; That is, the

subgrid-scale stress (LES) or Reynolds stresses (RANS) that arise from this filtering/averaging process. The filtering/averaging employed here will be indicated by a bar over a variable ($^-$). In RANS, the upper case variables represent the mean component while the lower case represent the fluctuating component for example the velocity is decomposed in to its mean $\overline{U_i}$ and its fluctuation u_i.

3.1.1 Conservation equations

The conservation of mass and momentum are expressed through the incompressible Navier-Stokes equation as:

$$\frac{\partial \overline{U_i}}{\partial x_i} = 0 \tag{3.1}$$

$$\frac{\partial \overline{U_i}}{\partial t} + \frac{\partial \overline{U_j U_i}}{\partial x_j} = -\frac{1}{\rho}\frac{\partial \overline{P}}{\partial x_i} + \nu \frac{\partial^2 \overline{U_i}}{\partial x_j^2} + \frac{\partial \tau_{ij}}{\partial x_j} \tag{3.2}$$

The last term in the momentum equation (3.2) is the divergence of the SubGrid-Scale (SGS) stress tensor (LES) or Reynolds stress tensor (RANS), which needs to be modeled. In general, this term can be written:

$$\tau_{ij} = -\overline{U_i U_j} + \bar{U}_i \bar{U}_j \tag{3.3}$$

but when $\overline{\overline{U}}_i = \bar{U}_i$ and $\bar{u}_i = 0$ as in the case for Reynolds average, this simplifies to

$$\tau_{ij} = -\overline{u_i u_j} \tag{3.4}$$

The stress is modeled via the Boussinesq approximation in which the deviatoric part of the stress is taken to be proportional to the strain rate tensor through the turbulent viscosity ν_t. In particular the stress is written

$$\tau_{ij} = \frac{2}{3}K\delta_{ij} - \nu_t \frac{1}{2}\left(\frac{\partial \overline{U_i}}{\partial x_j} + \frac{\partial \overline{U_j}}{\partial x_i}\right) \tag{3.5}$$

Where K is the turbulent kinetic energy (RANS) or subgrid energy (LES). The final form of the conservation of momentum equation is then obtained after simplification.

$$\frac{\partial \overline{U_i}}{\partial t} + \overline{U_j}\frac{\partial \overline{U_i}}{\partial x_j} = -\frac{1}{\rho}\frac{\partial}{\partial x_i}\left(\overline{P} + \frac{2}{3}K\right) + \frac{\partial}{\partial x_j}\left[(\nu + \nu_t)\frac{\partial \overline{U_i}}{\partial x_j}\right] \qquad (3.6)$$

Usually, a modified pressure $\tilde{P} = \overline{P} + \frac{2}{3}K$ is solved and unless one needs $\bar{P}$ away from boundaries ($\bar{P} = \tilde{P}$ at a wall), K never needs to be determined.

3.1.2 RANS and LES models

There are many different turbulent models that can be used to model the eddy viscosity and close the RANS/LES equations. In RANS, models are commonly classified by the dynamical equations that are solved for the turbulence quantities. These range from algebraic models such as the Balwin-Lomax model [6], one and two-equation models (e.g. k-ϵ model [55] [54]) and Reynolds stress transport models, which avoid the introduction of ν_t by solving for τ_{ij} directly. In LES, the most widely used model is the Smagorinsky model [109], which is algebraic. In this model, the eddy viscosity is proportional to a length scale squared (Δ^2) and the strain rate magnitude ($S = \sqrt{2\tilde{S}_{ij}\tilde{S}_{ij}}$)

$$\nu_t = (C_s\Delta)^2 S \qquad (3.7)$$

where C_s is the Smagorinsky constant which is commonly in the range of 0.1 and 0.2. Δ is called the filter width and it is related to a characteristic mesh or filter size.

RANS models have been widely used by the CFD community in theoretical and industrial applications showing satisfactory results in many applications, so that there

27

is a vast knowledge and experience in the implementation and use of these models. Nevertheless, in the past ten to fifteen years the development and improvement of RANS models has been static. Despite the fact that RANS models can be designed to predict boundary layers and boundary layers separation very accurately, their performance in very large separation regions (e.g: wakes) is not satisfactory [114]. For this reason and due to recent increases in computer power, the CFD community has moved towards the development of new LES models and the application of LES models in industrial problems with complex geometries[118]. However, a transition from a primary reliance on RANS models to a reliance on LES models has been slow for two reasons: First, a pure LES model is still computationally expensive, for example a complete LES simulation of an aircraft or a ground vehicle would require over $O(10^{11})$ grid nodes and approximately $O(10^7)$ time step which at the current rate of development in computational hardware, might be practical in 2045 [114]. Second, the majority of this expense is in the region close to the wall in which normally the near wall turbulence dynamics are resolved in what can be thought of a "Quasi-Direct Numerical Simulation" (QDNS)[112]. However, according to Spalart [112], even if the problem of LES wall treatment is solved allowing QDNS to be avoided, aerodynamic LES simulations will still be expensive.

3.1.3 Hybrid models

The disadvantages of RANS and LES models, as pointed out in the previous section, have been a motivation for the development of alternative turbulence methods. One of these alternatives, which is the approach followed here is to use a hybrid

(also called blended) RANS/LES model which allows the use of a RANS model close to the wall (in the boundary layer) and an LES model elsewhere in the computational domain. Using a RANS model close to the wall is advantageous since it reduces the resolution requirements in this region compared to LES. Another advantage of a hybrid method is that CFD codes (based on RANS and/or LES) can be extended to use hybrid models just by including an appropriate transition between the RANS and LES modes.

Hybrid models can be of two types: zonal and non-zonal. In both approaches, the user has to determine the regions of the computational domain in which each model is active. This is done through mesh generation and the model algorithm. The difference between the zonal and the non-zonal is in the transition between the RANS mode and the LES mode. In the non-zonal approach, this transition is achieved by a single formulation while in the zonal approach the transition is forced by two separated formulations at a explicitly defined interface between the RANS and LES regions[118]. In both models it is challenging to define the interface region, if this interface is too wide then there can be numerical errors in the model. On the other hand if the interface is too narrow then there can be discontinuities of the model variables that should be avoided[118]. Also, if the interface is defined in the log region of a turbulent boundary layer, then hybrid models have been found to incorrectly predict the velocity profile and hence the skin friction coefficient [128]. In practice the interface is set above the expected boundary layer thickness.

One of the first hybrid RANS/LES models was the Detached Eddy Simulation (DES) model [118]. Originally postulated in 1997 it has been widely used in different

CFD applications, most of them related with aerodynamics and aircraft [126] [107] [119] [43] [120], others have been related to ground vehicles [79] [80] and even active flow control applications [117]. DES was defined as "a three-dimensional unsteady numerical solution using a single turbulence model, which functions as a subgrid-scale model in regions where the grid density is fine enough for a large-eddy simulation, and as a Reynolds-averaged model in regions where it is not" [126] and in its original implementation is based on the Spalart-Allmaras (SA) RANS one-equation turbulence model, but it can be used in two-equations models as well [120] [29] [91]. The SA equation is a convection-diffusion equation with source terms to control the generation and destruction of the model variable $\tilde{\nu}$

$$\frac{\partial \tilde{\nu}}{\partial t} + \overline{U_i}\frac{\partial \tilde{\nu}}{\partial x_i} = c_{b1}\tilde{S}\tilde{\nu} + \frac{1}{\sigma}\left[\frac{\partial}{\partial x_i}\left((\nu + \tilde{\nu})\frac{\partial \tilde{\nu}}{\partial x_i}\right) + c_{b2}\left(\frac{\partial \tilde{\nu}}{\partial x_i}\right)^2\right] - c_{w1}f_w\left(\frac{\tilde{\nu}}{d}\right)^2 \quad (3.8)$$

The first term on the right hand side is a production term, the second is a diffusive term and the last a destruction term. $\tilde{\nu}$ and the eddy viscosity (ν_t) are related by $\nu_t = f_{v1}\tilde{\nu}$ where f_{v1} is given by

$$f_{v1} = \frac{\chi^3}{\chi^3 + c_{v1}^3} \quad (3.9)$$

Where χ is the ratio of the model variable ($\tilde{\nu}$) and the molecular viscosity i.e. $\chi \equiv \frac{\tilde{\nu}}{\nu}$.

$\tilde{S}$ in the production term of the SA equation is given by

$$\tilde{S} \equiv S + \frac{\tilde{\nu}}{\kappa^2 d^2}f_{v2} \quad (3.10)$$

where S is the magnitude of the vorticity or the strain rate, d represents the distance to the wall and $f_{v2} = 1 - \frac{\chi}{1 + \chi f_{v1}}$. For the destruction term of the SA equation f_w is

given by:

$$f_w = g \left[\frac{1 + c_{w3}^6}{g^6 + c_{w3}^6} \right]^{\frac{1}{6}} \qquad (3.11)$$

Where $g = r + c_{w2}(r^6 - r)$ and r is defined as $r \equiv \frac{\tilde{\nu}}{\tilde{S}\kappa^2 d^2}$. Finally to complete the SA model several constants that appear in equations 3.9 - 3.11 must be defined. These constants are: $\kappa = 0.41$ (Karman constant), $\sigma = 2/3$ (turbulent Prandtl number), $c_{b1} = 0.1355$, $c_{b2} = 0.622$, $c_{v1} = 7.1$, $c_{w1} = c_{b1}/\kappa^2 + (1 + c_{b2})/\sigma$, $c_{w2} = 0.3$ and $c_{w3} = 2$. All the constants are set as follows (see reference [115]): c_{b1} and c_{b2} were determined by testing the model in free shear flows, by matching the peak shear stresses of a two dimensional mixing layer and a two dimensional wake. c_{w3}, c_{w2} and c_{v1} are determined by testing the model in a boundary layer over a flat plate with zero pressure gradient. c_{w3} plays an important role in the shape of the velocity profile of the boundary layer especially in the outer part. c_{w2} is set by matching the skin friction coefficient for $Re_\theta = 1 \times 10^4$ and c_{v1} is set to match the inner intercept for the log law. Finally, c_{w1} is determined by postulating an equilibrium between the production, diffusion and the destruction terms.

To formulate the DES model based on the SA RANS model, An equilibrium between the production and the destruction terms of the SA equation is assumed so that the model variable $(\tilde{\nu})$ is proportional to $\tilde{S}$ (which is the vorticity magnitude or strain rate) and the distance to the wall square (d^2). By comparison with the Smagorinsky model (see equation 3.7) it is noticed that if d is replaced by a characteristic grid size like Δ then the SA model behaves like an LES model. Spalart suggested a new definition of d with $\tilde{d} = d \min(d, C_{DES}\Delta)$ so that the model behaves like RANS in the region where $d << \Delta$ and as an LES in the region of the domain

31

in which $\Delta << d$. C_{DES} is a constant that is equal to 0.65 for homogeneous turbulence [107]. In other words, with an appropriate grid design, DES modifies the length scale in the SA model to be proportional to the grid size far from the wall (LES mode), while remaining proportional to wall-distance near the wall (RANS mode). For a structured grid, Δ is commonly defined as the largest of the grid spacings in the three dimensions i.e: $\Delta = \max(\Delta_x, \Delta_y, \Delta z)$, but for an unstructured grid Δ is normally defined as the diameter of the grid cell (ϕ_{cv}) divided by $\sqrt{3}$ [126].

As DES was extensively used and applied in several engineering problems, different modeling deficiencies appeared e.g.: In thick boundary layers and shallow separation regions it was observed that DES exhibited premature transition from RANS to LES mode, leading to artificial separation, also known as Grid Induced Separation (GIS). For this reason, a new version of the DES model was proposed by Spalart et al [116]. This new version of DES was called Delayed Detached Eddy Simulation (DDES) and it consists on a redefinition of $\tilde{d}$ as:

$$\tilde{d} = d - f_d \max(0, d - C_{DES}\Delta) \tag{3.12}$$

Where $f_d = 1 - \tanh{(8r_d)^3}$ and it indicates the regions of the domain in which the DDES model behaves as SA-RANS ($f_d = 0$) or as DES ($f_d = 1$). r_d in equation 3.12 is given by:

$$r_d = \frac{\tilde{\nu}}{\sqrt{U_{i,j}U_{i,j}}\kappa^2 d^2} \tag{3.13}$$

This modification also makes the interface between RANS and LES (also called grey region) narrower, so that the transition between the RANS and LES modes happens more abruptly [116].

3.2 CFD code

One of the first steps in this study was the selection of a CFD tool for the implementation of DDES turbulent model and to achieve the proposed objectives, a CFD code with the following attributes was sought:

- Robust and reliable three dimensional flow solver.

- Ability to treat hybrid structured/unstructured meshes.

- LES or RANS model capabilities to enable the implementation of DDES.

- Parallel implementation with good scalability, at least up to hundreds of processes.

- Open source to allow the implementation of the turbulent model.

- Good discrete kinetic energy conservation properties, to support the LES region.

The final requirement is particularly important in the simulation of turbulent flows. Standard numerical methods commonly used in RANS models use highly dissipative numerical scheme or artificial dissipation. In the LES context these schemes are not appropriate since the numerical dissipation interferes with the effect of the subgrid model, disrupting the energy balance [88] [84] [77]. Reliable turbulence simulations for incompressible flows requires the use of numerical methods which retain the energy conservation characteristics of the convective and pressure terms of the NS equations. This means that the derivation of such a numerical scheme must ensure not only the conservation of momentum but also the conservation of kinetic energy. In structured

grids, this is accomplished by using a Harlow-Welch algorithm [56] in which there is no need for artificial viscosity to ensure stability. For unstructured grids, the development of such schemes is more complicated. Nevertheless, Mahesh et al [77] have achieved satisfactory results in the development of non-dissipative LES schemes on unstructured grids. This model was implemented in an unstructured grid incompressible flow solver called CDP v2.3[1] [2] which was developed at the Center for Integrated Turbulence Simulations (CITS) at Stanford University and it has been widely used in a variety of fluid flow problems becoming one of the state of the art unstructured LES codes [85]. CDP v2.3 fulfills the requirements and criteria needed in this study such as:

- It is a nearly energy conserving solver.

- It can be run as an standard LES code with several different model such as Smagorinsky and dynamic Smagorinsky.

- It can also be used as a Direct Numerical Simulation (DNS) solver.

- It is parallel with good scalability up to thousands of CPUs [53].

- It can handle hybrid meshes that can be partitioned with the standard ParMETIS library [70].

---

[1]`http://www.stanford.edu/group/cits/research/combustor/cdp.html`
[2]CDP was name after Charles David Pierce, a researcher who worked at Stanford and made several important contributions to the LES modeling of turbulent reacting flows

3.2.1 Temporal and Spatial discretization of the N-S equations in CDP v2.3

For completeness and to set the context for the implementation of the DDES model, the algorithm implemented in CDP v2.3 is briefly described here. More details about the numerical method used in CDPv2.3 are given in references [77] and [62] and details about the numerical conservation of kinetic energy can be found on reference [52]. Some aspects about the boundary conditions, discretization of the NS equation at the boundary and parallel performance of CDP can be found on references [134] and [53]. CDP documentation [51] has information about the requirements, installation, grid partition, numbering and ordering of nodes, faces and cells, connectivity and variables handling. CDP v2.3 uses a collocated finite volume formulation of the NS equation. In this formulation, field variables such as velocity, pressure and scalars are cell centered while the velocity normal to each face is maintained as face centered as is shown in figure 3.1. In this example $\overline{U}$ and $\overline{P}$ represent the velocity and pressure associated with the grey element (internal element) and the face velocities $\overline{U_{f1}}$, $\overline{U_{f2}}$ and $\overline{U_{f3}}$ are shared variables associated not only with the grey element but also with its neighbor elements.

For the temporal discretization, CDP v2.3 uses the fractional-step method, originally proposed by Chorin in 1968 [26]. Moin et al [86] proposed an improvement of the fractional-step method that consisted on the appropriate formulation of boundary conditions for the intermediate velocity field. Then in 2004, Mahesh et al [77] and Ham et al [52], extended this method to have better properties for the numerical conservation of kinetic energy on hybrid meshes.
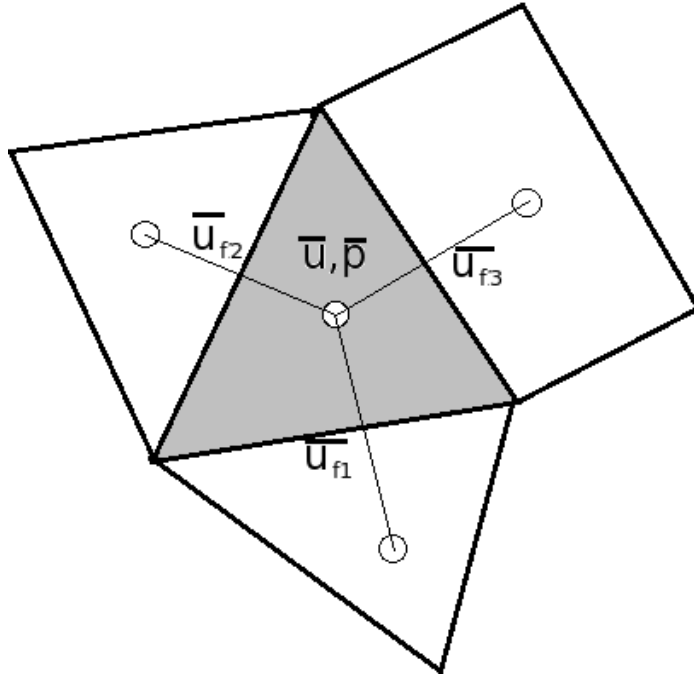
Figure 3.1: Variables association on CDP v2.3

When the fractional step method is applied to the momentum equation (see equation 3.6), it is split in two steps:

$$\frac{\hat{\overline{U}}_{i,cv} - \overline{U}^n_{i,cv}}{\Delta t} V_{cv} + \frac{1}{2}(\hat{H}_{i,cv} + H^n_{i,cv}) = -\frac{\partial \overline{P}}{\partial x_i}^{n-1/2} V_{cv} \tag{3.14}$$

$$\frac{\overline{U}^{n+1}_{i,cv} - \hat{\overline{U}}_{i,cv}}{\Delta t} = -\frac{\partial \overline{P}}{\partial x_i}^{n+1/2} \tag{3.15}$$

Where $\hat{\overline{U}}$ represents an intermediate velocity field that does not satisfy the continuity equation (see equation 3.1) while $\overline{U}^n_{i,cv}$ and $\overline{U}^{n+1}_{i,cv}$ must satisfy it. The subscript cv stands for the control volume in which the equation is discretized, e.g. V_{cv} represents its volume. The pressure gradient ($\frac{\partial \overline{P}}{\partial x_i}$) is evaluated using the Green-Gauss theorem

[8] assuming that the gradient of the variable is constant over the control volume (see Appendix A)

In equation 3.14, $H_{i,cv}$ represents the convective and diffusive terms (i.e. $H_{i,cv} = \text{conv}_{i,cv} - \text{diff}_{i,cv}$) and their discretization plays an important role in the numerical conservation of kinetic energy. In a finite volume discretization the convective term can be expressed using the convective fluxes through the control volume faces and it is given by:

$$\widehat{\text{conv}}_{i,cv} = \sum_{f=1}^{nf} \overline{U}_f^{n+1} \left(\frac{\hat{\overline{U}}_{i,cv} + \hat{\overline{U}}_{i,cv_{nbr}}}{2} \right) A_f \tag{3.16}$$

In this equation the subscript cv_{nbr} stands for the neighbor control volume value associated to the face f. A_f represents the area of the face f. In order to avoid solving non-linear algebraic equation while also avoiding Courant-Friedrich-Lewis (CFL) stability constraints from the convective term, the face velocity $\overline{U}_f^{n+1}$ is predicted before the first step of the fractional step method.

Similarly, in a finite volume discretization the diffusive term can be written using the diffusive fluxes through the control volume faces. In CDP v2.3 the discretization of the diffusive terms is done following Zwart's description [134] given by:

$$\widehat{\text{diff}}_{i,cv} = \sum_{f=1}^{nf} (\nu_f + \nu_{tf}) \left(\psi \frac{\hat{\overline{U}}_{i,cv} - \hat{\overline{U}}_{i,cv_{nbr}}}{\Delta s} + \left(\overline{\nabla \overline{U}}^n (\hat{n} - \psi \hat{s}) \right)_i \right) A_f \tag{3.17}$$

Where ν_f and ν_{tf} represent the molecular and eddy viscosity at the face respectively, which are computed by a simple average of the cell centered values. $\hat{n}$ is the unit normal vector to the face f and $\hat{s}$ is a unity vector defined in the direction from

the centroid of the control volume to its neighbor. Δs is the distance between the centroid of the control volume and its neighbor. ψ is a scaling factor that depends on geometrical parameters and for unstructured grids is defined as $\psi = \hat{s} \cdot \hat{n}$. The term $\overline{\nabla \overline{U}}^n$ is the average velocity gradient between the control volume and its neighbor.

The algorithm advances in time as follows:

1. Prior to the first step of the fractional step method, the face velocity $\overline{U}_f^{n+1}$ is determined using an Adams-Bashforth predictor

$$\overline{U}_f^{n+1} = \frac{3}{2}\overline{U}_f^n - \frac{1}{2}\overline{U}_f^{n-1} \tag{3.18}$$

   CDP v2.3 solves and couples any passive or reactive scalar with the NS solver at this point (between step 1 and 2).

2. $\hat{\overline{U}}_i$ is calculated by solving the momentum equation 3.14 including the discrete convective and diffusive terms (equations 3.16 and 3.17). Since the discretization of the velocity in this step is semi-implicit a linear system of equations must be solved using a BiConjugate Gradient Stabilized (Bi-CGSTAB) solver [33].

3. A Poisson equation for $\overline{P}^{n+1/2}$ is obtained by taking the divergence of the second step of the fractional step method (equation 3.14) and using the continuity equation (equation 3.1).

$$\sum_{f=1}^{nf} \left.\frac{\partial \overline{P}}{\partial n}\right|_f^{n+1/2} A_f = \frac{1}{\Delta t}\sum_{f=1}^{nf} \hat{\overline{U}}_f A_f \tag{3.19}$$

Where $\left.\frac{\partial \overline{P}}{\partial n}\right|_f^{n+1/2}$ represents the face normal component of the pressure gradient and the normal face velocity $(\hat{\overline{U}}_f)$ is computed by a simple interpolation of the

38

predicted cell centered velocity of the previous step. The system of equations for the pressure (equation 3.19) is solved using an Algebraic MultiGrid (AMG) Solver using the Hypre library[3].

4. Finally, the velocity is corrected based on the pressure field solved in the previous step i.e:

$$\overline{U}_{i,cv}^{n+1} = \hat{\overline{U}}_{i,cv} - \Delta t \frac{\partial \overline{P}}{\partial x_i}^{n+1/2} \tag{3.20}$$

3.2.2 DDES implementation on CDP v2.3

To use CDPv2.3 for the AVOCET project the DDES model had to be implemented. One important characteristic of the discretization of the SA equation is its positivity i.e. the numerical scheme must ensure that $\tilde{\nu}$ is positive everywhere and at every time step [115] [76]. The continuous SA equation satisfies the positivity of $\tilde{\nu}$, but in its discrete form this characteristic must be enforced. A non-positive $\tilde{\nu}$ not only represents a non-physical situation but also represents stability problems in the numerical scheme specially for the NS solver.

3.2.2.1 Discretization of the Spalart-Allmaras equation in CDP v2.3

The solution of the SA equation is included into the NS algorithm described in section 3.2.1 between steps 1 and 2, because this is where CDP solves other scalar equations (passive and reactive). To be consistent with the NS solver, the discretization of the SA equation was done based on Zwart's methodology [134] so that the

---

[3]`https://computation.llnl.gov/casc/linear_solvers/sls_hypre.html`

same operators used in the NS solver are used in the discretization of the SA equation. As long as $\tilde{S}$ is positive the destruction and production terms are always positive so they can be treated as sources. This ensures that the matrix of the system of equations resulting from the solution of the SA equation is diagonally dominant. For the time advancement, a backward Euler scheme was used to preserve the positivity of $\tilde{\nu}$, similar time marching scheme for the SA equation has been used in other studies [123] [115]. Forward Euler and Crank-Nicholson schemes were tested as well but they lead to negative eddy viscosities resulting in a NS solution blow-up. The discrete SA equation is given by

$$\frac{\tilde{\nu}^{n+1} - \tilde{\nu}^n}{\Delta t} + \text{conv}^{n+1} - \text{diff}^{n+1} = C_{b1} \tilde{S}^n \tilde{\nu}^n + \frac{C_{b2}}{\sigma} \left(\frac{\partial \tilde{\nu}^n}{\partial x_i} \right)^2 - C_{w1} f_w^n \left(\frac{\tilde{\nu}^n}{\tilde{d}} \right)^2 \quad (3.21)$$

The discretization of the convective term (conv^{n+1}) is done with an upwinding scheme given by:

$$\text{conv}^{n+1} = \sum_{f=1}^{n_f} \overline{U}_f^{n+1} \left[\left(\frac{\gamma \tilde{\nu}_{i,cv}^{n+1} + \beta \tilde{\nu}_{i,cv_{nbr}}^{n+1}}{2} \right) + \Phi \overline{\nabla \tilde{\nu}_{cv}}^n \cdot \hat{s} \right] A_f \quad (3.22)$$

Where the values of the coefficients γ, β and Φ depend on the type of scheme used. By default, CDP uses a 2ND order QUICK scheme in which $\gamma = 3/2$, $\beta = 1/2$ and $\Phi = 1$. The diffusive term (diff^{n+1}) is treated as in the NS equation and is given by

$$\text{diff}^{n+1} = \frac{1}{\sigma} \sum_{f=1}^{n_f} (\nu + \tilde{\nu}^n)_f \left[\psi \left(\frac{\tilde{\nu}_{i,cv}^{n+1} - \tilde{\nu}_{i,cv_{nbr}}^{n+1}}{\Delta s} \right) + \overline{\nabla \tilde{\nu}_{cv}}^n \cdot (\hat{n} - \psi \hat{s}) \right] A_f \quad (3.23)$$

Where $(\nu + \tilde{\nu}^n)_f$ is the sum of the molecular viscosity and the model variable at the face. The value of $\tilde{\nu}$ used in this case is at the old time level n to avoid non-linearity of the diffusive term. $\overline{\nabla \tilde{\nu}_{cv}}^n$ corresponds to the average gradient of $\tilde{\nu}$ between the

40

control volume and its neighbor. The non symmetric sparse matrix that is obtained from the discretization of the SA equation is also solved using a Bi-CGSTAB solver.

3.2.2.2   DDES model tuning

Several adjustments to the standard DDES model were implemented to preserve positivity and to obtain values of the eddy viscosity in the wake that are consistent with expectations. First, it is required that $\tilde{S}$ must be greater than zero every time step and everywhere in the computational domain. Deck et al [119] proposed a new definition of $\tilde{S}$ to ensure the positivity of $\tilde{\nu}$. This modification does not affect the performance of the turbulent model and prevents the spurious propagation of eddy viscosity in the simulation of flows with laminar separation regions [32]. This new definition of $\tilde{S}$ is given by

$$\tilde{S} \equiv f_{v3}S + \frac{\tilde{\nu}}{\kappa^2 d^2}f_{v2} \tag{3.24}$$

Where $f_{v2} = \left(1 + \frac{\chi}{5}\right)^{-3}$ and $f_{v3} = \frac{(1+\chi f_{v1})(1-f_{v2})}{\chi}$.

The DDES implementation first test was on a flat-plate boundary layer in which the model should behave like RANS since no separation is expected. In the wall normal direction the first grid point is located at $y^+ = 6$ and a growing ratio of 1.2 was used from this point on, results were analyzed at $x = 1$ in which $Re_\theta = 6.6 \times 10^5$. Figure 3.2 shows U^+, eddy viscosity and U/U_∞ profiles, in which the different regions of the boundary layer are clear and a good agreement with the log-law is also appreciated. The shape of U/U_∞ is satisfactory and in agreement with other computational results [115].

Though boundary layer tests were satisfactory, results from early tests on

41
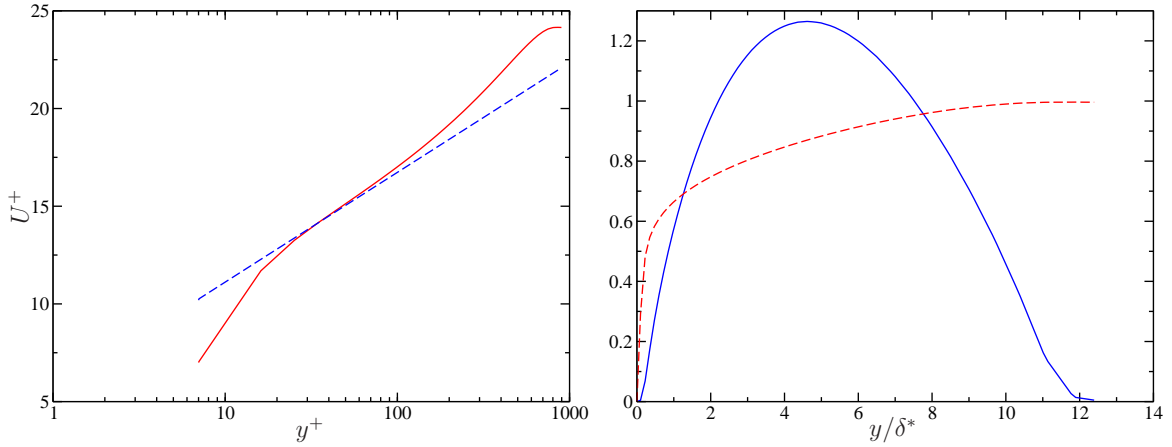
Figure 3.2: Boundary layer test results: Velocity profile in wall units (left) $-$ DDES model $--$ log-law and U/U_∞ $(--)$ and $\nu_t/(0.025 U_\infty \delta^*)$ $(-)$ profiles (right).

separated flow showed unexpected high values of the eddy viscosity in the wake and in the separation region. Basically, the model was behaving as RANS in these regions. This observation had been reported previously in the DDES model by Deck [31] who attributed it to a slow transition from RANS to LES mode due to an extended grey-area, leading to a delay in the development of instabilities and turbulent fluctuations. As pointed out by Breuer et al [14] in the LES region there should be an equilibrium between the production and destruction of $\tilde{\nu}$, leading to values of the functions $f_{v1} = 1$, $f_{v2} = 0$ and $f_w = 1$. It was also suggested that Δ be redefined as $\Delta = \sqrt[3]{V_{cv}}$ in the LES region, so that it matches the usual LES definition. To determine where the switch from RANS to LES mode should occur, the Extended Delayed Detached Eddy simulation (EDDES) proposed by Riou et al[99][98], was used. This extension takes advantage of the DDES function f_d to define the interface between the LES and RANS regions as follows:

42
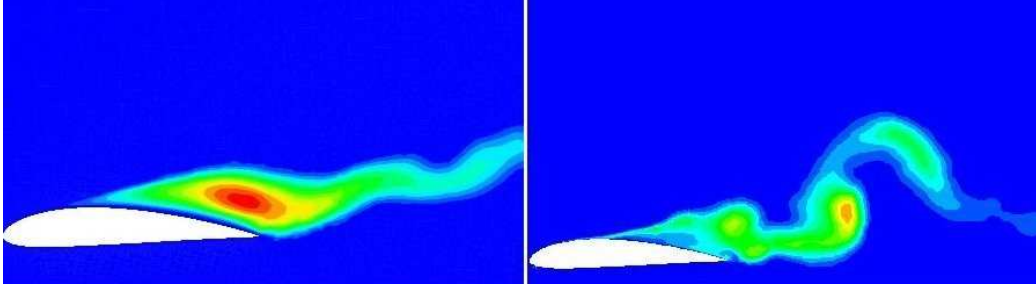
Figure 3.3: Eddy viscosity field $\alpha = 30°$ and $Re = 5.7 \times 10^5$. From DDES (left) and EDDES (right) models

$$\Delta\ ,f_{v1}\ ,f_{v2}\ \text{and} f_w = \begin{cases} \frac{\phi_{cv}}{\sqrt{3}}\ ,\frac{\chi^3}{\chi^3+c_{v1}^3}\ ,\left(1+\frac{\chi}{5}\right)^{-3}\ \text{and}\ g\left[\frac{1+c_{w3}^6}{g^6+c_{w3}^6}\right]^{\frac{1}{6}} & f_d < f_{d0} \\ \sqrt[3]{V_{cv}}\ ,f_{v1}=1\ ,f_{v2}=0\ \text{and}\ f_w=1 & f_d \geq f_{d0} \end{cases} \quad (3.25)$$

Where f_{d0} is a threshold value for the function f_d, normally taken to be equal to 0.8. ϕ_{cv} is the diameter of the control volume and V_{cv} is the volume of the cell. Figure 3.3 shows the eddy viscosity field from the DDES model and the extended DDES (EDDES) model in a simulation of flow around a NACA4415 airfoil. A reduction of the magnitude of the eddy viscosity, of about 1 order of magnitude, is observed in the wake accompanied by an stronger vorticity breakdown.

Finally, a limiting algorithm that consists of modifying the coefficients (γ, β and Φ) used in the discretization of the convective term of the SA equation was implemented. This algorithm is used in CDPv2.3 to limit the mixture fraction variable in chemical reacting flows [51] and consists of the following steps:

1. The SA equation is solved with the Bi-CGSTAB solver.

2. From this initial solution, those cells in which $\tilde{\nu} < 0$ are identified.

3. The coefficients of the convective discretization are modified so that a fully upwind formulation (technically known as Upwind Differencing Scheme [96]) is used on those problematic cells. The new value of the coefficients in this case are : $\gamma = 2$, $\beta = 0$ and $\Phi = 0$

4. The SA solver is rerun.

This approach locally increases the numerical diffusion to ensure that the lower bound of the model variable is limited to 0^+

3.3 Grid Generation

Any hybrid RANS/LES model requires an appropriate mesh which plays an important role in the performance of the model. The criteria to design a mesh in DES is based on physical and numerical arguments rather than on convergence issues (like in RANS and DNS) [113]. Any mesh intended for a DES model must have 3 basic regions: Euler, RANS and LES. The Euler region is the zone in the computational domain in which irrotational flow is expected. For an external flow simulation, the Euler region covers the majority of the domain, especially upstream of the airfoil. The RANS region is the part of the domain that is close to the wall (i.e. the boundary layer) and the guidelines to design it for a DES simulation are exactly the same used in a pure RANS simulation. The RANS region is further subdivided in to: the viscous RANS region and the RANS outer region. The viscous RANS region is closest to the wall and it has several requirements such as: the first cell should be about 2 in

wall units i.e: $\Delta y^+ \approx 2$, the stretching ratio should be about 1.25 or less for good resolution in the log layer and this region should be extended up to about half of the expected boundary layer thickness (δ). The RANS outer region goes from about $\delta/2$ up to 2-3 times δ. The grid spacing normal to the wall in the outer RANS region should not exceed $\delta/10$ [113].

The LES region is the part of the computational domain (excluding the boundary layer) in which it is expected to have vorticity and turbulence. This region is subdivided in to: viscous LES region, departure region and focus region. The viscous LES region is the zone in which detached boundary layers are expected and it has the same requirements as the viscous RANS region. The focus region is the region close and downstream of the airfoil where the vorticity in the wake has to be resolved. This region is characterized by having an isotropic mesh with a grid size called Δ_o which is a measure of the LES filter in the DES model. In practice, in the simulation of flow around airfoils the focus region goes up to 3-5 chords downstream [113]. Finally, the departure region is further downstream than the focus region. In this region it is not necessary to resolve vortical structures of size Δ_o, so that the size of the cells can be greater than Δ_o. The departure region provides a smooth transition and connection between the focus and the Euler regions.

The first step in the mesh design is to determine the shape and size of the domain. In the simulation of external flows especially in flow around airfoils, three types of meshes are commonly used: C-mesh, O-mesh and H-mesh [22]. The addition of the actuators increases the complexity of the geometry with respect to an unmodified airfoil. An O-mesh is probably one of the easiest meshes to generate but it has two

45

disadvantages: first it will extend to regions far from the airfoil where the numerical solution is of no interest for this study and second refinement of the region downstream of the airfoil is needed in order to satisfy the requirements of the turbulent model, so a C or H mesh are more suitable for the turbulent model. For this research a C topology is appropriated since it can support appropriate mesh refinements in the wake region. Grids can also be classified in three types based on the connectivity of the mesh and the form of the data structure: Structured, unstructured and hybrid [124]. A hybrid C-mesh was selected as appropriated for this study since its shape brings some advantages from the turbulent model perspective i.e: It allows a structured grid close to the airfoil (RANS region) and an unstructured grid in the rest of the domain (LES and Euler regions).

Even though there are not any guidelines to determine the size of the domain, in the simulation of airfoils in free flight it is clear that the bigger the domain the better, so that the outer boundary of the domain does not interfere with the solution close to the airfoil. But, as the size of the domain increases, the number of cells increases as well, leading to a more expensive simulation. The size of the domain in the spanwise direction (z direction) plays an important role in the performance of the turbulent model and in the numerical results especially at high angle of attack. A computational domain with a spanwise length of less than 1 chord ($1c$) leads to an over prediction of the aerodynamic properties of the airfoil and a domain with a spanwise length greater than 1.5 chord ($1.5c$) is more reliable [18]. Shur et al [107] suggest that at moderate Reynolds number and angle of attack, the difference in the computational results and the aerodynamic properties of the airfoil between a $1c$

46
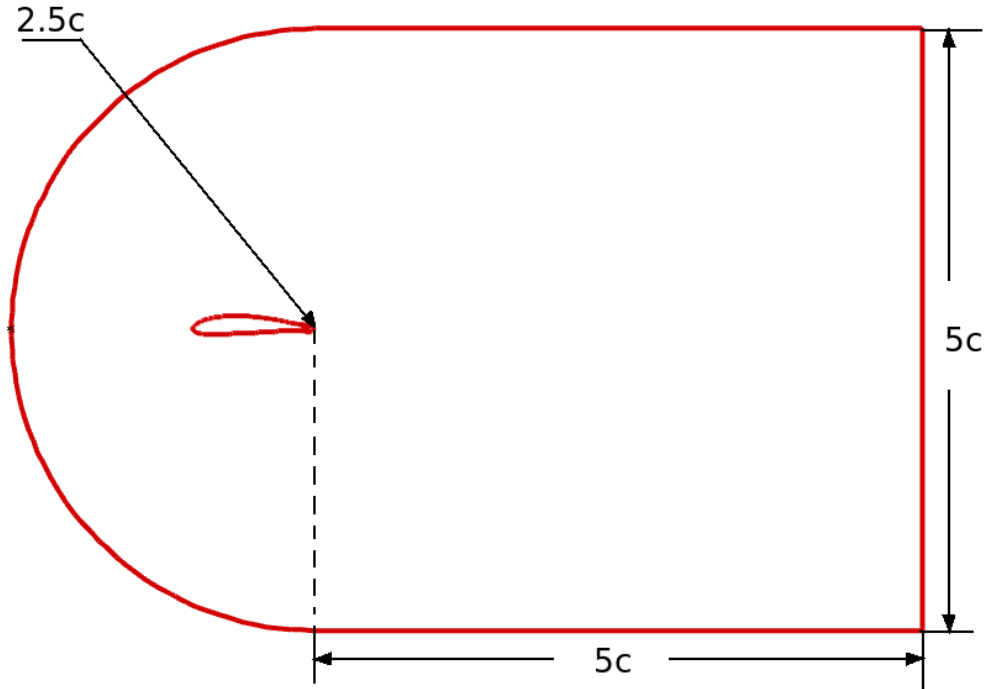
Figure 3.4: XY view of the computational domain

length domain and a $2c$ length domain in the spanwise direction is very small. Based on these observations, the domain used in this study is selected to be one chord length in the spanwise direction. A two dimensional view (XY) of the final shape and size ($7.5c \times 5c \times 1c$) of the mesh used here is shown in figure 3.4.

In order to satisfy the requirements of the DES model, the grid design continues with the meshing of the RANS region (structured mesh). Starting with the viscous region and based on the chord Reynolds number of 1×10^6 a grid spacing of $O(10^{-5}c)$ was chosen in the direction normal to the wall. The size of the first grid cell in wall units is about 1.5 i.e: $\Delta y_1^+ = 1.5$. Along the surface of the airfoil 150 grid points

47

were used. These grid points were clustered towards the leading and the trailing edges giving a grid spacing of $O(10^{-2}c)$ to $O(10^{-3}c)$. The stretching ratio used in the viscous region was 1.2 and the region was extended to about $\delta/2$. δ was estimated with a combination of a vortex panel method and two numerical boundary layer methods for a flow over NACA4415. This a standard and widely use method for the estimation of airfoil aerodynamic properties [103] [87] [121]. The vortex panel method allows computation of the inviscid flow around the airfoil, and to obtain the pressure and an approximate outer velocity distribution along the upper and lower surfaces of the airfoil. Based on the pressure and velocity distribution, a laminar integral boundary layer method can be used to compute the laminar part of the boundary layer and if transition occurs then the transition point along the airfoil is determined. Finally, a turbulent boundary layer method is used from this point until the trailing edge. For a low positive angle of attack and $Re = 1 \times 10^6$, the boundary layer on the suction side experiences transition from laminar to turbulent while the pressure side remains laminar. Table 3.1 shows the methods, codes and conditions used in the estimation of δ. For these conditions the suction side boundary layer showed the following result at the transition point $(x/c = 0.2361)$ $\delta^\star = 0.844 \times 10^{-3}$, $Re_\theta = 460.2$ and a maximum boundary layer thickness of $0.035c$ close to the trailing edge.

The outer RANS region goes from $\delta/2$ up to 3δ. In the first part of this region (up to δ) the mesh size was fixed to $\delta/10$, from δ to 3δ a stretching ratio of 1.25 was used. Details about the mesh in the cavity of the actuator are presented in section 3.5.1 but the requirements of the RANS region were followed in this part of the domain as well.

48

	Method	Code [a]	Conditions
Inviscid flow	Hess-Smith	HSPM	NACA4415 airfoil $\alpha = 5°$
Laminar BL	Thwaites [127]	thwaites	2D flow with $Re = 1 \times 10^6$
Transition	Michel [81]	michel	$Re_\theta < 1.174 \left(1 + \frac{22400}{Re_x}\right) Re_x^{0.46}$
Turbulent BL	Head [19]	head	SS:$H1_{trans} = 1.4$ $\theta/L_{trans} = 0.317 \times 10^{-3}$

[a] Developed by Cebeci et al [20]

Table 3.1: Estimation of δ for the suction side

The LES region has two types of meshes: structured (viscous region) and unstructured (focus and departure regions). For the viscous region and as suggested by Spalart [113], similar parameters to those used in the RANS viscous region were used. The near-wall grid size in wall units is of order 1.5 but the stretching ratio was reduced to 1.1 in order to resolve small vortices in the detached boundary layer. This viscous LES region extends from the wall up to $0.2c$ downstream. The focus region is probably one of the most important parts of the domain because it is the region in which the dynamics of the wake are resolved. Since the final purpose of the CFD part of the AVOCET project is to simulate the dynamics of free flight maneuvers, the angle of attack during these maneuvers will be changing in time (positive and negative). This means that the focus region is not only limited downstream of the airfoil but also above and below of it. This is the reason why a parabolic geometry was chosen for this region (see figure 3.5). One relevant characteristic of the grid in the focus region is its isotropy, the characteristic grid size (Δ_o) of this region is determined by the grid resolution in the spanwise direction. Fifty grid points were used in the spanwise direction making Δ_o equal to $0.02c$. The focus region mesh was generated so that most of its elements were isotropic with an edge size of $0.02c$.
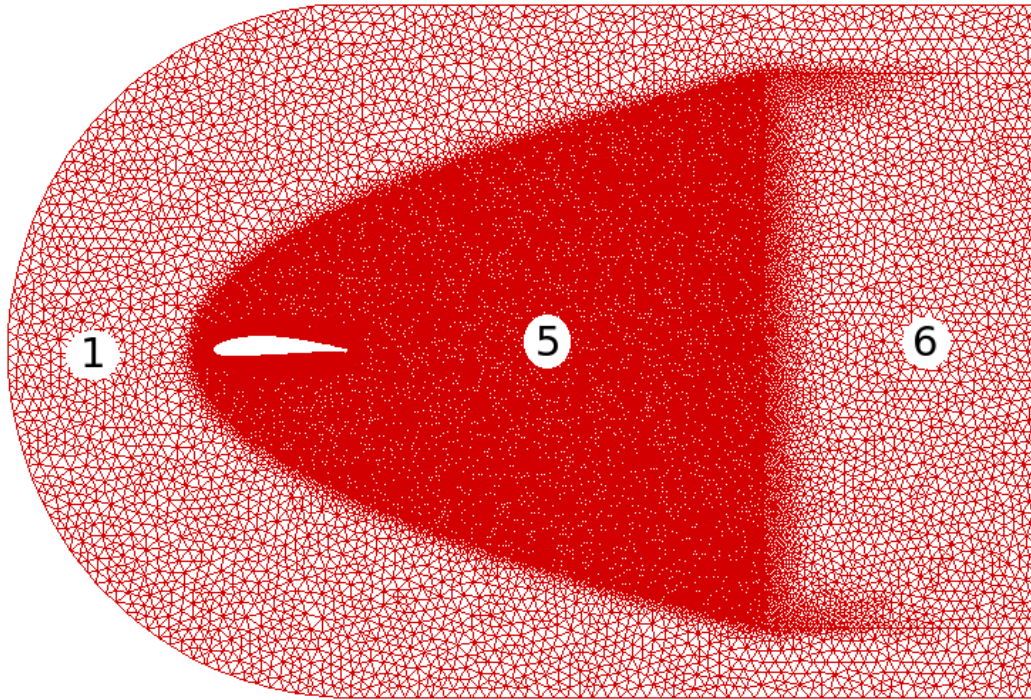
Figure 3.5: Mesh

The departure region goes from $4c$ up to $6c$ downstream, in this region the size of the elements varies between $0.02c$ and $0.1c$. The transition between the focus and the Euler region is done smoothly as shown in figure 3.5. Finally, the Euler region covers the rest of the domain and it has a characteristic mesh size of $0.1c$. Figure 3.5 shows the final mesh used in this research. Figure 3.6 shows the detail of the mesh in the RANS region including the transition from structured to unstructured. Table 3.2 shows id number for figures 3.5 and 3.6 along with the extension of the regions within the computational domain. Table 3.3 summarized the different regions in which the computational domain was subdivided and the characteristic grid sizes used in each one.
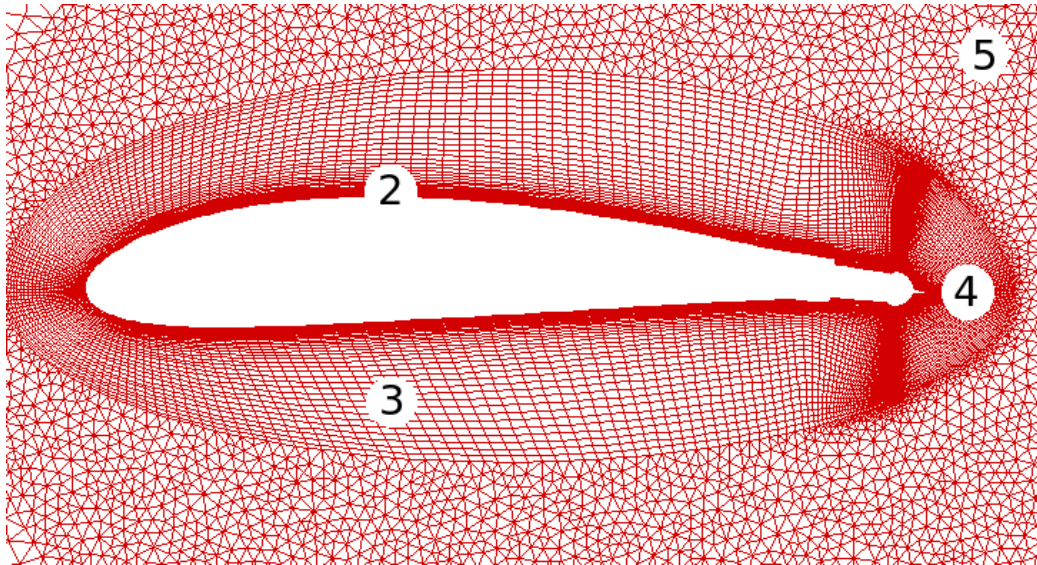
Figure 3.6: Mesh details close to the airfoil

Gridgen [4], a commercial software package for grid generation, was used to generate the grids. The mesh was created by blocks, taking advantage of the automatic mesh generators and smoothness algorithms available in Gridgen. The blocks in the RANS and the viscous LES regions were created first. Based on these blocks, the focus region was generated and finally the Euler and departure regions were created. To create the three dimensional domain, all the blocks were extruded in the z direction. A gridgen script file [5] can be used to recreate this process and the mesh used in this numerical study (see Appendix B). In order to execute this script a grid file [6], that describes the modified NACA4415 geometry, is required. Figure 3.7 shows the wing section described in the gridgen grid file and Table 3.4 summarizes details about

---

[4]`http://www.pointwise.com/gridgen/`
[5]`http://turbulence.ices.utexas.edu/data/gridgen_avocet/modifiedNACA4415.glf`
[6]`http://turbulence.ices.utexas.edu/data/gridgen_avocet/modifiedNACA4415.grd`

Region	ID $N°$ figs 3.5, 3.6	Location
Euler	1	Upstream airfoil
VR RANS	2	Wall up to $\sim \delta/2$
OR RANS	3	$\sim \delta/2$ up to $\sim 3\delta$
VR LES	4	Wall up to 0.2c downstream
FR LES	5	$\sim 3\delta$ up to 4c downstream
DR LES	6	4c up to 6c downstream

Table 3.2: Mesh regions extension

Region	Type	Size
Euler	Unstructured	$\Delta \approx 0.1c$
VR RANS	Structured	$\Delta y_1^+ = 1.5$, $\frac{\Delta y_j}{\Delta y_{j+1}} = 1.2$, $\Delta x O(10^{-2}c)$
OR RANS	Structured	$\Delta y < \frac{\delta}{10}$
VR LES	Structured	$\Delta y_1^+ = 1.5$, $\frac{\Delta y_j}{\Delta y_{j+1}} = 1.1$, $\Delta x O(10^{-3}c)$
FR LES	Unstructured	$\Delta = \Delta_o = 0.02c$
DR LES	Unstructured	$\Delta_o < \Delta < 0.1c$

Table 3.3: Mesh region types and sizes

the mesh .

3.4   Initial and boundary conditions

The initial condition for the velocity is just the free-stream velocity everywhere in the computational domain, corresponds with an impulsive start of the body. This is a common initial condition used in theoretical and computational fluid dynamics. Appropriate initial conditions for the eddy viscosity depends on the free-stream turbulence levels at the inlet of the domain (e.g. the wind tunnel). If the level of the free-stream turbulence are not available, Spalart [115] suggests that the initial condition should be set equal to the free-stream value $\tilde{\nu}$ and $\tilde{\nu} < \nu/10$ is acceptable. Here,
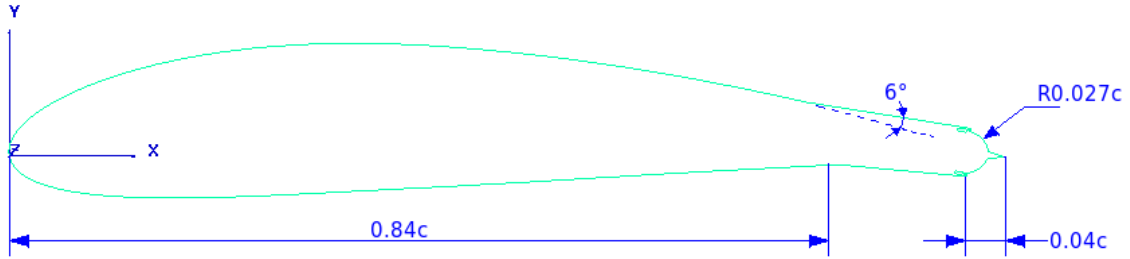
Figure 3.7: Modified NACA4415 section included in grid file

Number of nodes	1,838,780
Number of boundary faces	5,748,790
Number of interior faces	2,520,290
Total number of cells	1,609,800
Number of tetrahedra cells	0
Number of pyramids cells	0
Number of wedge cells	1,389,720
Number of Hexahedra cells	220,080

Table 3.4: Mesh details

the initial condition was set based on the minimum value that allows the production term to generate eddy viscosity close to the airfoil surface. This value was set by trial and error to $\tilde{\nu}_{initial} = \nu/1000$. A similar process to set the initial condition for the eddy viscosity was used by Shur et al [106].

The boundary conditions used for the velocity are shown in figure 3.8. In the spanwise direction periodicity was imposed, so that from the point of view of the aerodynamic properties the span is infinite. Over the airfoil surface (excluding the cavity that is explained in the next section) the boundary condition is no-slip i.e: $U_x = 0$, $U_y = 0$ and $U_z = 0$. A free boundary condition was used for the rest of the boundaries. In CDP v2.3 free boundary conditions were not available so they had

to be implemented. Free boundary conditions are either inflow or outflow boundary conditions, depending on the direction of the normal velocity of the previous time step. In particular:

if $(U \cdot n)_f <= 0$ then $U_f = U_{inlet}$ where U_{inlet} can be specified arbitrarily, otherwise determine the velocity at the boundary U_{outlet} by solving

$$\frac{\partial U_f}{\partial t} + U_{conv} \frac{\partial U_f}{\partial n} = 0 \qquad (3.26)$$

i.e.

$$U_{outlet} = U_f^n - \frac{U_{conv} \Delta t}{\Delta n}(U_{cv} - U_f)^n \qquad (3.27)$$

Where Δn represents the normal distance between the cell center and the boundary while U_{conv} is the average velocity at the assigned free boundary and computed as

$$U_{conv} = \frac{\sum_{f=1}^{nf} U_f A_f}{\sum_{f=1}^{nf} A_f} \qquad (3.28)$$

For the SA equation, the boundary conditions are very similar to the NS equation i.e: Periodic boundary conditions in the z direction, over the airfoil surface (including the synthetic jet cavity) the boundary condition is Dirichlet ($\tilde{\nu} = 0$) and free boundary conditions are imposed on the rest of the boundaries.

3.5   Synthetic Jet Models

In this research two different models were used in the simulation of the synthetic jet actuators: a detailed time-resolved synthetic jet model and a synthetic jet model based on an empirical Reynolds stress field induced by the actuator.
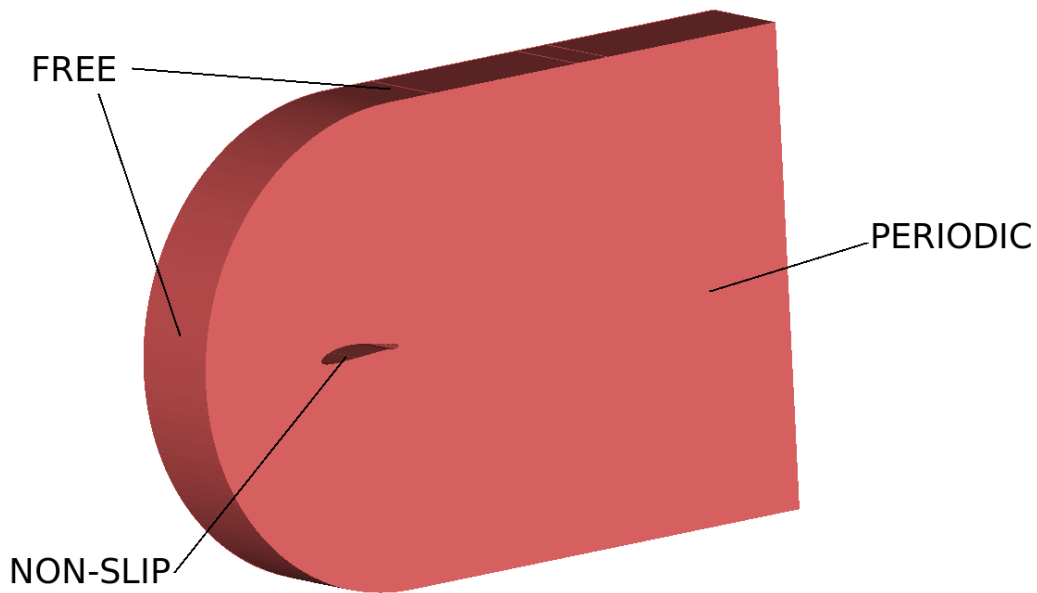
Figure 3.8: Three dimensional view of the domain with boundary conditions

3.5.1 Detailed Model

This model consists of resolving the spatial and temporal detail of the synthetic jet. Figure 3.9 shows the cavity of the synthetic jet, it is clear that the size of the cavity used in the model is smaller than the actual cavity used in the experiments (see figure 2.6). According to Mittal [83], it is important to reproduce as accurately as possible the dynamics of the flow at the synthetic jet outlet. However, in previous research [100], it was shown that the size of the cavity does not play an important role in determining the characteristics of the synthetic jet. In the dynamics of the flow in a synthetic jet, not only its outlet is important but also the small pipe or "neck" that connects the cavity to the synthetic jet outlet [83]. Based on these observations and on the actual design of the the synthetic jet, the exact dimensions of the synthetic
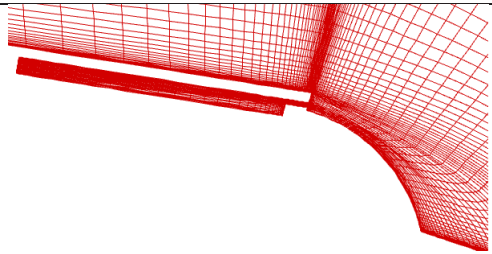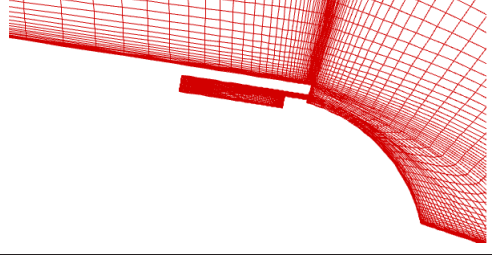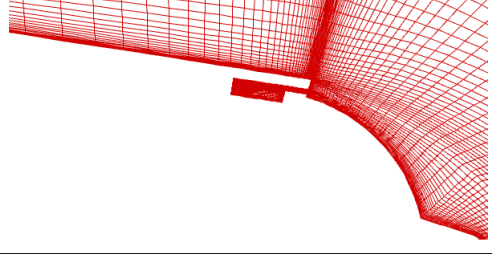
Cavity	C_m noact	C_m SSact	C_m PSact
	-0.088	-0.1029	-0.0675
	-0.089	-0.1021	-0.0678
	-0.089	-0.1031	-0.0681

Table 3.5: Different cavity sizes and moment coefficients at $\alpha = 0°$

jet outlet and neck were used, while the size of the cavity was reduced. Several computational experiments with different cavity sizes showed that the effect on the aerodynamic properties of the airfoil was negligible (See Table 3.5). In the cavity, the DDES model must behave as RANS, so the meshing process in this part of the domain followed the guidelines for the RANS region. Twenty grid points were used across the synthetic jet outlet to resolve the velocity profile. Figure 3.9 also shows the details of the mesh in the synthetic jet cavity.

In order to simulate the actuator diaphragm oscillation, a specified normal

56
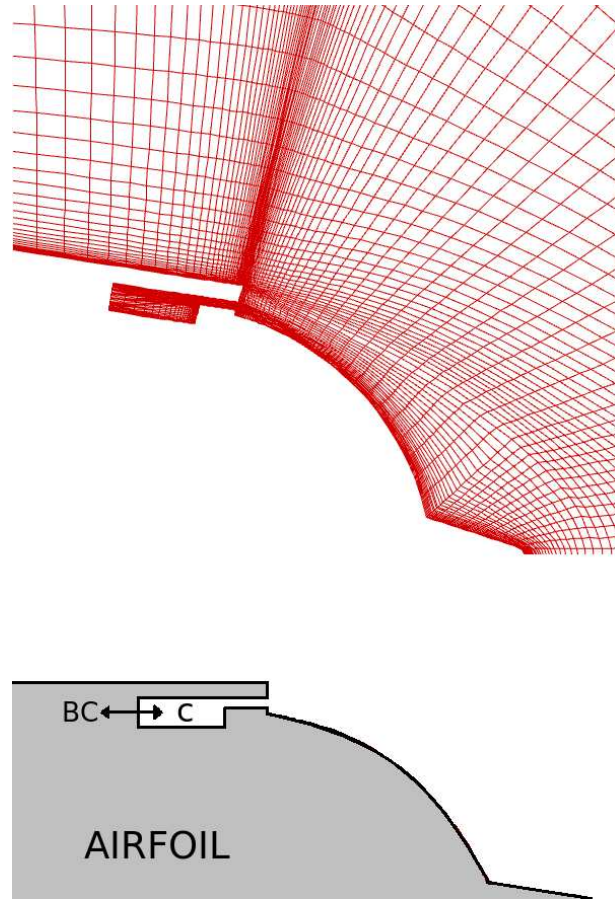
Figure 3.9: Geometry of the synthetic jet cavity (c) with mesh and detail of the boundary condition (BC)

velocity

$$U_n = A \sin 2\pi F^+ T \qquad (3.29)$$

was imposed on the left boundary of the cavity (see figure 3.9). In equation 3.29, A represents the amplitude of the Dirichlet boundary condition and it is determined by the momentum coefficient C_μ of the synthetic jet at the outlet. Since the experimental velocity at the synthetic jet outlet is about $40m/s \approx 1.333U_\infty$ and the ratio between
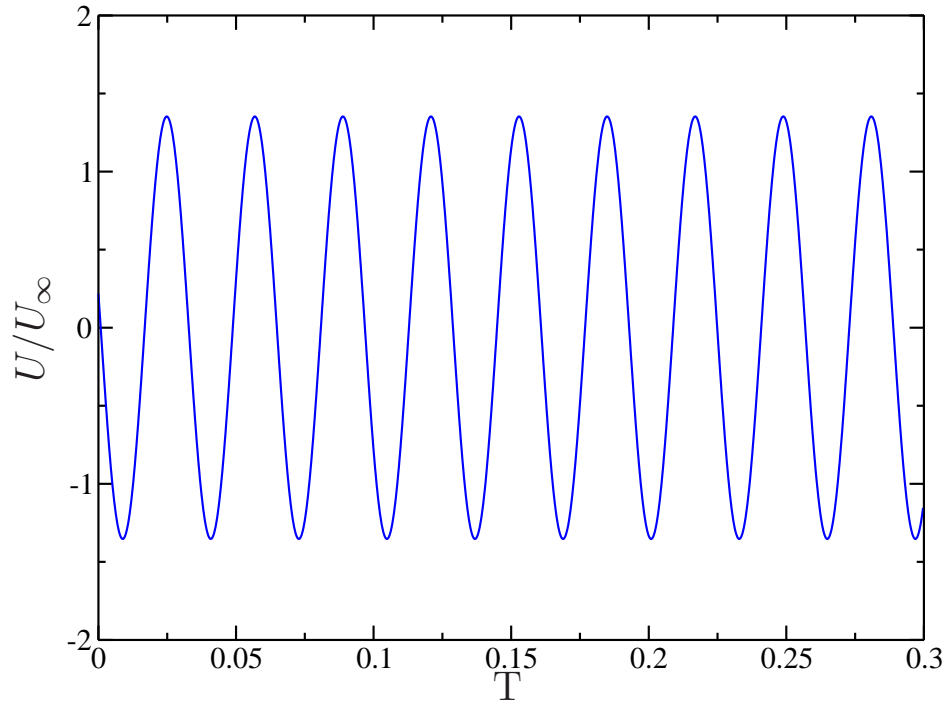
Figure 3.10: Non dimensional normal velocity at the synthetic jet outlet vs time

the synthetic jet outlet and the left boundary of the cavity is $\approx 1 : 3$, the amplitude of the boundary condition was set to approximately $0.38U_\infty$. Details about the actual values used for the amplitude of the boundary conditions of the pressure side and suction side actuators are discussed in chapter 4. Here, F^+ is the non-dimensional frequency (based on the chord length and the free-stream velocity) and it is set to 31.242 which for the experimental conditions is a frequency of 2050 Hz. Finally, T represents the non dimensional time i.e. $T = tU_\infty/c$. Figure 3.10 shows the evolution of the normal velocity at the synthetic jet outlet when the actuator operates in quiescent air. The amplitude (A) used in this simulation was $0.38U_\infty$ and the computed RMS velocity is about $1.2U_\infty$.

Boundary conditions are also necessary for the eddy viscosity. The amount of eddy viscosity that is ejected from the synthetic jet plays an important role in the flow downstream. In practice, $\tilde{\nu}$ is set to zero in all the cavity boundaries but this is still a topic under investigation in the numerical simulation of synthetic jets [100].

3.5.2 Reynolds Stress Synthetic Jet Model (RSSJ)

This ad hoc model is based on the fact that the actuation frequencies are high in comparison to relevant flow time-scales, which can be inferred from the fact that in order to achieve effective flow control the difference between the characteristic flow frequency and the actuation frequency must be about one order of magnitude [74]. The time stepping in the detailed model is limited by the actuation frequency, so in order to be able to advance faster in time a model based on the averaged Reynolds stress field induced by the synthetic jet is proposed. The averaged Reynolds stress field of the synthetic jet can be obtained from computational results of the detailed model. Figure 3.11 shows the time averaged difference of the $\overline{u'u'}$[7] Reynolds stress component between flows with the actuator on and off.

It is clear that the Reynolds stress field is concentrated in spots or blobs, which is important to parametrize the Reynolds stress field arising/induced by the jet. This parametrization was done by using simple mathematical exponential functions to

---

[7]Henceforth $\overline{u'u'}$, $\overline{u'v'}$ and $\overline{v'v'}$ are the nondimensional Reynolds stress components. i.e: $\frac{\overline{u'u'}}{U_\infty^2}$, $\frac{\overline{u'v'}}{U_\infty^2}$ and $\frac{\overline{v'v'}}{U_\infty^2}$ respectively
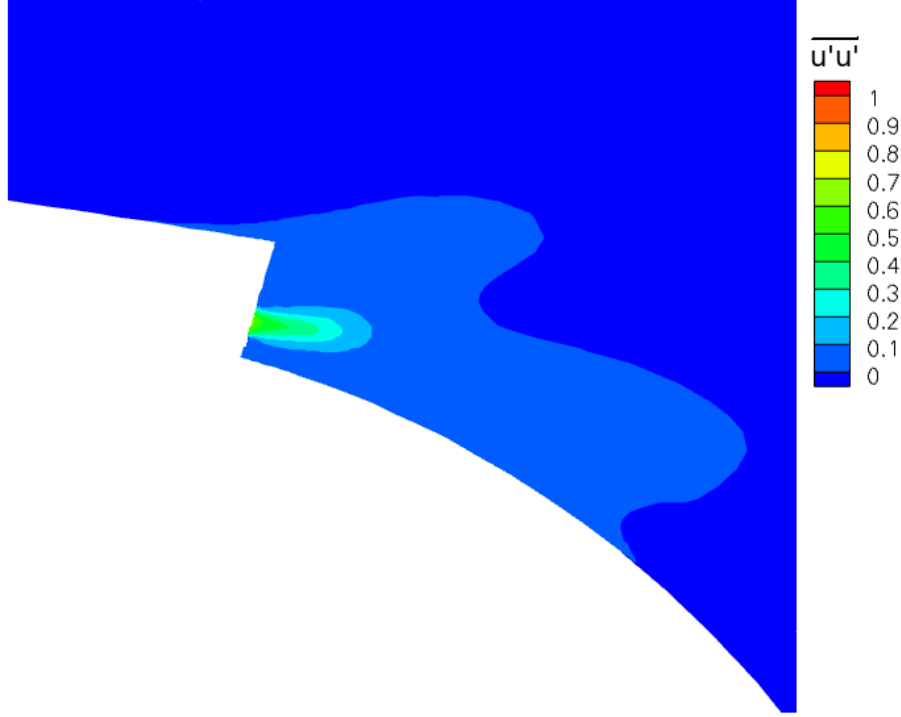
Figure 3.11: Averaged difference of the $\overline{u'u'}$ Reynolds stress component at $\alpha = 0°$, $Re = 1 \times 10^6$ and full actuation (Detailed model - SS actuator)

mimic the computational (detailed model) Reynolds stress field e.g:

$$\overline{u'u'} = \sum_{i=1}^{n} \Gamma_i e^{\hat{x} \cdot M_i \hat{x}} \tag{3.30}$$

In this example, the parametrized $\overline{u'u'}$ component of the Reynolds stress field is composed from n different exponential functions. n depends on the number of spots (blobs) of $\overline{u'u'}$ needed, for example from figure 3.11 three spots are enough to mimic the $\overline{u'u'}$ field obtained from the detailed simulations. In equation 3.30, Γ_i determines the $\overline{u'u'}$ spot strength, $\hat{x}$ is a vector of position in space ($x - X_i$ $y - Y_i$), where X_i and Y_i are the location of the center of the spot of $\overline{u'u'}$. Finally, M_i is a matrix given

by

$$M_i = \begin{pmatrix} \cos\theta_i & -\sin\theta_i \\ \sin\theta_i & \cos\theta_i \end{pmatrix} \begin{pmatrix} \lambda_i & 0 \\ 0 & \omega_i \end{pmatrix} \begin{pmatrix} \cos\theta_i & \sin\theta_i \\ -\sin\theta_i & \cos\theta_i \end{pmatrix} \tag{3.31}$$

Where λ_i and ω_i control the $\overline{u'u'}$ spot size while θ_i controls the orientation. Once all the components of the Reynolds stress are parametrized, its divergence is taken and then this result is introduced as a momentum source in the Navier-Stokes solver. For a given Reynolds number, the magnitude of the different numerical parameters (Γ_i, λ_i, ω_i and θ_i) of the RSSJ model not only depend on the jet strength[8] but also on the angle of attack. More details about the RSSJ implementation are given in chapter 4.

In order to use this model in a dynamic simulation, a local flow field variable must control the model numerical parameters. The pressure change (Δp) upstream of the synthetic jet outlet was selected as the control variable. Figure 3.12 shows the position of four pressure probes used to estimate Δp along the ramp upstream the synthetic jet outlet. Probes 1 and 3 are located at the beginning of the ramp while probes 2 and 4 are located half way along the ramp length. For the suction side actuator the control variable is determined from the difference in the measurements between probe 1 and probe 2 ($\Delta p_{SS} = P_1 - P_2$), while the pressure side is found from the difference between probes 3 and 4 ($\Delta p_{PS} = P_3 - P_4$).

Δp_{SS} and Δp_{PS} oscillate in time with the shedding frequency, requiring that a moving average technique [104] be employed. Such technique consists on solving a

---

[8]Jet strength (JS) is a nondimensional parameter which is 1 for full actuation and 0 for no actuation
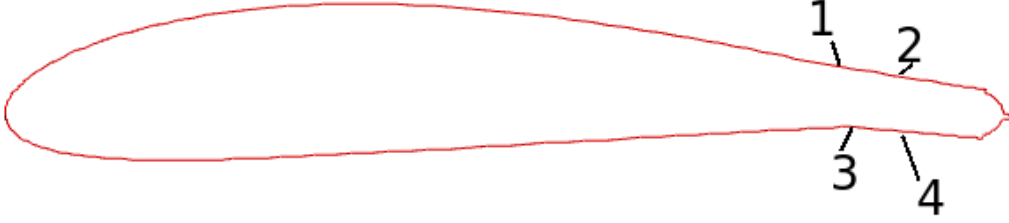
Figure 3.12: Pressure probes position

differential equation for the average $(\bar{\Delta}p)$

$$\frac{d\bar{\Delta}p}{dT} = \frac{1}{\hat{t}}(\Delta p(T) - \bar{\Delta}p) \tag{3.32}$$

Where $\hat{t}$ is a non-dimensional time constant set to 1 for static cases, so that shedding and actuation frequencies were filtered. Figure 3.13 shows the variation of Δp_{SS}. It is clear that for no actuation the peak-to-peak value of Δp_{SS} is about 0.012 and that the moving average captures the average value of this oscillation. It is also clear that when the actuator is active there is an increment of the averaged Δp_{SS} of approximately 0.01 in the case of full actuation and 0.004 for half-actuation with respect to the unactuated case.

By estimating Δp for different levels of actuation (using the detailed model), it is possible to obtain a scatter map that correlates the model variable with Δp and levels of actuation. By means of a radial basis function interpolation [95], a map for each model variable was created. Figure 3.14 shows an example of the map used for the variable Γ_1 of the $\overline{u'u'}$ component of the suction side actuator Reynolds stress field. These maps are introduced into the CFD code so that at each time step the model computes the magnitude of the model parameters based on the synthetic jet

62
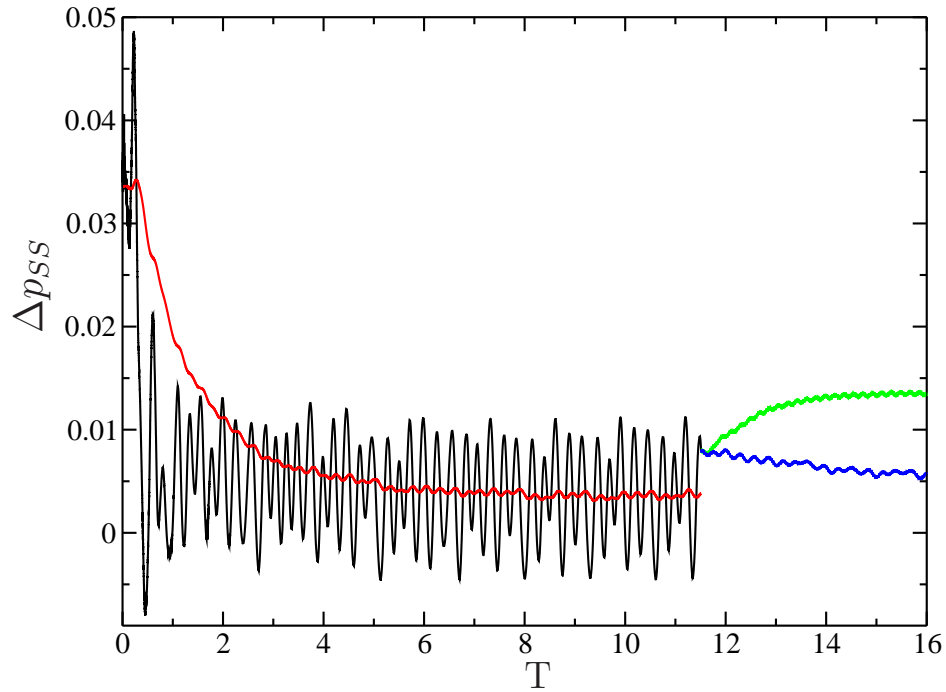
Figure 3.13: Δp_{SS} at $\alpha = 0°$. No actuation $-$ No actuation average $-$ Full SS actuation average $-$ Half SS actuation average $-$

strength and Δp. Section 4.3.4 gives more details about tuning the RSSJ model for this specific type and application of tangential synthetic jets.

3.6   Importance and Contribution

The computational tools described in the previous sections address three significant research issues:

- Support for the development of flow control actuators for UAVs (in the context of the AVOCET project).

- Application and development of synthetic jet models for use in flow control
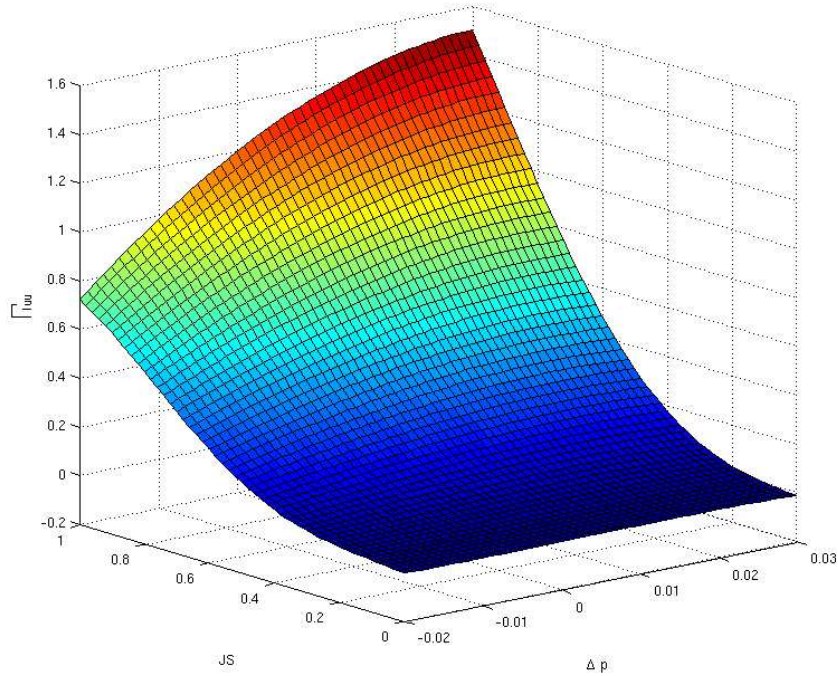
Figure 3.14: Map of the variable Γ_1 used in the RSSJ model

simulations.

- Implementation and application of hybrid turbulence models in kinetic energy conserving algorithms.

This research represents important support for the development and application of flow control actuators for UAVs, since it provides detail information on the controlled flow dynamics which is useful in the controller design and sensors placement. In the case of the controller design, valuable information can be obtain from this CFD study to support the design of the outer-loop controller (See section 2.4).

64

Figure 3.15 [9] shows a schematic of the outer controller architecture. It has two important parts the adaptive neural network and the low (or Reduced) order reference model. The adaptive neural network compensates the modeling errors, nonlinearities of the synthetic jet actuators and unmodeled dynamics. Also it increases the robustness of the PID controller while the reduced order reference model tries to model the effects of the trapped vorticity and massively separated vortex structures when they exist [75]. A correct design and validation of a reduced order model depends on the detailed information on the vorticity field, which can be provided by this CFD study when it is not available from experimental observation. For example, the validation of a reduced model in an impulsively started flow can only be performed against a higher order model [122], the evolution of the vorticity flux very close to the airfoils trailing edge is another quantity that can best be obtained from a CFD simulation. Sensor placement plays an important role in the performance of the closed-loop controller, the higher fidelity solutions provide by this computational study help decide the placement of the pressure and flow direction sensors.

Most of the synthetic jet models used by the CFD community are required to solve the frequency of actuation (see section 1.2). Experimental observation has shown that effective control is achieved with actuation frequencies an order of magnitude larger than the natural shedding frequency of the body [4]. The shedding frequency of the flow around an airfoil depends on the angle of attack, airfoil section and the Reynolds number. Nevertheless, for a fixed Reynolds number ($\approx 1 \times 10^6$) and airfoil wing (NACA 4415) the Strouhal number based on the chord has been found to be $O(1)$

---

[9]Courtesy of Kutay and Muse (GA Tech)
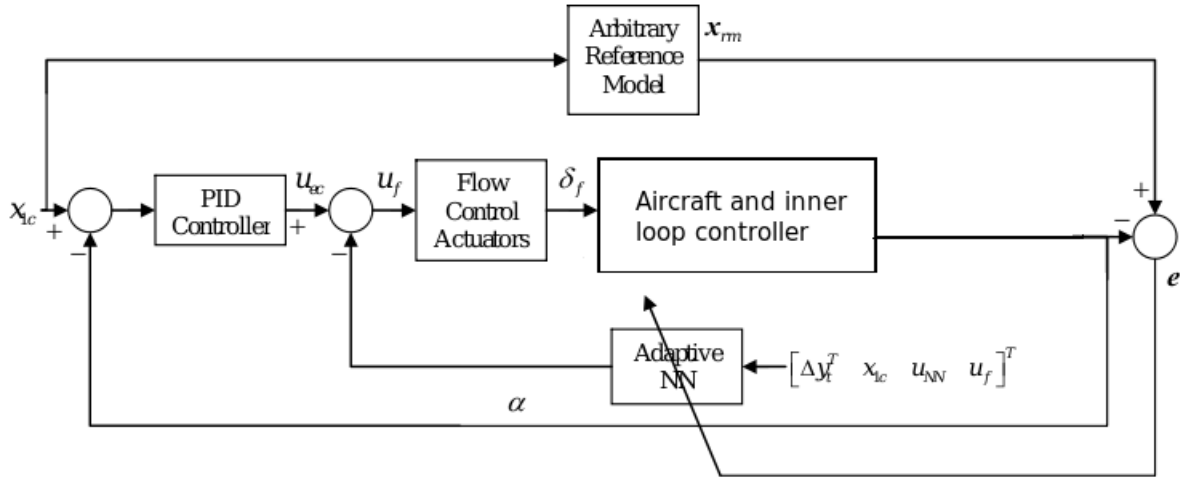
Figure 3.15: Outer loop controller architecture.

for a wide range of angles of attack [13] [71]. This means that an effective actuation frequency should have Strouhal number of order $O(10)$ but the experimental plunging or pitching (maneuvering) frequency achieved in the wind tunnel is about two to three orders of magnitude smaller than the actuation frequency i.e. $O(0.01)$ so that there is a difference of three to four orders of magnitude between the actuation frequency and the maneuvering frequency. A detailed simulation of this problem is computationally expensive due to the constraint in the time step imposed by the synthetic jet model. A new model based on the averaged Reynolds stress field induced by the synthetic jet (described in section 3.5.2) can be used to overcome this constraint and allows the simulation to advance as fast as possible without compromising the accuracy and stability of the computational results. Despite the fact that a model based on the Reynolds stress field does not capture the detail of the unsteady flow field induced by the actuator, the development of such a synthetic jet model represents an

important advance in the simulation of flow control problems (especially on problems in which average aerodynamic properties are the final objective) since it reduces the computational cost in comparison to a time-resolved simulation.

Finally, another important aspect of this work is the implementation and application of a hybrid RANS/LES model in a state of the art nearly energy conserving LES code. No references have been found so far in this specific application of hybrid models, which represents an alternative to wall treatment LES models. This implementation provides feedback information (such as stability, positivity preservation of the eddy viscosity, mesh requirements, etc) that could be useful for future model improvements and for the future development of turbulent models in energy conserving algorithms. For these reasons, this work represents an important contribution to the field of computational aerodynamics flow control and in general to the CFD research community.

Chapter 4

Numerical Results and Validation

Numerical and computational results are presented in this chapter as well as validation and comparison with experimental data. First, the available experimental data is described and discussed. Methods to correct the experimental data for the wall interference, solid and wake blockage, streamline curvature and infinite aspect ratio are then explained, since such corrections are needed to facilitate comparison to simulations. Two wing sections were considered in this study: NACA4415 and Dragon Eye. The flow around each airfoil was simulated in three different scenarios: unmodified section, modified section unactuated and modified section with actuation. For all the simulations the vorticity fields (instantaneous and time averaged) and the aerodynamic properties of the airfoil are studied and analyzed. All vorticity fields shown in this chapter are spanwise averaged unless otherwise specified. The effects of the actuation in the vorticity field as wells as in the aerodynamic properties are shown and explained from both a qualitative and quantitative points of view. The advantages of the synthetic jet model based on the Reynolds Stress are presented and quantified as a reduction in the computational cost, including the performance of the RSSJ model in a dynamic simulation and its comparison with the detailed model.

4.1 Experimental data

Two different types of experimental data were used for the calibration and validation of the computational models: two dimensional velocity fields measured using PIV and integrated forces and moments. Instantaneous field data from PIV can be used to compute time-averaged or phase-averaged statistics. For steady experiments, there are two ways to determine the integrated aerodynamic properties of the airfoil: by measuring the pressure distribution over the airfoil or by measuring the forces and moments directly with the instrumentation available in the traverse structure [17]. Figure 4.1 shows an example of a time averaged experimental velocity field. In this case, multiple instantaneous PIV fields were used to compute the time-averaged velocity field (arrows) in a region close to the trailing edge of the airfoil. Based on this field, the vorticity field (contours) is computed with a simple second order finite difference approximation. Unfortunately, the details of the flow near the pressure side actuator can not be captured due to the position of the laser relative to the airfoil in this experimental set-up.

4.2 Experimental data correction

The numerical results obtained from the simulations are commonly called "section characteristics" since an infinite aspect ratio wing and free boundary conditions are simulated, while experimental data is usually known as "wing characteristics" [1]. Section characteristics just depend on the airfoil shape, in contrast wing characteristics are highly influenced by the wing plan form and aspect ratio. To be able to compare and validate the computational results, experimental data must be corrected

69
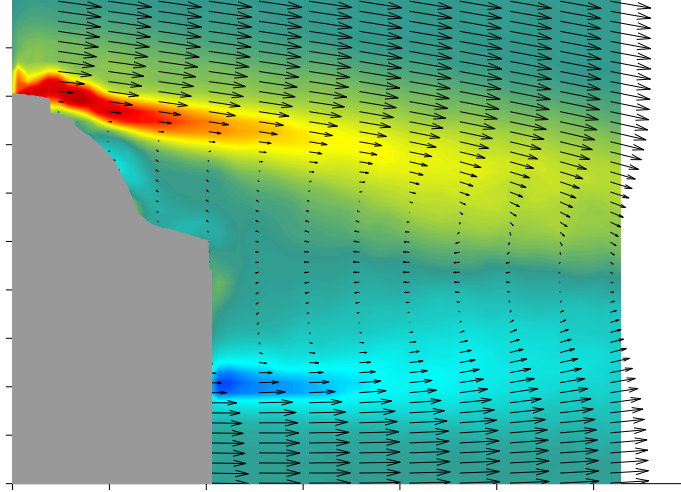
Figure 4.1: Sample experimental PIV data.

and take into account the solid and wake blockage, wall interference, streamline curvature and finite aspect ratio. The correction procedure followed here is based on the methodology proposed by Barlow et al [7] and Jacobs et al [64].

4.2.1 Solid and wake blockage correction

In free flight the ratio between the frontal area of the wing to the free stream cross sectional area is zero, but in a wind tunnel, especially in a closed one, this ratio is finite typically $O(10^{-2})$. As a result, this solid blockage increases the surface stresses and the free stream velocity close to the airfoil in comparison with free-air conditions. A solid blockage correction can be determined as an adjustment to the dynamic pressure:

$$\epsilon_{sb} = \frac{K_1 \xi_1 V_{wing}}{C^{3/2}} \tag{4.1}$$

70

Where K_1 is a body-shape factor that depends on the type of airfoil, ξ_1 depends on the wind tunnel section, V_{wing} is the wing volume and C is the wind tunnel test section area. Details about how to estimate K_1 and ξ_1 can be found in reference [7]. On the other hand wake blockage is related to the finite size of the wake in the wind tunnel (i.e the wake is thinner and shorter in comparison to free flight) the primary effect of which is to augment the measured drag. This correction is computed following Maskell's method [78]:

$$\epsilon_{wb} = \frac{A_{pf}}{4C} C_{du} \tag{4.2}$$

Where A_{pf} is the airfoil plan form area and C_{du} is the measured (uncorrected) drag coefficient. The correction for the drag coefficient is given by

$$\Delta C_{Dw} = -\frac{K_1 \xi_1 V_{wing} C_{Du}}{C^{3/2}} \tag{4.3}$$

Equations 4.2 and 4.3 are used for low angles of attack. For massively separated flows, a different set of corrections must be applied [7]. The solid and blockage correction may be summed and then used to correct the measured dynamic pressure $\left(q = \frac{\rho A V^2}{2}\right)$.

$$\epsilon_t = \epsilon_{sb} + \epsilon_{wb}$$

$$q_c = q(1 + \epsilon_t)^2 \tag{4.4}$$

The wake blockage correction requires experimentally determining the drag coefficient, which may be available in some experiments. In case C_d is not available an alternative method to correct both effects can be estimated using this empirical equation [7]

$$\epsilon_t = \frac{F}{4C} \tag{4.5}$$

Where F is the model frontal area which depends on the airfoil thickness and the angle of attack. Once the dynamic pressure q_c is corrected, then the pressure, drag, lift and moment coefficient can be estimated.

$$
\begin{aligned}
C_{db} &= \frac{C_{du}}{(1 + \epsilon_t)^2} \\
C_{lb} &= \frac{C_{lu}}{(1 + \epsilon_t)^2} \\
C_p &= \frac{C_{pu}}{(1 + \epsilon_t)^2} \\
C_{mb} &= \frac{C_{mu}}{(1 + \epsilon_t)^2}
\end{aligned}
\tag{4.6}
$$

Where C_{du}, C_{lu}, C_{pu} and C_{mu} represent the measured (uncorrected) drag, lift, pressure and moment coefficients respectively.

4.2.2 Wall interference correction

The streamlines in a cross section of the wind tunnel are very different from those in free flight, due to the presence of the walls. Basically, the streamlines in the wind tunnel are confined by the walls while in free flight the streamlines extend to infinity. The theory for this correction was initially developed by Prandtl [94] and Glauert [47] and it is based on the method of images widely used in potential flow theory. The idea is to create a three-dimensional image system for a pair of trailing and a lifting line vortices, this correction is highly dependent on the wind tunnel cross sectional area and the type of lift distribution along the airfoil's span. The presence of the walls reduces the effective angle of attack and the drag coefficient, corrections

for which are given by:

$$\alpha_w = \alpha_u + \eta \frac{A_{pf}}{C} C_{lb} 57.3$$

$$C_{dw} = C_{db} + \eta \frac{A_{pf}}{C} C_{lb}^2 \tag{4.7}$$

Where α_w is the wall interference corrected angle of attack (in degrees), C_{dw} is the corrected drag coefficient, α_u is the measured angle of attack (in degrees) and η is an experimental coefficient that depends on the shape of the test section, the type of wind tunnel, the type of test section, the type of lift distribution on the model and the ratio between the airfoil span and the total width of the test section so that for the experimental set-up at Georgia Tech $\eta \approx 0.195$.

4.2.3 Streamline curvature correction

According to Von Mises [82], the three-dimensional wing theory does not predict any influence of the aspect ratio in the position of the aerodynamic center or the moment coefficient (C_m), nevertheless the presence of the top and the bottom walls modify the curvature of the streamlines affecting the magnitude of the moment coefficient. This change in the streamlines makes the body appear to have a larger chamber while increases the lift, moment and angle of attack in comparison to free flight which are respectively corrected as

$$\alpha_{sc} = \alpha_w + \xi_2 \eta C_{lb} \frac{A_{pf}}{C} 57.3$$

$$C_l = C_{lb} - \xi_2 \eta C_{lb} \frac{A_{pf}}{C} 57.3a \tag{4.8}$$

$$C_m = C_{mb} - 0.25 \xi_2 \eta C_{lb} \frac{A_{pf}}{C} 57.3a$$

Where α_{sc} is the streamline curvature corrected angle of attack (in degrees), C_l is the corrected lift coefficient, C_m is the corrected moment coefficient at quarter chord, a is the experimental wing lift curve slope and ξ_2 is a numerical parameter that depends on the point at which the moment is measured, the type of wind tunnel and the wind tunnel sectional area.

4.2.4   Infinite aspect ratio correction

Once all the corrections due to the wind tunnel walls are computed, the infinite aspect ratio has to be taken in account. The effect of the aspect ratio on the lift and drag coefficients was also first investigated by Prandtl [94]. Early wind-tunnel experiments showed that the slope of the lift-curve increases while the slope of the drag curve decreases as the wing aspect ratio increases [1]. Prandtl was able to demonstrate that for a wing with elliptical lift distribution, the drag coefficient and the angle of attack for wings of different aspect ratios could be correlated by simple mathematical expressions. These expressions were extended to rectangular distributions [64], so that the corrected angle of attack and drag coefficient are given by

$$\alpha = \alpha_{sc} - \frac{C_l(1+\xi)57.3}{\pi R}$$
$$C_d = C_{dw} + \frac{C_l^2(1+\zeta)}{\pi R} \tag{4.9}$$

Where ξ and ζ are factors that correct the span loading distribution for an airfoil with rectangular plan form. R is the actual aspect ratio of the airfoil, which is about 2 for the experimental set-up at Georgia tech.

4.3 NACA4415

This section shows the numerical results for different cases at fixed angles of attack for the NACA 4415 airfoil. In order to test the DDES implementation and the code performance, initially several simulations of a NACA 4415 were conducted in a wide range of angles of attack (section 4.3.1). Then, simulations of the modified NACA 4415 (no actuation) were performed and validated against experimental results (section 4.3.2). Finally, a set of simulations of the modified NACA 4415 airfoil at full actuation were performed using the detailed model (section 4.3.3) and the Reynolds Stress Synthetic Jet model (section 4.3.4).

4.3.1 Unmodified

A total of eleven simulations were performed with the unmodified NACA 4415 airfoil, nine of them were performed to validate the CFD code with legacy data while the rest were intended to compare the results against experimental data obtained at GA Tech and to test the performance of the DDES implementation at high angle of attack. The conditions for the first set of computational experiments were a wide range of angle of attack ($-9°$ up to $12°$) and $Re = 2.0 \times 10^6$. Figures 4.2 and 4.3 show lift, moment (at quarter chord) and drag coefficient results along with legacy data for this airfoil [2] [65] [1]. Good agreement is evident in the region between $\alpha = -9°$ and $\alpha = 10°$. In this range, the turbulence model mostly behaves as a RANS model since there is no massive flow separation. The slope of the C_l and C_m curves is well predicted by the numerical simulations. In the stall regime ($\alpha > 10°$), the wake is 3-dimensional and computational results strongly depend on the spanwise domain

75
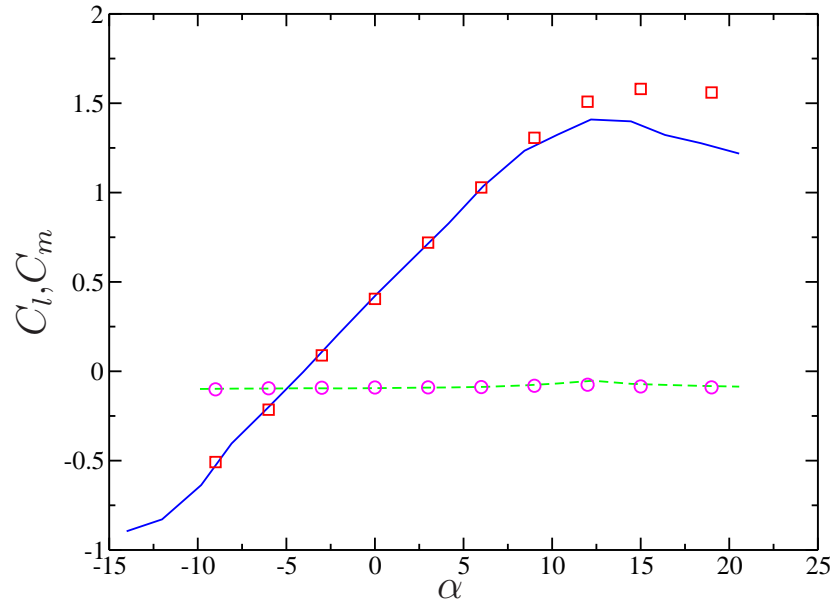
Figure 4.2: NACA4415 computational and experimental[1] lift and moment coefficients. C_l exp— C_l comp □ C_m exp-- C_m comp ○

extent[18]. Discrepancies of 20% between computational and experimental results at high angle of attack have been observed when the spanwise domain extent is c and better agreement were achieved with spanwise domains $> 2c$[18]. Since this study is focused on low angle of attack simulations, it was considered that a $1c$ spanwise length is sufficient to achieved satisfactory results.

The polar plot (figure 4.3) shows some disagreements in the drag coefficient between the computational and experimental results. This observation is common in the computational prediction of drag coefficients due to errors in the prediction of the skin friction by the turbulence model RANS mode.

Two more tests at 19° and 30° with a $Re = 5.7 \times 10^5$ were performed to match the experiments at Georgia Tech and to test the implementation of the turbulent
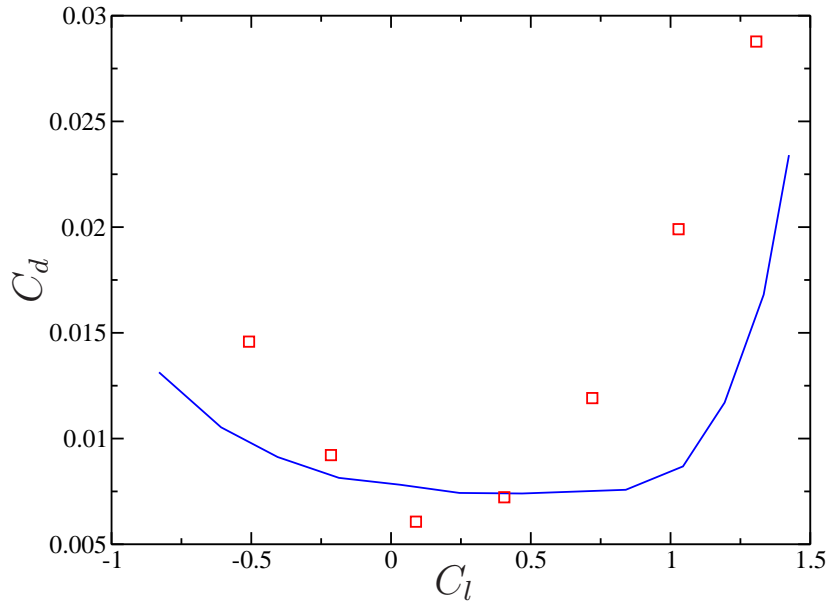
Figure 4.3: Comparison of the polar plot with legacy data (NACA4415). Exp— Comp □

model in a massively separated flow (see figure 3.3). Results at angle of attack of 19° also show good agreement with other simulations and experiments at the same conditions [69] [71] [40]. Figure 4.4 shows time-averaged vorticity fields of that simulation (left) and a comparison with the experimental PIV data (right) [15]. Even though the experimental PIV data shows smaller scales with very strong vorticity in the separation bubble and missing data, the simulation and experiment are in good agreement regarding separation location (at $\frac{x}{c} \approx 0.3$) and the structure of the separation bubble.

Figure 4.5 shows the time-averaged pressure coefficient as a function of $\frac{x}{c}$, the pressure coefficient plot is similar to the experimental one [15] with some small discrepancies in the peak pressure close to the leading edge and the pressure distribution
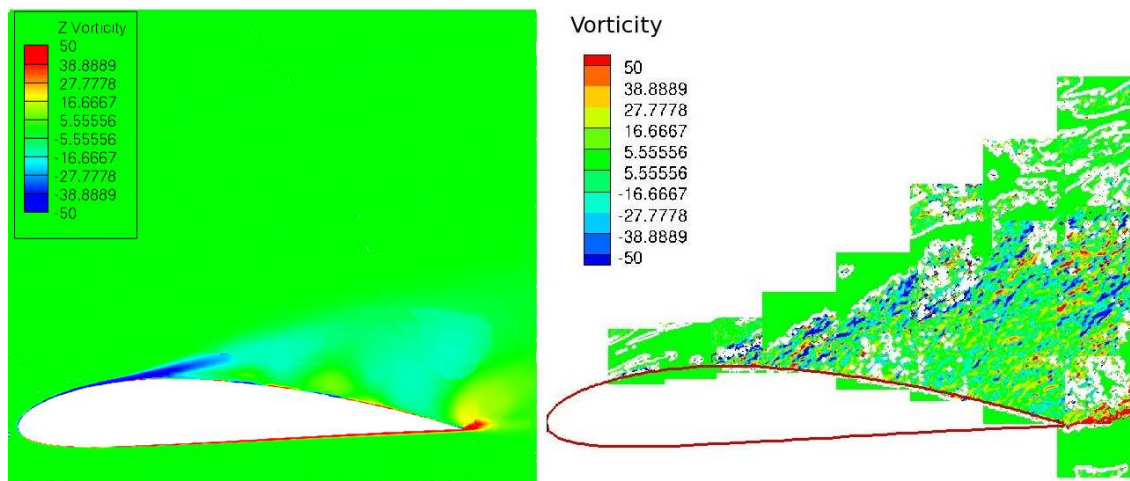
Figure 4.4: Time-averaged spanwise vorticity at $\alpha = 19°$ computational (left) experimental (right)

on the suction side of the airfoil.

4.3.2 Modified unactuated

Several static cases of the modified NACA4415 without actuation were performed, for these simulations the Reynolds number was fixed at 9×10^5 and the angle of attack was changed from $0°$ up to $15°$ to match the experiments at Georgia Tech. Figure 4.6 shows a comparison between the experiments and the computational simulation of the time averaged spanwise vorticity close to the trailing edge at $\alpha = 0°$. Good agreement is observed especially in the magnitude of the vorticity, thickness of the shear layer formed at the end of the actuator ramp and the size of the recirculation regions formed downstream of the trailing edge. An observable difference is that the computational results show stronger concentration of vorticity close to the airfoil surface. In particular a co-rotating vortex in each side of the airfoil close to

78
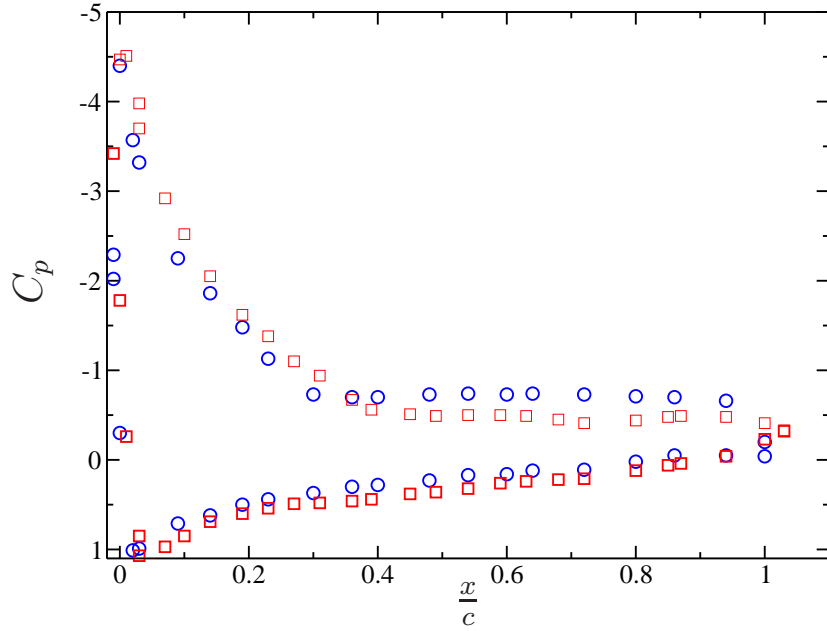
Figure 4.5: NACA4415 C_p as a function of $\frac{x}{c}$ at $Re = 5.7 \times 10^5$ and $\alpha = 19°$. Experimental ○ Computational □

the trailing edge, this vortex does not appear in the PIV measurements but it is a flow feature that should be expected. This difference can be attributed to the CFD model higher resolution close to the airfoil compared to the PIV measurements. The number of grid points in this region in the CFD model is about an order of magnitude greater than the highest PIV resolution measurement.

Figure 4.7 shows the instantaneous eddy viscosity field and vorticity field for an angle of attack of 0°. As expected, the eddy viscosity is strong in the boundary layers, where the generation of eddy viscosity is high, and far from the walls the eddy viscosity behaves as a convected scalar that is diffused downstream. The vorticity field shows a clear vortex street in the wake in which the distance between vortical structures is $\frac{x}{c} \approx 0.24$ and there is a slight asymmetry due to the lack of symmetry
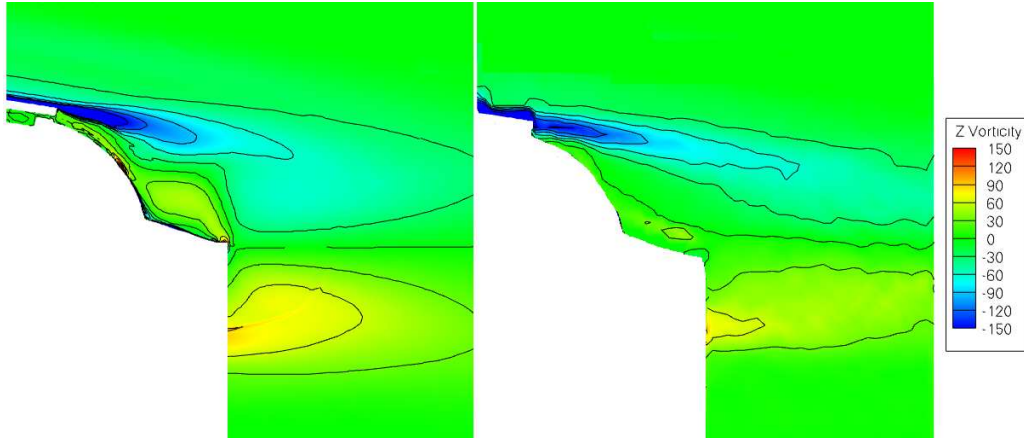
Figure 4.6: Averaged spanwise vorticity modified NACA4415 at $\alpha = 0°$. Computational (left) Experimental (right).

in the airfoil profile.

The Strouhal number based on the chord length

$$S_t = \frac{f_{shed}c}{U_\infty} \tag{4.10}$$

can be estimated by performing a zero-crossing measurement of the evolution of one the aerodynamic properties. Figure 4.8 shows the evolution of the moment coefficient in convective time units $(T = \frac{tU_\infty}{c})$. It was found that ten periods occurred in $\Delta T \approx 2.38$, so that $S_t \approx 4.2$. This result is in fairly good agreement with the experimental one of approximately 3.9[17].

Figures 4.9 and 4.10 show the lift, moment (at quarter chord) and drag coefficients for these simulations, in which a very good agreement between the experimental and computational results is observed. The C_l curve slope is slightly underpredicted by the CFD model, and the C_m curve in the experiments is flat while in the computa-
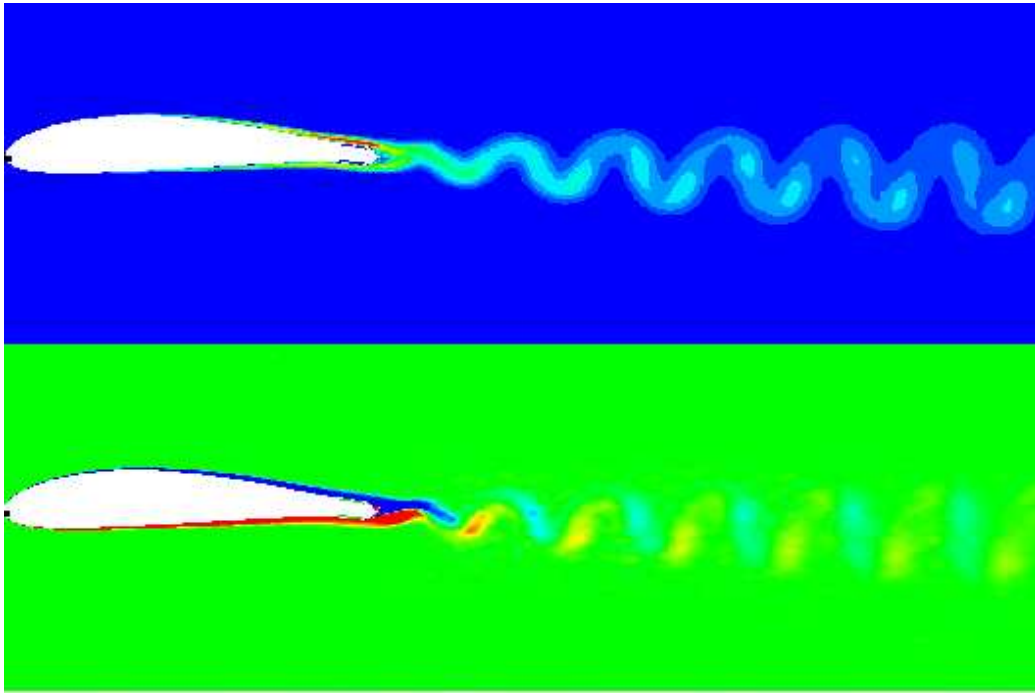
Figure 4.7: Eddy viscosity (top) and vorticity field (bottom) at $Re = 9 \times 10^5$ and $\alpha = 0°$. (modified NACA4415)

tions the slope is slightly negative. In this case C_d results are in very good agreement with experiments.

Figure 4.11 shows a comparison of the computational results between the unmodified and modified NACA4415 profile. While the C_l curve slope is not strongly influenced by the geometrical modification of the airfoil profile, there is a radical change to the C_m curve slope. Changes in $\frac{\partial C_m}{\partial \alpha}$ have been observed experimentally by De Salvo et al [37] with similar actuators but on a different airfoil section. An important numerical parameter that can be computed from these results is $\frac{\partial C_m}{\partial C_l}$ at low angle of attack, which is related to the location of the aerodynamic center of the wing
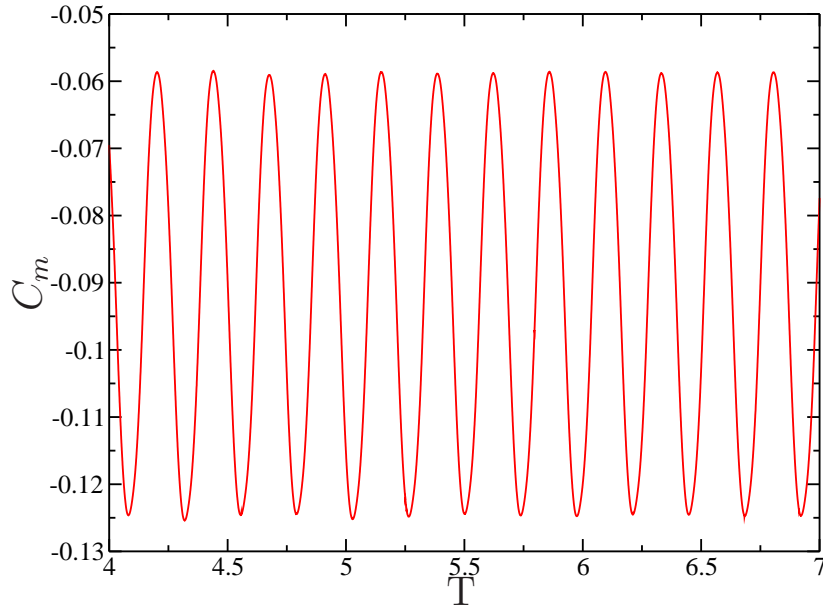
Figure 4.8: Evolution of the moment coefficient at $Re = 9 \times 10^5$ and $\alpha = 0°$. (modified NACA4415)

section. For the unmodified case $\frac{\partial C_m}{\partial C_l} \approx 0.0035$, so that the aerodynamic center is located at $x/c \approx 0.245$ which is very close to the experimental result of 0.242[2][65][1]. In the modified case $\frac{\partial C_m}{\partial C_l} \approx -0.022$, meaning that the aerodynamic center is located at $x_{ac}/c \approx 0.272$. Based on these calculations, the aerodynamic center moved towards the trailing edge due to the geometrical modification of the airfoil section, this result is consistent with experimental observations (for a large group of NACA profiles) in which changes to the geometry such as trailing-edge included angle and airfoil thickness at $x/c = 0.9$ were investigated and found to have the aerodynamic center move forward, consistent with current results for the NACA4415 with actuators[97].

Figure 4.12 shows the pressure coefficient for both the unmodified and modified NACA 4415. A modification of the pressure distribution along the airfoil surface is

82
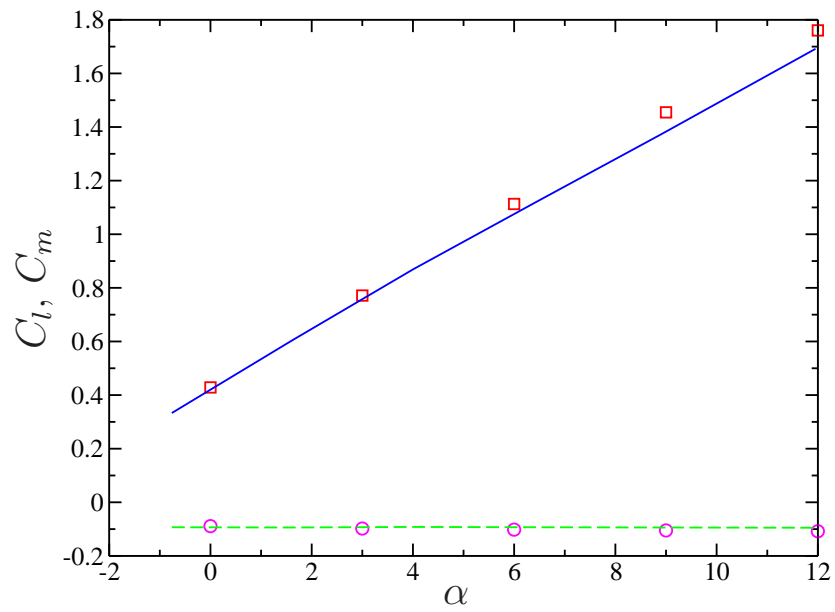
Figure 4.9: Lift coefficient for the modified NACA4415. (C_l comp □ C_l exp — C_m exp — C_m comp ○)
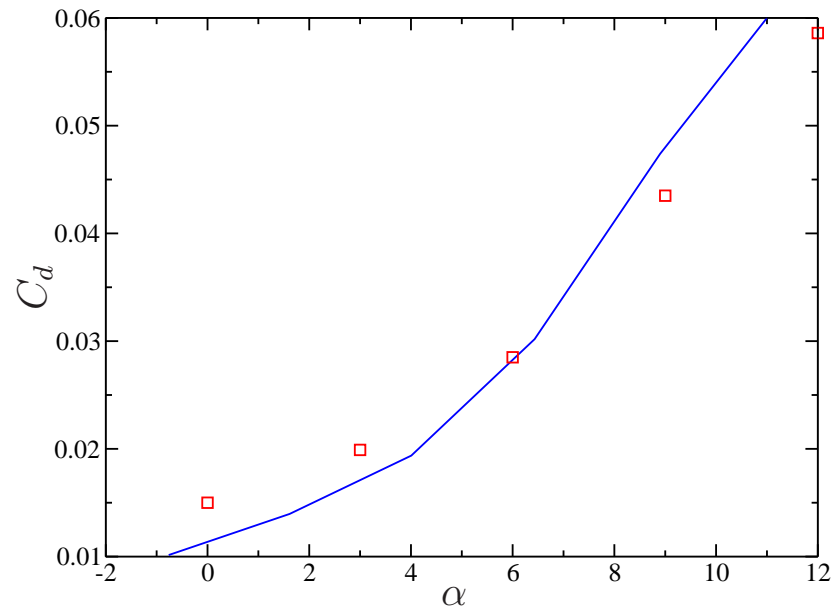
Figure 4.10: Drag coefficient for the modified NACA4415. (Comp □ Exp —)
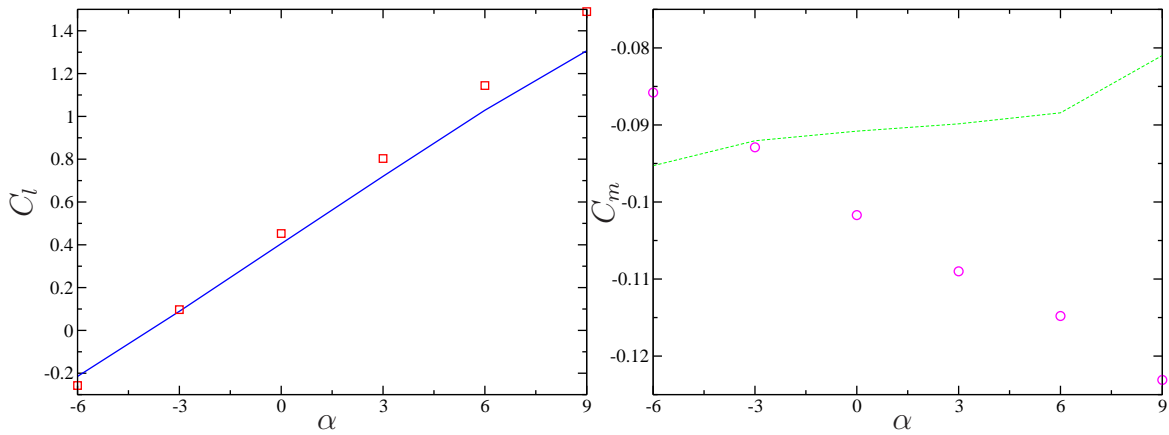
Figure 4.11: C_l and C_m vs α for the NACA4415 airfoil. C_l unmodified $-$ C_l modified $\square$ C_m unmodified $--$ C_m modified $\circ$

observed for $x/c > 0.7$ due to the actuator. There is a reduction of the pressure along the actuators ramp (due to a flow acceleration) and the pressure close to the trailing edge is reduced due to flow separation.

4.3.3 Modified Actuated - Detailed model

Numerical results obtained from the implementation of the detailed synthetic jet model on the modified NACA4415 airfoil are presented in this section. Two important numerical parameters are required in the boundary condition for the synthetic jet model (equation 3.29): the non-dimensional actuation frequency F^+ and the non-dimensional amplitude A. As was discussed in section 3.5.1, F^+ is 31.24 which corresponds to 2050 Hz in the experimental set-up at Georgia Tech. The amplitude A was set to match two experimental parameters the momentum coefficient (C_μ) for
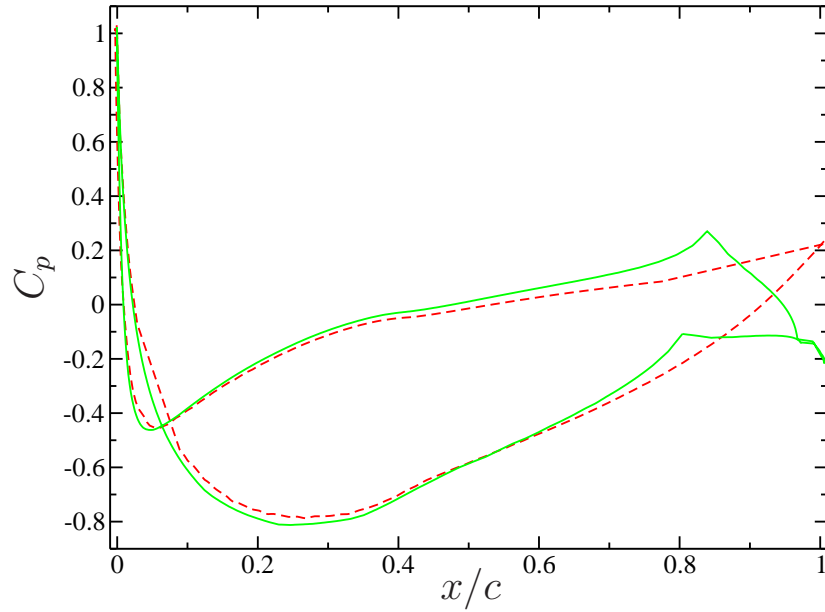
Figure 4.12: C_p comparison for the NACA4415 airfoil at $\alpha = 0°$. Unmodified $--$ Modified $-$

full actuation [1] which is $O(10^{-3})$ and the actuator effectiveness (ΔC_m), the latter being the most relevant. One disadvantage of this model is that the time stepping is constrained by the actuation frequency, a time step of $3 \times 10^{-4} \frac{c}{U_\infty}$ was used, which was chosen to yield about 100 steps per actuation cycle. But this results in a CFL number of only ≈ 9 which is small for this implicit time discretization on this mesh. The effects of the synthetic jet actuator on the vorticity field and the aerodynamic properties are of particular interest.

---

[1]Full actuation is defined by the maximum experimental voltage that could be applied to the piezoelectric elements of the synthetic jet and that produce an RMS velocity at the synthetic jet outlet of about $40 \frac{m}{s}$

4.3.3.1 Effects on the vorticity field

Both time average and instantaneous vorticity fields are examined here to gain information about the effects of the actuation on the flow. Figure 4.13 shows the time averaged vorticity contours close to the suction side actuator in which it is clear that the average effect of the synthetic jet is to bend the shear layer (formed at the end of the actuator ramp) towards the actuator coanda surface, which is related to changes in the size and shape of the recirculation regions formed downstream the trailing edge. This bending of the shear layer has been observed experimentally (see figure 4.14) and is associated with lift enhancement due to a local reduction of the pressure[16]. While the details of the near actuator mean streamlines are a bit different in the experiments and computations, the amount by which the extend streamline deflected is about the same. Another important change brought on by the actuation is the strength of the trapped vorticity close to the trailing edge. But, once again, the computational results show more vortical structures in this region than the experimental PIV data. This difference could be due to the higher resolution of the CFD compared to the PIV. The streamlines also show that the size of the recirculation region in the near wake ($\approx 0.04\frac{x}{c}$) is very similar to the experimental result and it is actually shorter that the recirculation region of the unactuated case which is $\approx 0.06\frac{x}{c}$ in both experimental and computational results (see Figure 4.6).

Figure 4.15 shows the time averaged vorticity field in the near wake with either the suction side or the pressure side actuators activated. The "symmetry" of the recirculation regions in the near wake shown in the unactuated case (see figure 4.6) is lost. For suction side actuation, the near wake shows a downwash compared
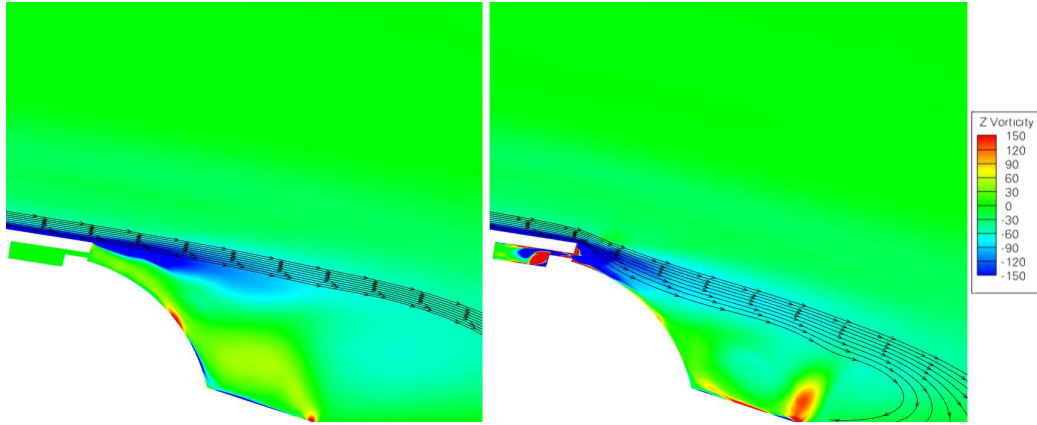
Figure 4.13: Time averaged vorticity field for the suction side actuator. No actuation comp (left) and full actuation comp(right)
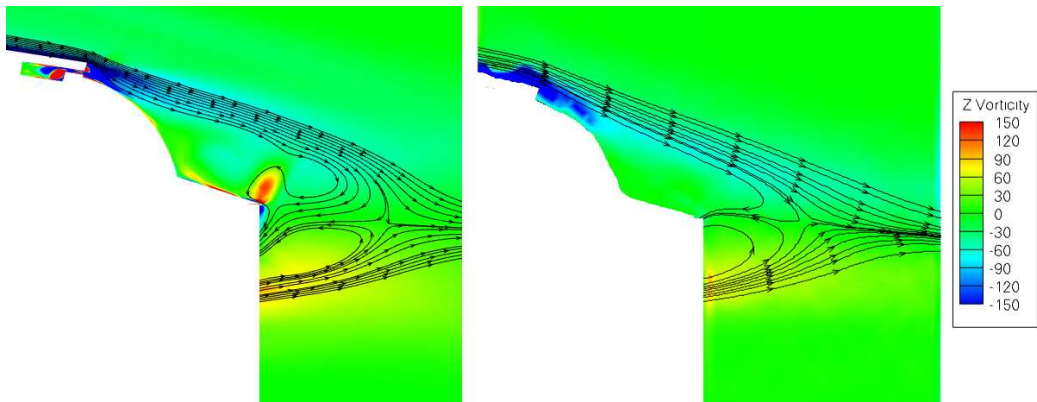
Figure 4.14: Time averaged vorticity field including streamlines for the suction side actuator. Computational (left) and experimental PIV (right)

87
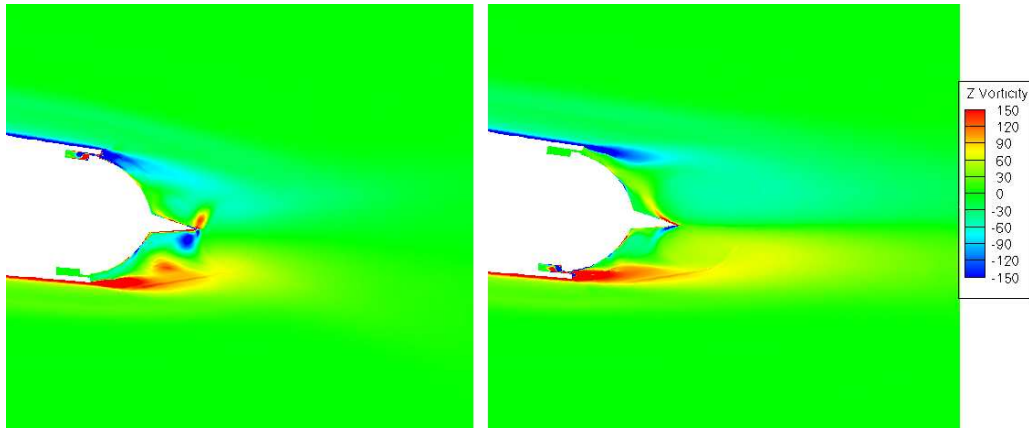
Figure 4.15: Computational time averaged vorticity field in the near wake ($\alpha = 0°$). SS actuation (left) and PS actuation (right)

to the unactuated case consistent with the experimental results[89] (see figure 4.16). For the pressure side actuator the near wake shows an upwash, which has also been observed in previous experimental work[89].

Figure 4.15(right) shows that both recirculation regions are affected by the pressure side actuation in the computational results, they seem thinner and longer than the unactuated case. This observation is not consistent with the experimental results in which the near wake is shorter than the unactuated case (see figure 4.16-right). Experimental observation suggested that this difference could be attributed to a three-dimensionality in the velocity field arising from the jet [9]. A three dimensional version of the detailed model was implemented and tested to explain the discrepancies observed between the experimental and computational vorticity fields for the PS actuation. The spanwise domain size of this test was $L_z = 0.0831c$ which corresponds to the size of one synthetic jet disk and 20 grid points were used in the spanwise direction. The boundary condition given by the normal velocity in the actuator

88
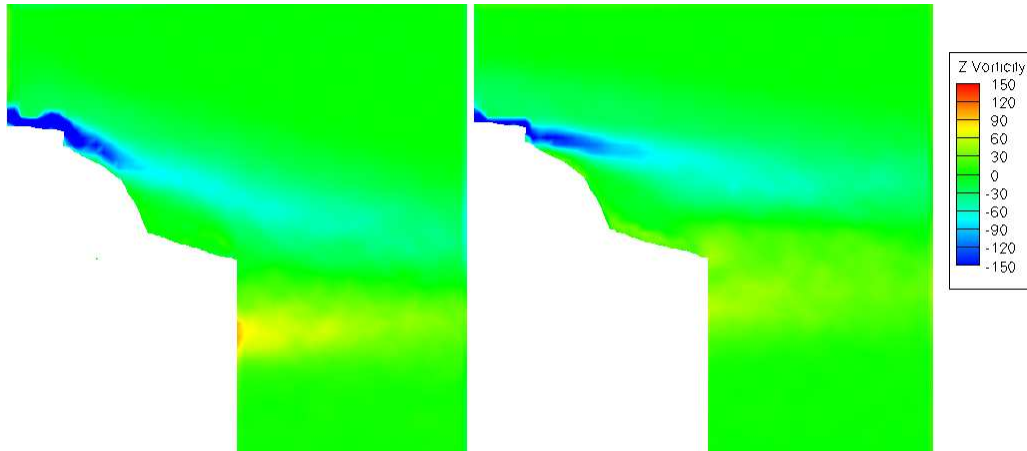
Figure 4.16: Experimental time averaged vorticity field in the near wake ($\alpha = 0°$). SS actuation (left) and PS actuation (right)

chamber now depends on the spanwise direction (z):

$$U_n = A \sin\left(\pi \frac{z}{L_z}\right) \sin\left(2\pi F^+ T\right) \tag{4.11}$$

Where A is set to match the same mass flux of the 2D boundary condition (see equation 3.29). Figure 4.17 shows the time averaged vorticity field at two different spanwise locations for this simulation. It is clear that at $z = 0.04c$ (center of the synthetic jet outlet) the vortical structures and the near wake are shorter than at $z = 0$. A very good agreement is observed between the experimental PIV results (at the same spanwise location - figure 4.18) and the three dimensional simulation, not only in the magnitude and size of the vortical structures but also on the computed streamlines based on a 2D velocity field. Though the three-dimensionality of the velocity field explains such differences, using this model makes the CFD extremely expensive. For a simulation with a domain of one chord-length in the Z direction, it requires about 250 grid point in the spanwise direction and a reduction of the filter
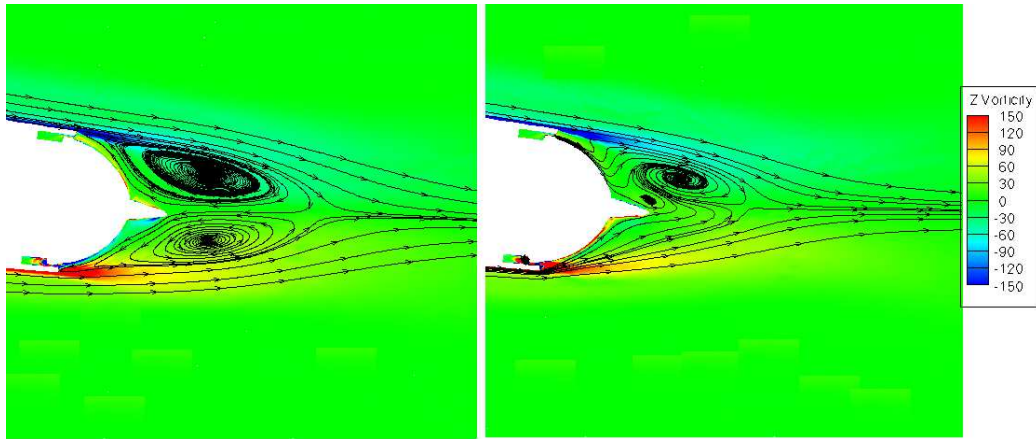
Figure 4.17: Time averaged vorticity field with streamlines for 3D detailed model. $z = 0$ (left) and $z = 0.04$ (right)

size in the LES region of 10 times, increasing the number of control volumes to the order of 100 millions. For this reason this three dimensional synthetic jet model was not pursued any further.

The effect of the actuators in the wake is more dramatic in the instantaneous vorticity fields. Figure 4.19 shows the instantaneous vorticity field of the wake for the SS actuated (left) and PS actuated (right) $15T$ after the actuation was iniciated. For the suction side actuation, the Strouhal number increases to 5.1 as was corroborated through a Fourier analysis (see figure 4.44). More details about this S_t increment are given in section 4.3.4.2. It is also clear that the wake for the suction side actuation is thinner in comparison to the unactuated case. On the other hand the pressure side actuation produces a different effect on the wake, it reduces the vortex shedding substantially, and a stabilization of the wake is observed after 8 convective time units (T). Attenuation of vortex shedding with high frequency actuation has also been

90
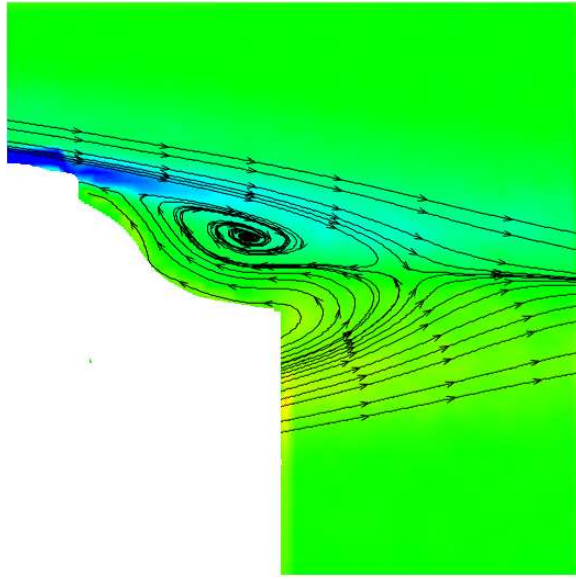
Figure 4.18: Experimental time averaged vorticity field with streamlines for the PS actuation.

observed in other experimental studies in which it was found that the high frequency actuation increases the dissipation and reduces the turbulent kinetic energy in the wake[49][130].

Figures 4.20 and 4.21 show the averaged turbulent kinetic energy in the near wake for the unactuated case and the pressure side actuation case respectively. For the unactuated case, the computational results fluctuating energy is about a factor of 1.5 larger than the experimental measurements. The stabilization of the wake due to pressure-side actuation observed in the instantaneous vorticity field is corroborated in the averaged computational turbulent kinetic energy field (Figure 4.21 left). This reduction of the turbulent kinetic energy has also been observed in the experimental setup at Georgia Tech, but not as strongly as is predicted by the simulations.

91
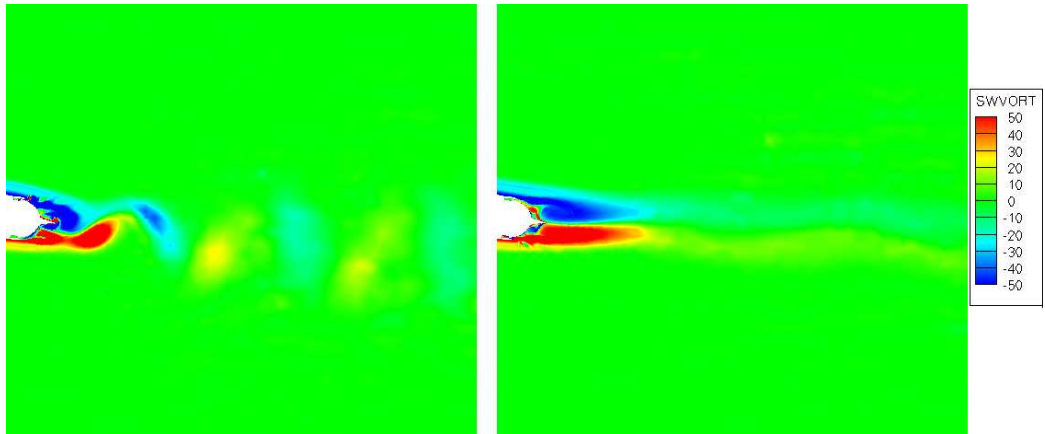
Figure 4.19: Instantaneous vorticity field in the wake ($\alpha = 0°$). SS actuation (left) and PS actuation (right)
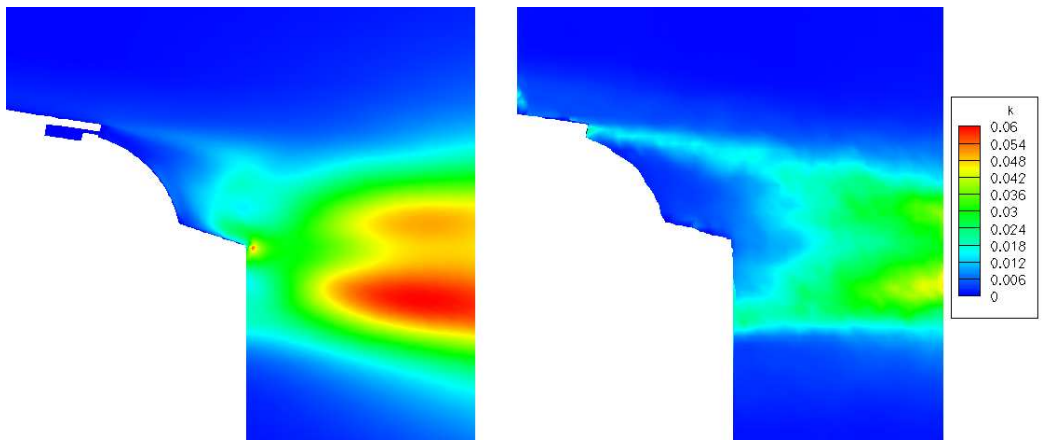
Figure 4.20: Averaged turbulent kinetic energy field unactuated case ($\alpha = 0°$). Computational (left) and experimental (right)
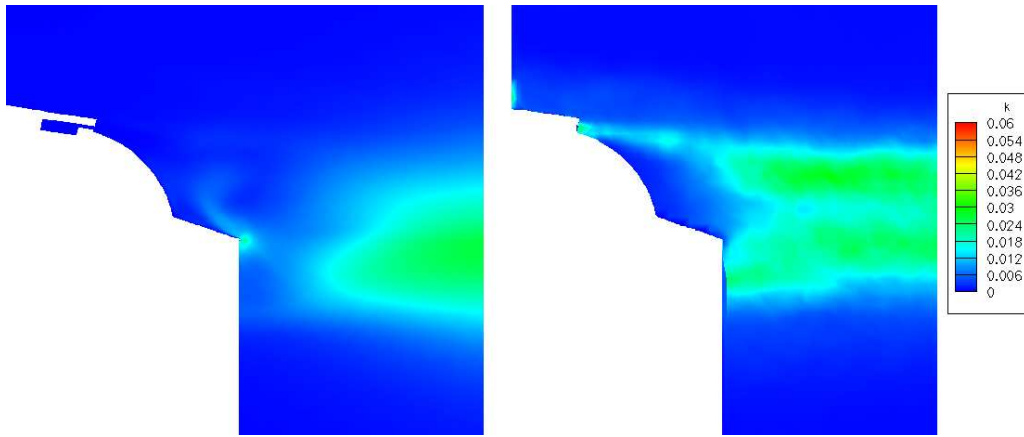
Figure 4.21: Averaged turbulent kinetic energy field pressure side actuation case ($\alpha = 0°$). Computational (left) and experimental (right)

This stabilization of the wake is not observed at other angles of attack or lower jet strengths, so several computational experiments were run changing other parameters such as: frequency of actuation and trailing edge rounding, at full actuation. It was found that the stabilization of the wake was still observed at other frequencies of actuation (in the vicinity of F^+) so a phase locking effect was ruled out. On the other hand, it was observed that the stabilization of the wake was broken if the trailing edge was rounded (at $F^+ = 31.24$). Despite that there was not available data of the exact rounding of the trailing edge of the wind tunnel model, the computational model was rounded with a radius of $\approx 0.001c$. Figure 4.22 shows the effects of the rounding in the instantaneous and time averaged vorticity for the PS actuation. It is clear that the time averaged vorticity shows a shorter near wake and that the instantaneous vorticity field shows a vortex street. The effect of such an small rounding of the trailing edge is significant in the flow field but it is negligible in the aerodynamic properties as is shown in section 4.3.4.2.

93
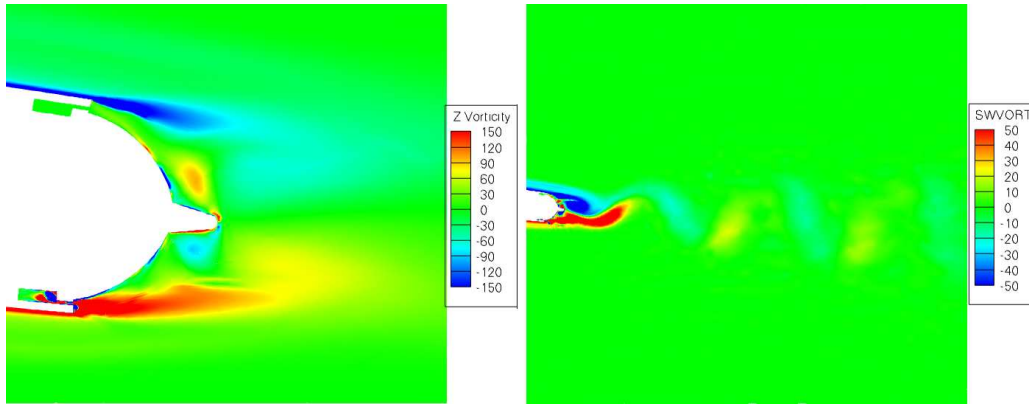
Figure 4.22: Vorticity field for the rounded trailing edge case (PS actuation and $\alpha = 0°$). Time averaged near wake (left) and Instantaneous wake (right)

Figure 4.23 shows the evolution of the vorticity and velocity vector field in one actuation cycle at full actuation. The cycle starts with the inflow phase (Figure 4.23a). In this stage the fluid is sucked into the actuator cavity, as this is happening a clockwise vortex (blue) is formed over the synthetic jet outlet. The size and strength of the vortex increases as the inflow finishes as is shown in Figure 4.23b. The outflow phase starts in Figure 4.23c, at this moment the fluid that is blown out of the cavity interacts with the clockwise vortex and detaches it. As the outflow continues a counterclockwise vortex (Figure 4.23d), which is smaller and weaker than the clockwise vortex of the inflow phase, is created at the synthetic jet outlet. Figure 4.23e shows the end of the outflow phase, were the counterclockwise vortex detaches from the actuator due to the cross flow. Both vortices interact with the wall vorticity and with the shear layer as they are convected downstream. Figure 4.23f shows the beginning of the inflow stage, in which the clockwise vortex starts. Finally, the cycle is completed as it is shown in Figure 4.23g.

94
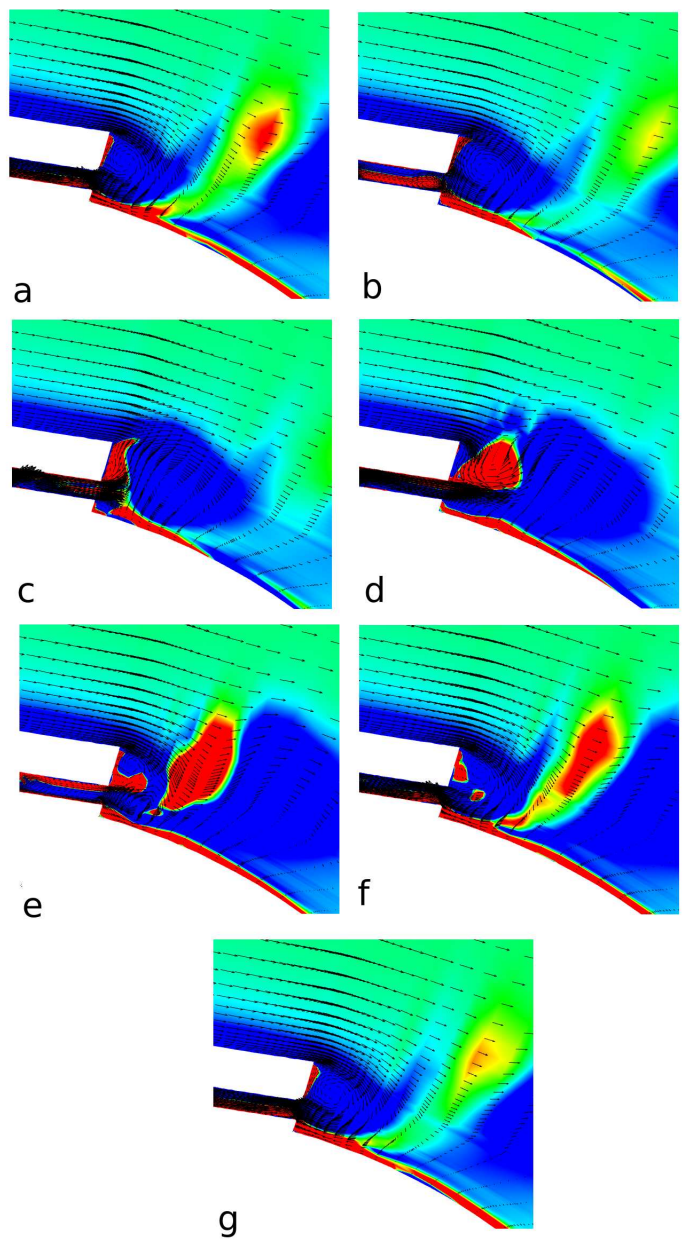
Figure 4.23: Evolution of the vorticity and vector field close to the synthetic jet outlet

This dynamic of the vorticity field at the synthetic jet outlet depends on a formation criteria given by the inverse of the strouhal number based on the slot height (F_h^+) [59]

$$\frac{1}{F_h^+} = \frac{\tilde{U}}{\Omega h} \tag{4.12}$$

Where h is the height of the synthetic jet outlet, Ω is the actuation frequency and $\tilde{U}$ is the time and spatial averaged synthetic jet exit velocity given by

$$\tilde{U} = \frac{2}{Th} \int_0^h \int_0^{T/2} u(t,h)dtdh \tag{4.13}$$

Mittal et al [59] proposed that when this quality is greater than about 1, a synthetic jet is formed [2] [59]. For full actuation the inverse of the strouhal number is 3.86 so as is shown in figure 4.23 a jet is formed. If the jet strength is not high enough to reach the formation criteria then the pair of vortices is ingested back into the slot during the inflow phase and no jet is formed. Figure 4.24 shows the evolution of the vorticity field in one actuation cycle at a quarter of full actuation. The cycle starts with the outflow (Figure 4.24a) in which the fluid is blown out of the actuator's cavity and a pair of co-rotating vortices are formed at the synthetic jet outlet. The size and strength of the vortices increase as the outflow phase continues (see figures 4.24b and 4.24c) but not as strong as in the full actuation case. The outflow finishes in Figure 4.24c, but the vortices are not detached and they stay at the synthetic jet outlet. The inflow starts in Figure 4.24d in which the pair of co-rotating vortices start being sucked into the synthetic jet outlet. As the inflow continues (Figures 4.24e and 4.24f), the vortices

---

[2] Jet formation as "the appearance of a time-averaged outward velocity along the jet axis and corresponds to the generation and subsequent convection or escape of a vortex ring"[59]

are slowly ingested into the synthetic jet as their size and strength decreases. Finally, the cycle is completed as is shown in Figure 4.24g in which the pair of co-rotating vortices were ingested back into the slot. For this case, the inverse of the strouhal number was about 0.98 so the evolution shown in figure 4.24 is consistent with the theory of jet formation and it is expected that the performance of the synthetic jet will be seriously affected for this operating condition.

4.3.3.2 Effects on the the aerodynamic properties

The effects of the actuation on the aerodynamic properties are mainly focused on the lift, moment and pressure coefficients for two reasons: first C_l and C_m are the most relevant properties to airfoil dynamics; and second, it is expected that the impact of the synthetic jet actuation on the drag coefficient is negligible. The evolution of the aerodynamic properties in time before and after actuation is the first way in which the effects of the actuation will be explored. Figure 4.25 shows the evolution of the moment coefficient (C_m) measured at $0.25c$ for an angle of attack of $0°$ in which the actuator is active after 7.5 convective time units. When the suction side actuator is active, there is an increase in the pitch down moment, on the other hand there is a pitch up when the pressure side actuator is active.

Figure 4.26 shows the effects of the actuator on the lift coefficient (C_l) for the same simulation, when the suction side actuator is active there is a reduction of the lift coefficient, while there is an increase when the pressure side actuator is active. For this simulation ($Re = 9 \times 10^5$ and $\alpha = 0°$) the increase in the C_m due to the suction side actuator is about 0.015 while the reduction in C_l is about 0.07 (i.e

97
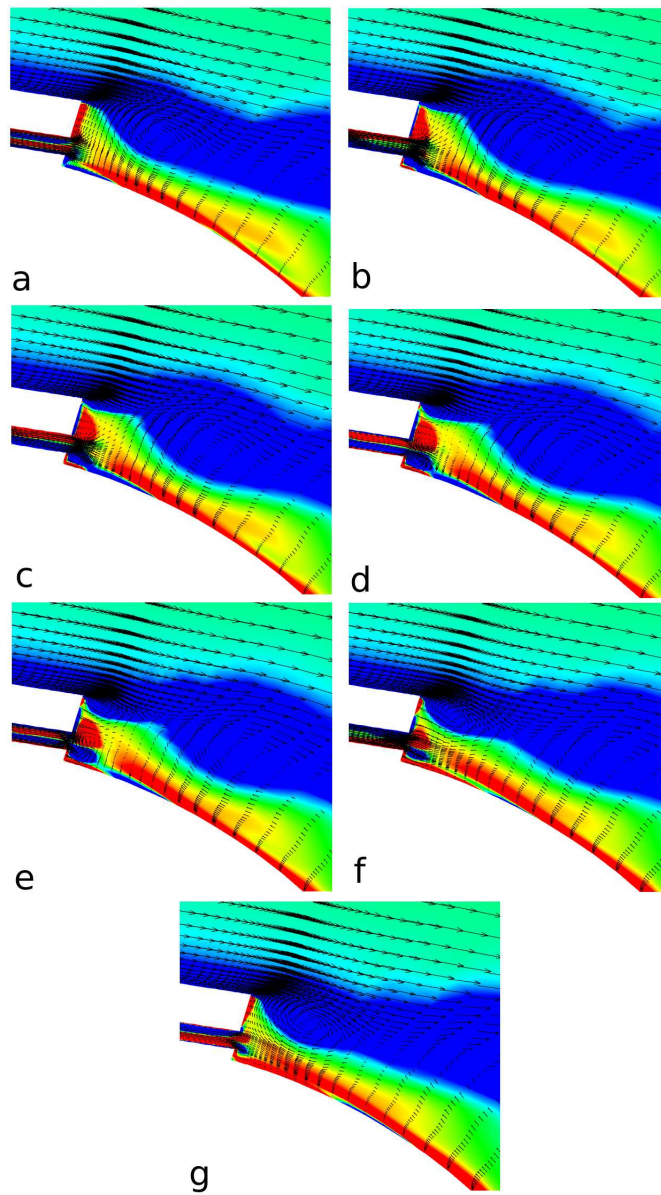
Figure 4.24: Evolution of the vorticity and vector field close to the synthetic jet outlet for quarter of full actuation
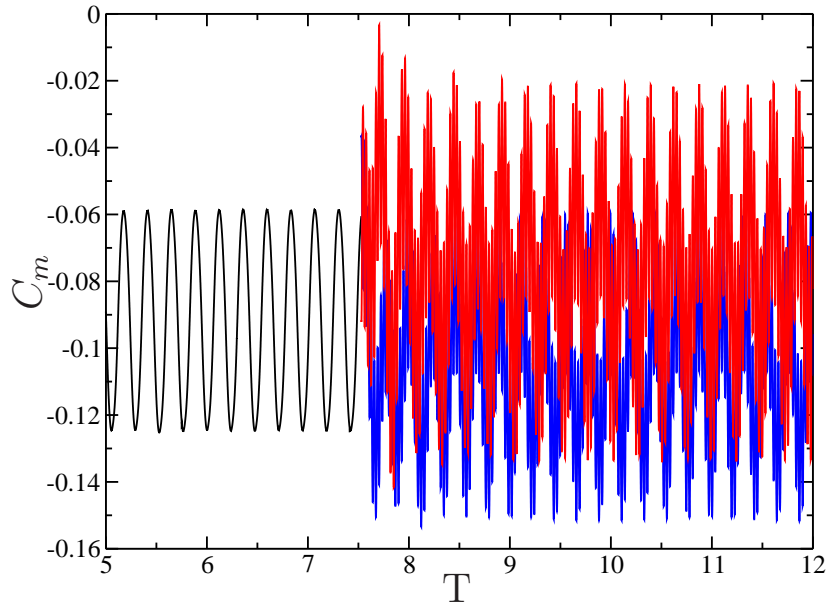
Figure 4.25: Moment coefficient as a function of T. (No act − SS − PS −)

$\Delta C_l \approx 5\Delta C_m$), similar results were reported in the experimental measurements at Georgia Tech.

The effect of the actuation on the drag coefficient at an angle of attack of 0° is shown in figure 4.27. The change in the drag is negligible since the average C_d value before actuation is ≈ 0.016 while for the suction and pressure side actuation it is ≈ 0.0157 and ≈ 0.0152 respectively. Another important observation is the change in the dominant frequencies in the evolution of the aerodynamics properties, before and after the actuation. Before actuation, the shedding frequency is dominant, but with actuation, it is the actuation frequency that is dominant.

Figure 4.28 shows the variation of the time-averaged pressure coefficient (C_p) along the airfoil due to full actuation at an angle of attack of 0°. Actuation influences
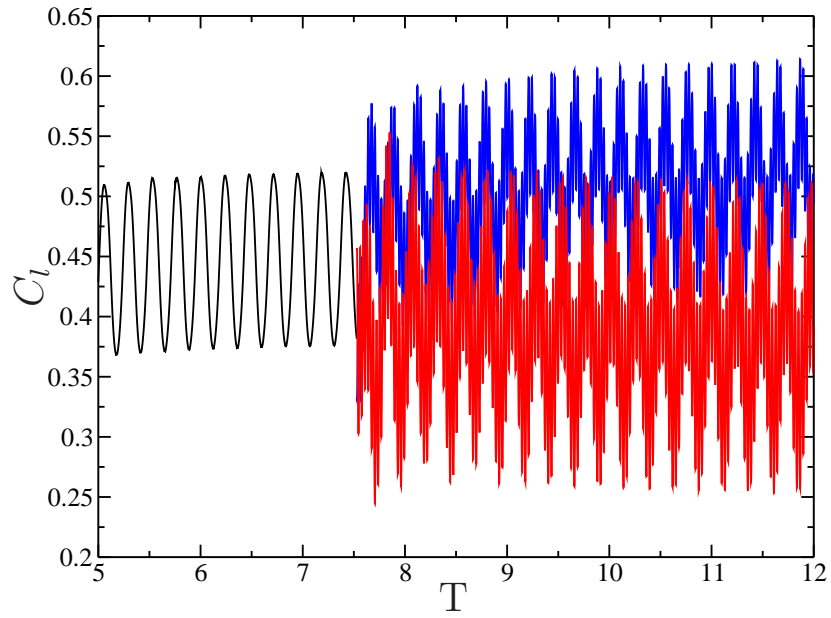
Figure 4.26: Lift coefficient as a function of T. (No act − SS − PS −)
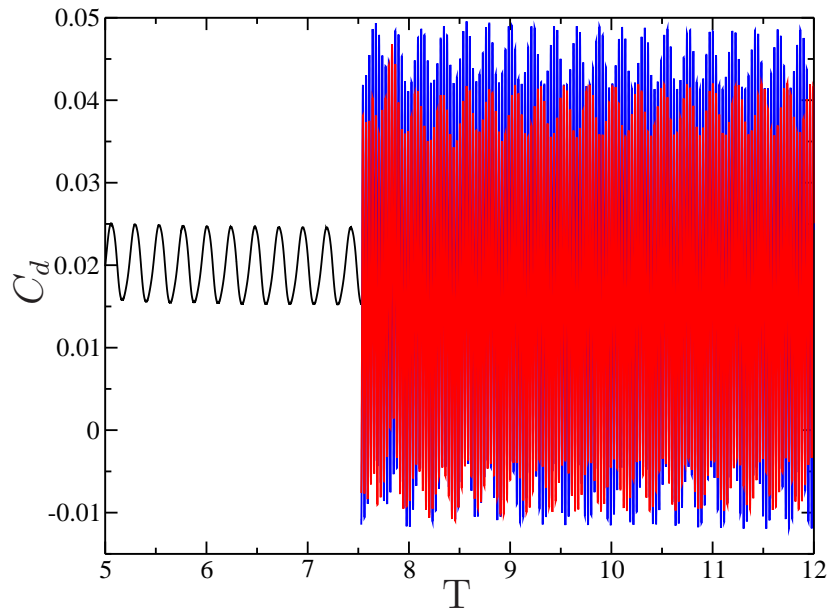
Figure 4.27: Drag coefficient as a function of T. (No act − SS − PS −)

100
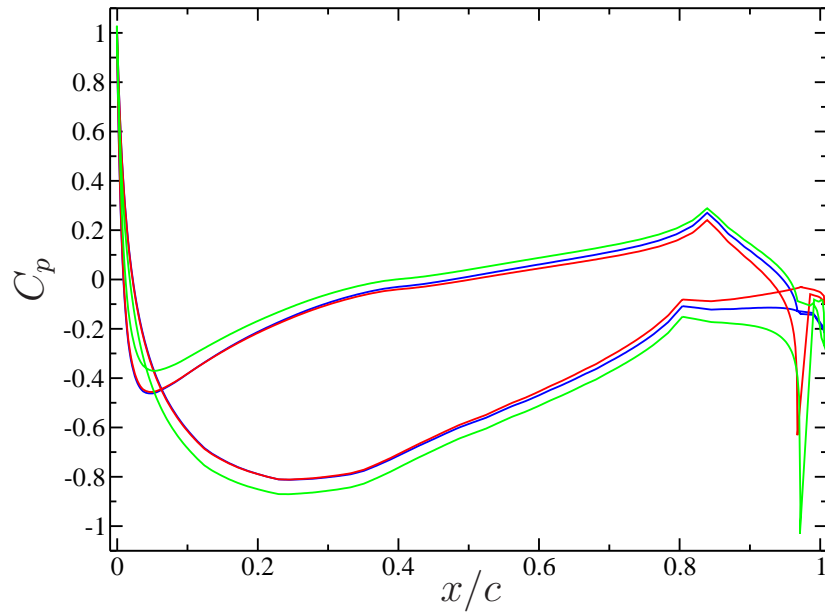
Figure 4.28: Pressure coefficient at $\alpha = 0°$. (SS — PS — no act —)

the pressure distribution, especially at the trailing edge where a spike in the pressure is induced by the actuation. The increment of C_p at full actuation, for both the suction and pressure side actuators, at $\frac{x}{c} = 0.95$ (position of the actuators) is about 0.9 relative to the unactuated case. Similar results were reported by DeSalvo et al [37] with the same actuators but on a different airfoil. This local reduction of the pressure is associated with the trapped vorticity and with a flow acceleration close to the trailing edge.

Figure 4.29 shows the effect of the suction side jet strength on the time-averaged pressure coefficient at an angle of attack of 0°. On the left, is shown that as the level of actuation decreases the area inside the C_P curve (hence C_l) decreases. Figure 4.29 (right) shows the C_p spike near the trailing edge caused by the actua-
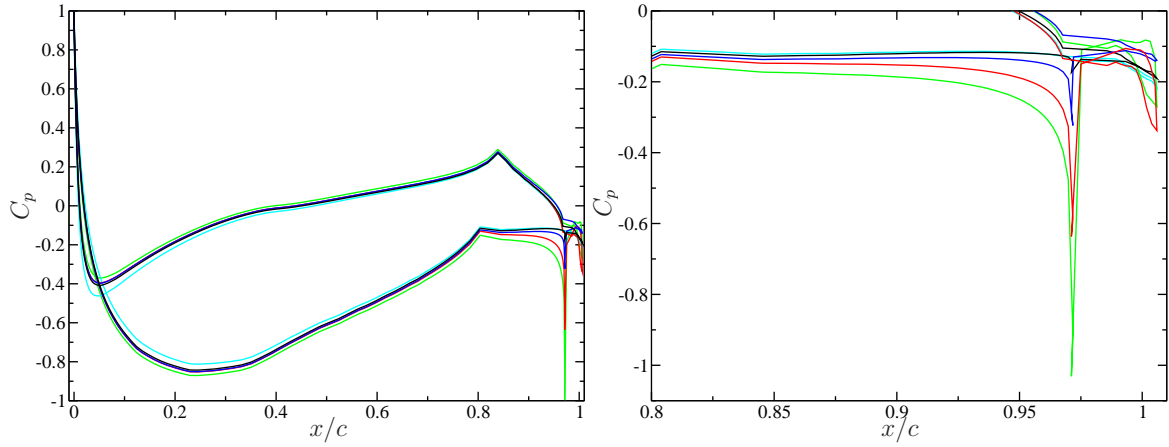
Figure 4.29: Pressure coefficient at $\alpha = 0°$ for different levels of SS actuation. (Full — Three quarter— half— quarter — noact —)

Actuation	ΔC_p
0.25	0.05
0.5	0.21
0.75	0.6
1.0	0.99

Table 4.1: ΔC_p at $\frac{x}{c} \approx 0.97$ (synthetic jet outlet location) for different levels of actuation

tion. When the jet strength is approximately a quarter of the full actuation, the lift enhancement is greatly reduced, as was predicted by the jet formation criteria which can be quantified by the increment on the local pressure at the synthetic jet outlet (see table 4.1).

The effectiveness of the actuator is measured by computing the increase or decrease of the the aerodynamic properties of the airfoil, in particular the change in moment and lift coefficients (ΔC_m and ΔC_l respectively). In early computational experiments, the performance of the pressure and suction side actuators was presumed

to be identical; That is $A = 0.38U_\infty$ (see equation 3.29) was the same for both actuators, set to match the experimental determined $C_\mu = O(10^{-3})$. But comparison with experimental data over a range of α showed and inconsistency which was not possible to eliminate under the assumption of identical actuators. A number of possible causes for this discrepancy were eliminated, including three dimensionality of the actuation and PS boundary layer grid resolution. To address this discrepancy, the amplitudes of the boundary condition forcing for the two actuators were adjusted independently to match experimental ΔC_m at $\alpha = 0°$, with the result of $A = 0.41U_\infty$ and $A = 0.36U_\infty$ for the SS and PS actuators respectively. However, there was still a discrepancy in the PS ΔC_m response, with the sensitivity of ΔC_m to α too large in the computations, as is evident in figure 4.30. It was found that this discrepancy could be addressed by making a small geometric adjustment in the PS actuator as shown in figure 4.31.

Figures 4.32 and 4.33 show the effectiveness of the actuator (computational and experimental), with the modifications mentioned before, in the range of $-2°$ to $6°$ at full actuation. It is shown that the boundary condition and geometric modifications help to capture the correct trend in the ΔC_m and ΔC_l slopes. The performance and parametrization of the detailed and RSSJ models could be improved by more precisely matching the experimental data. Since ΔC_m is a small quantity of $O(10^{-4})$, it is very sensitive to the precision in the boundary condition parameter A. Here, it was considered that the precision given to A was acceptable to demonstrate the capabilities of the detailed model.
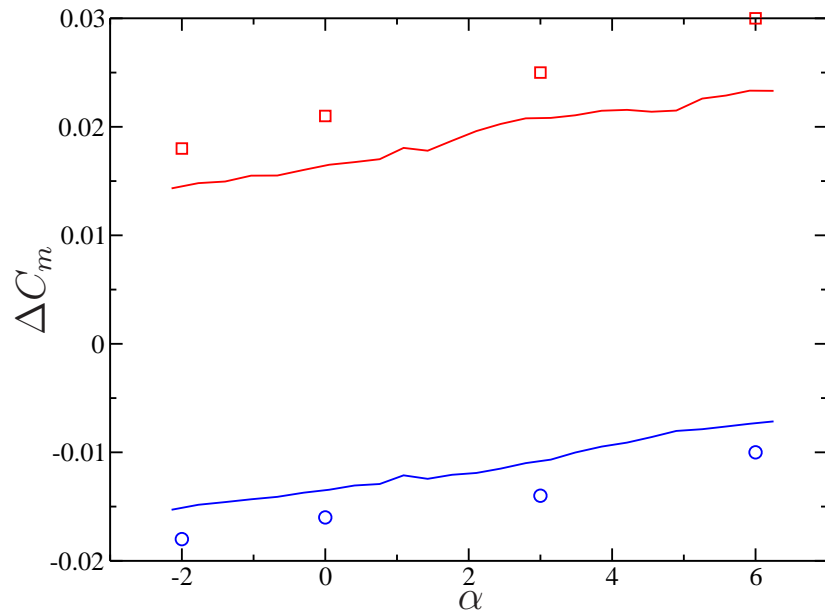
Figure 4.30: ΔC_m as a function of α (early results). (SS exp — PS exp— SS comp ○ PS comp □)
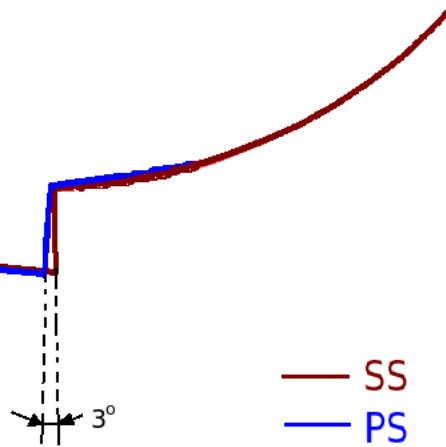
Figure 4.31: Geometrical modification in the PS actuator

104
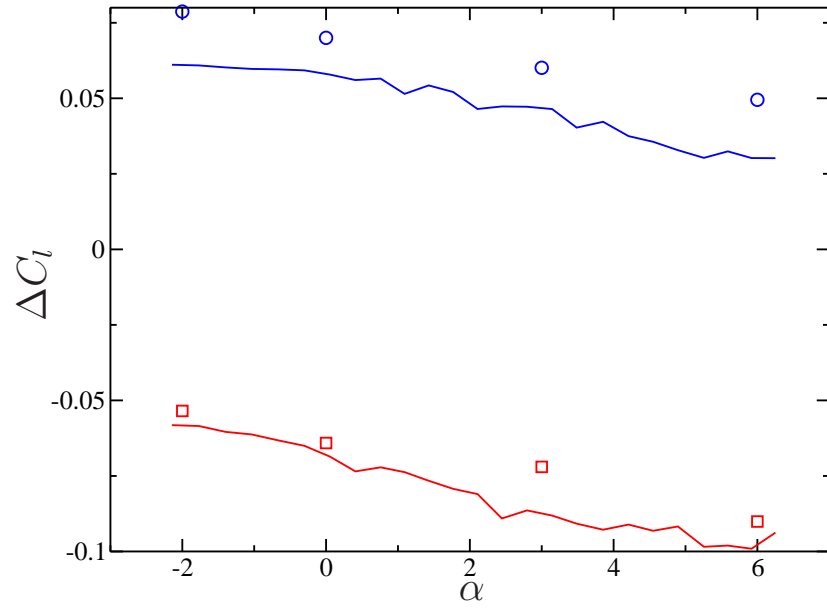
Figure 4.32: ΔC_l as a function of α. (SS exp — PS exp— SS comp ○ PS comp ☐)

Figure 4.33: ΔC_m as a function of α. (SS exp — PS exp— SS comp ○ PS comp ☐)

105
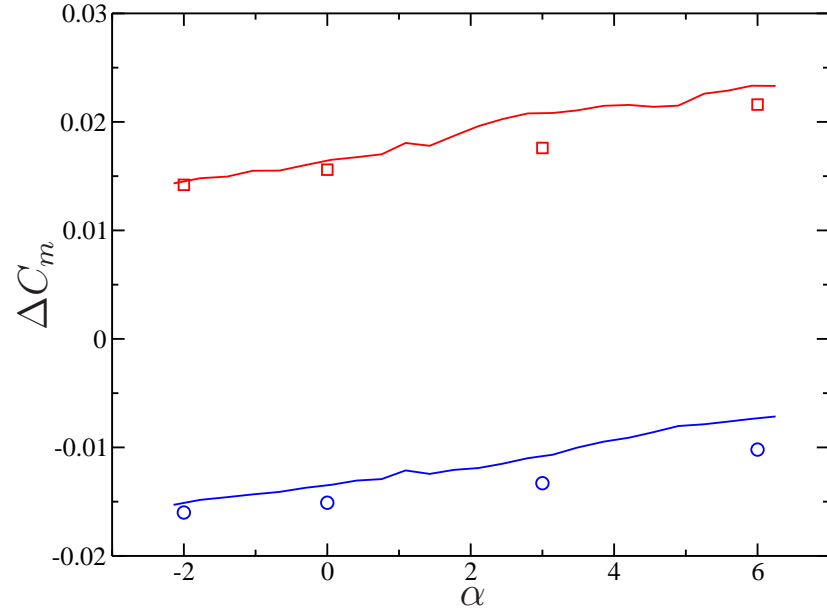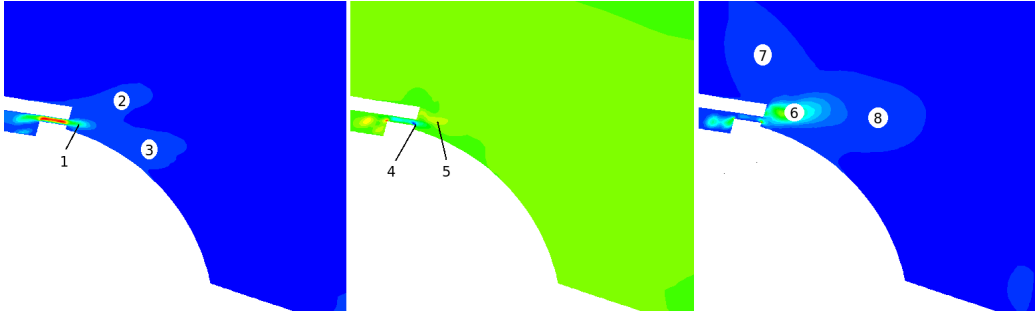
Figure 4.34: Reynolds Stress field arising from the suction side synthetic jet. $\overline{u'u'}$ (left) $\overline{u'v'}$ (center) $\overline{v'v'}$ (right).

4.3.4 Modified Actuated - RSSJ model

As pointed out in section 3.5.2, numerical results from the detailed model can be used to develop a less computationally expensive synthetic jet model for dynamic simulations. As it was discussed in chapter 3, this ad hoc model involves parameterizing the two dimensional time and spanwise averaged Reynolds stress field (RSF) that arises from the synthetic jet. Figure 4.34 shows the three components of the RSF (for the suction side actuator at $\alpha = 0°$) that arise from the jet, which are obtained by computing the difference between the actuated and unactuated averaged fields. To fully describe the Reynolds stress tensor, it is necessary to represent at least eight concentrations (sources or blobs). As explained in section 3.5.2 (see equation 3.30) each source requires six different numerical parameters (Γ_i, θ_i, λ_i, ω_i, X_i and Y_i) meaning that a complete description of the RSF needs almost fifty numerical parameters per actuator, and in general each parameter would be a function of α and the jet strength for static airfoils.

A model with 50 numerical parameters to independently characterize as a

function of α and the jet strength is challenging, so for practical reasons the model was here simplified by reducing the number of spots and by dependency reduction. The dependency reduction is simply based on observation of the Reynolds stress field behavior (obtained from detailed simulations) at three different angles of attack ($-6°$,$0°$ and $6°$) and four different levels of actuation (full, three quarter, half and quarter). For example: Figure 4.35 and 4.36 show the variation of the $\overline{u'u'}$ component of the actuator induced Reynolds stress with the angle of attack and jet strength respectively. For this component of the Reynolds stress, the angle of attack strongly affects θ_i and in a weaker way Γ_i, λ_i and ω_i, while the jet strength directly affects only Γ_i. Similar behavior was observed for the $\overline{v'v'}$ component of the Reynolds stress, while the $\overline{u'v'}$ component is strongly affected by the jet strength but is unaffected by changes in the angle of attack. The spots position defined by (X_i, Y_i) does not strongly change with the jet strength or the angle of attack for any component of the Reynolds stress field.

Based on these observations, dependency reduction allows the number of dependent parameters to be decreased from almost fifty to eleven parameters per actuator. These eleven parameters are: the strength of all eight spots (see figure 4.34),the angle of spot 1 and the size controlling parameters (λ_i and ω_i) of spot 6. This model was implemented and tested, showing good results in both the averaged vorticity field and the aerodynamic properties in comparison with the experimental results (see figure 4.37). Using these eleven parameters in the model not only captures the basic shedding frequency but also other frequencies due to the interaction of the synthetic jet with the shear layer that develops at the end of the actuator ramp.
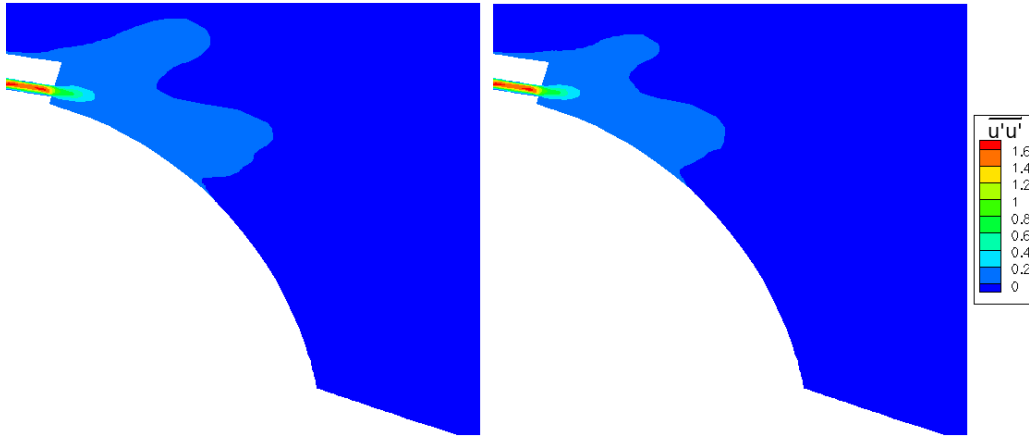
Figure 4.35: Reynolds Stress field arising from the suction side synthetic jet vs α. $\alpha = 0°$ (left) $\alpha = 6°$ (right).
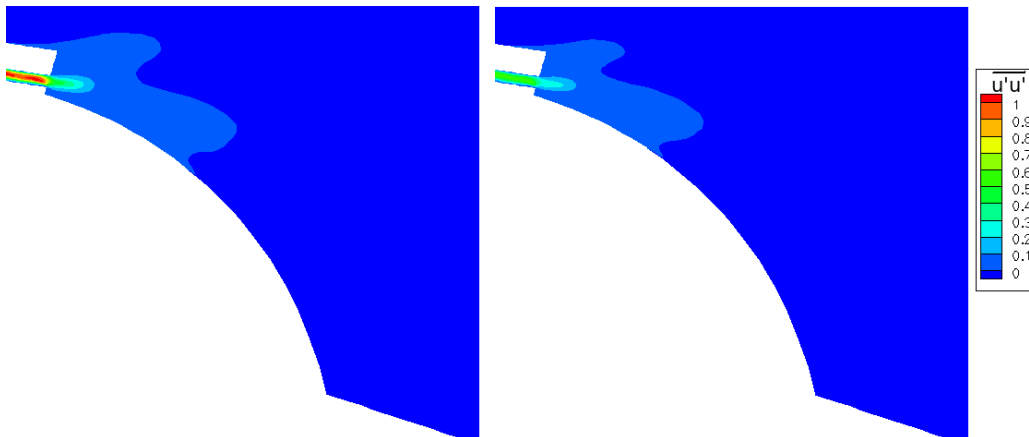
Figure 4.36: Reynolds Stress field arising from the suction side synthetic jet vs jet strength. Full actuation (left) half actuation (right).
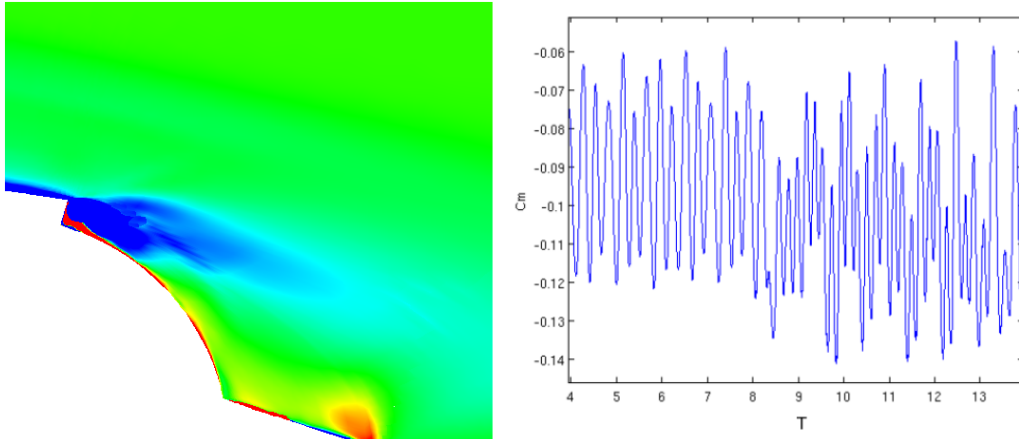
Figure 4.37: Averaged vorticity field (left) and C_m evolution for the RSSJ model (11 parameters).

In order to eliminate the synthetic jet interaction with the shear layer, the weaker spots were also eliminated i.e: Only those concentrations of Reynolds stress that were located closer to the synthetic jet outlet (1, 4, 5 and 6) were retained. It seems that these spots would represent the Reynolds stress field very close to the synthetic jet outlet disregarding the interaction of the synthetic jet with the shear layer formed at the edge of the actuator ramp. Based on this analysis a simplified RSSJ model can be developed with only seven numerical parameters (Γ_1, θ_1, Γ_4, Γ_5, Γ_6, λ_6 and ω_6) that change with the angle of attack and the jet strength. Once the number of parameters used in the RSSJ model are determined, then their numerical values have to be estimated. A First approximation to this estimation is done by eyeballing matching the Reynolds stress field obtained from the detailed model. Then the numerical parameters are slightly adjusted in order to match ΔC_m values from the detailed model. Appendix C shows the magnitude of the seven parameters finally

used in the RSSJ model for the different cases including those parameters that remain unaltered. Though this set of numerical parameters is specifically designed for this application and problem, the methodology followed in this study could be extended to other synthetic jet simulations.

To complete the model, the maps of the dependence of these numerical parameters with respect to the change of pressure (Δp) along the actuator ramp has to be determined. As discussed in section 3.5.2, to use this model in a dynamic simulation the numerical parameters must be controlled by a local flow field variable (Δp) and a radial basis function interpolation. Appendix D shows the values of the weights used in the interpolation process, in which a Gaussian radial basis function was employed due to its extrapolation properties particularly close to zero jet strength [95]. This simplified model was implemented and used here and its results are shown in the following sections.

4.3.4.1 Effects on the vorticity field

As previously discussed, the important quantitative effect of the actuation, is the bending of the shear layer formed at the actuator ramp edge towards the coanda surface. Figures 4.38 and 4.39 show the time average spanwise vorticity for the suction and pressure side actuators respectively, with a comparison of the detailed and RSSJ model.

While there are some differences in the details, the simplified model captures the bending of the shear layer towards the coanda surface and also the distribution of vorticity along the surface including the trapped vorticity close to the trailing edge,
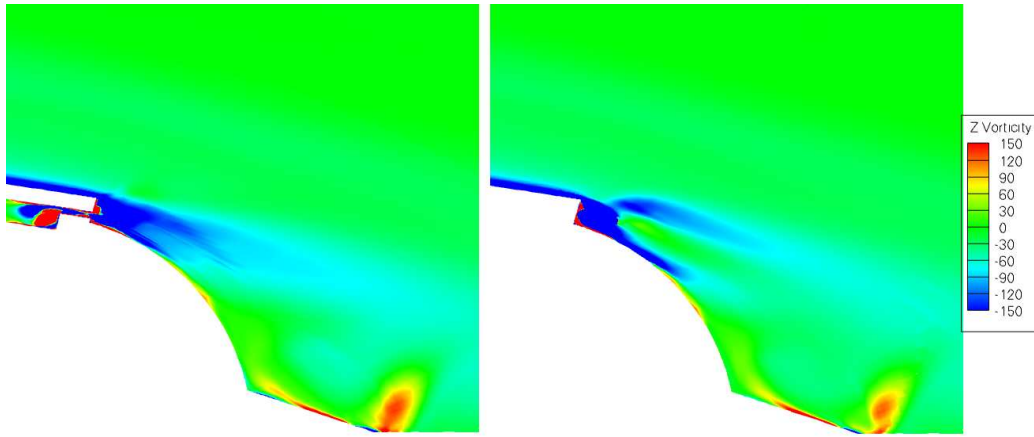
Figure 4.38: Comparison of the time-averaged spanwise vorticity field (SS) at $\alpha = 0°$ between detailed model (left) and RSSJ model (right)

despite the fact that the simplified model just retained the sources that were closer to the synthetic jet outlet. The most remarkable difference is the vorticity far from the coanda surface on the suction side actuator. It is suspected that this difference is due to the lack of sources in this part of the domain, which would interact with the shear layer that is formed at the end of the actuator ramp.

Figure 4.40 shows the time average vorticity field for the suction and pressure side in the near wake, which shows very good agreement with the detailed model (see figure 4.15). As in the detailed model, there is a downwash of the vortical structures for the suction side actuation and a upwash for the pressure side actuation. It is also clear that the recirculation regions seem longer and thinner for the pressure side actuation than the suction side actuation which is also apparent in the detailed model results.

The effect of the model on the instantaneous vorticity field in the wake is

111
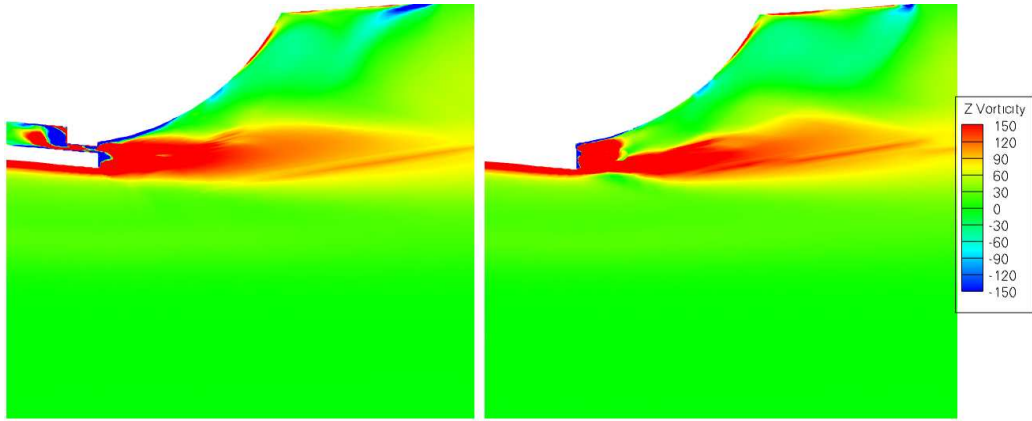
Figure 4.39: Comparison of the time-averaged vorticity field (PS) at $\alpha = 0°$ between detailed model (left) and RSSJ model (right)
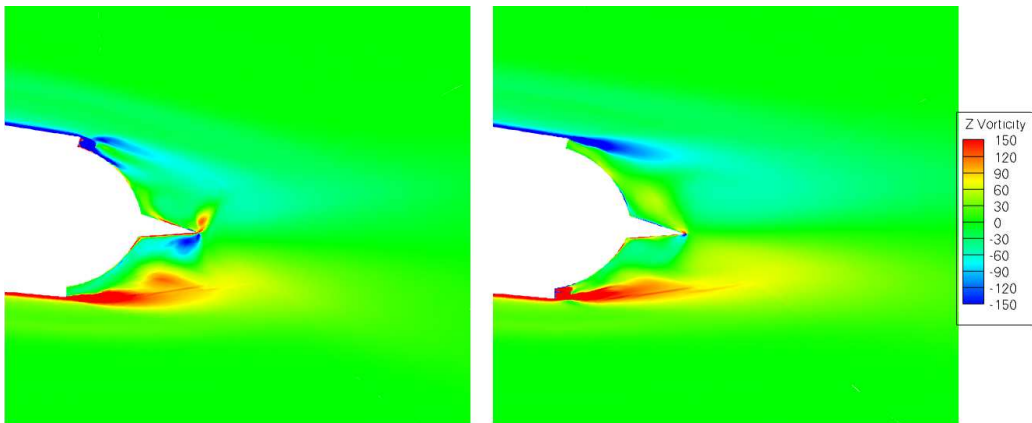
Figure 4.40: Computational time averaged vorticity field in the near wake (RSSJ model) at $\alpha = 0°$. SS (left) and PS(right)
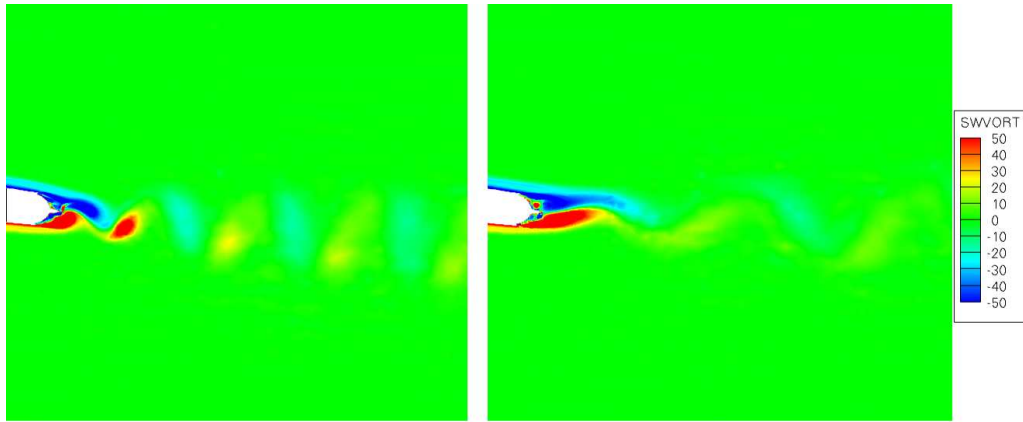
Figure 4.41: Instantaneous vorticity field in the wake at $\alpha = 0°$ (RSSJ model). SS (left) and PS (right)

shown in figure 4.41. The RSSJ model shows good agreement with the detailed model especially for the suction side actuator, for which the vortex shedding frequency with the RSSJ model is consistent with the detailed model. There is an observable difference in the wake for the pressure side actuation. As was pointed out in section 4.3.3.1, the detailed model showed a wake stabilization by pressure side actuation, and this effect it is not completely captured by the RSSJ model. This was expected since the RSSJ model does not represent the dynamic interaction between the jet unsteadiness and vortex shedding. With round trailing edge, for which there is no wake stabilization, the RSSJ model is in good agreement with the detailed model.

4.3.4.2 Effects on the aerodynamic properties

Similar to the detailed model, we are particularly interested in the lift, moment and pressure coefficients. Figures 4.42 and 4.43 show the evolution of C_m and C_l respectively. The conditions for these simulations are the same as the detailed model

113
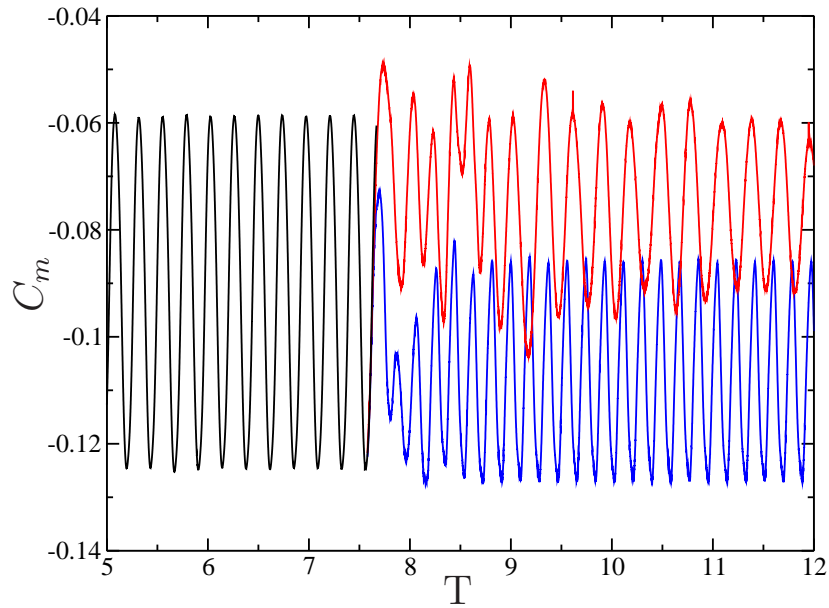
Figure 4.42: Moment coefficient as a function of T for the RSSJ model. (No act −
SS − PS −)

i.e: $Re = 9 \times 10^5$ and $\alpha = 0°$, and the actuation starts at $T = 7.2$. Clearly,
lift enhancement and moment reduction result from suction side actuation while lift
reduction and moment enhancement arise with pressure side actuation. In these plots,
the dominant frequency after actuation corresponds to the shedding frequency, not
the actuation frequency, as was the case in the detailed model (see figures 4.25 and
4.26). The fact that the dominant frequency for the RSSJ model is the shedding
frequency, it allows the model to be advanced in time faster than the detailed model.
Though the magnitude of C_m and C_l fluctuations are significantly smaller in the RSSJ
model, the average values of the aerodynamic properties are consistent between RSSJ
and detailed models.

A Fourier analysis of the moment coefficient evolution (in both models) was

114
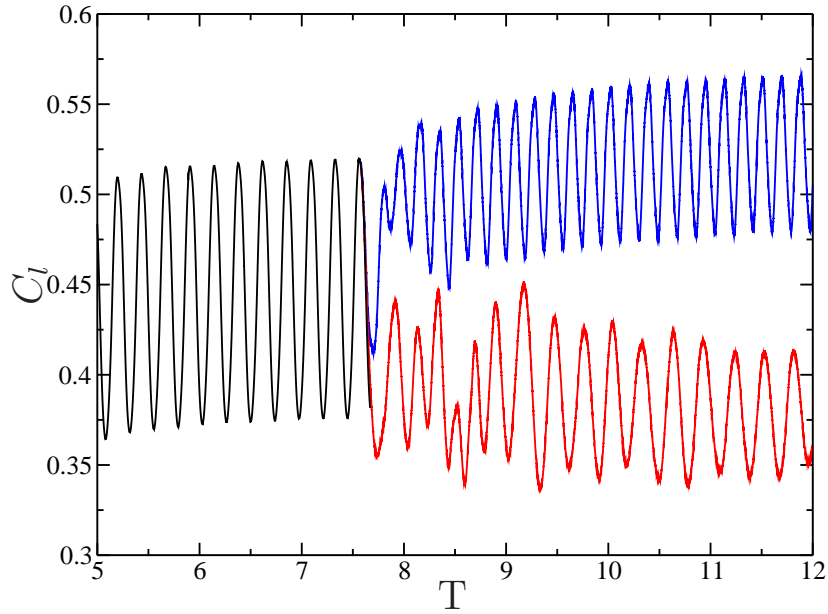
Figure 4.43: Lift coefficient as a function of T for the RSSJ model. (No act − SS −
PS −)

performed further analyze the differences between the models. Figure 4.44 shows the
frequency spectrum of the suction side moment coefficient evolution for both synthetic
jet models.

For the detailed model two primary peaks are observed in the frequency spec-
trum: at $F = 31.2\frac{U_\infty}{c}$ and at $F = 5.1\frac{U_\infty}{c}$. The first occurs at the actuation frequency
F^+ while the other is at the shedding frequency S_t. In fact S_t is shifted to higher
frequency compared to that for the unactuated case of 4.0 (see figure 4.8). The RSSJ
model eliminates the actuation frequency while retaining the shedding frequency and
amplitude, which is corroborated by the comparison between the evolution of C_m for
the RSSJ and the low-pass filtered evolution of C_m for the detailed model (see figure
4.45).

115
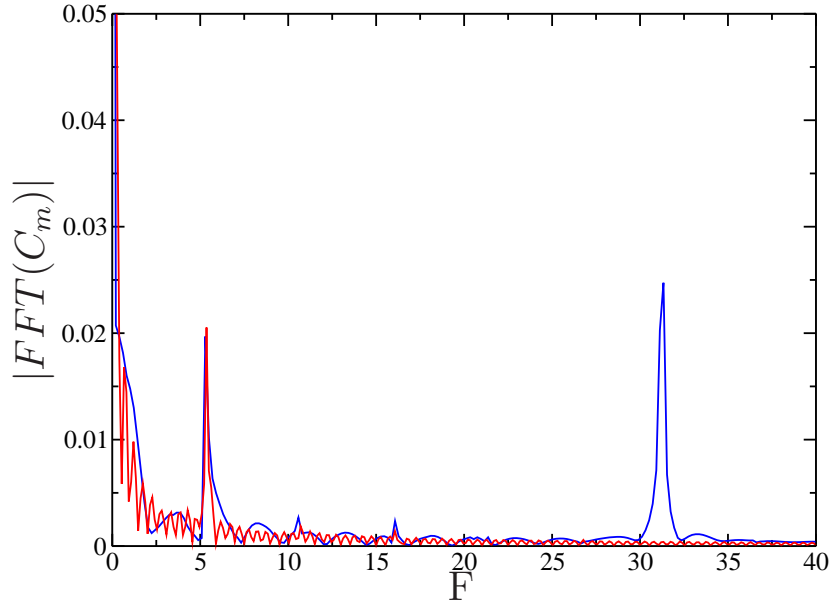
Figure 4.44: Fast Fourier transform of the evolution of C_m for the SS actuation. (Detailed model − RSSJ model −)

A similar analysis was performed on the pressure side actuation (see figure 4.46). As in the SS case the RSSJ model retains the shedding frequency ($S_t \approx 3.7$) while the actuation frequency ($F^+ \approx 31.2$) is eliminated. In this case, the shedding frequency is shifted to lower frequencies compared to the unactuated case . Finally, the amplitude of the shedding frequency is not as well captured as it was in the SS case, as it was pointed out previously the attenuation of the shedding frequency in the detailed model is stronger than the attenuation in the RSSJ model.

Since the stabilization of the wake was suppressed by rounding the trailing edge, a Fourier analysis of simulations results with rounded trailing edge was performed for both synthetic jet models. Figure 4.47 shows the frequency spectrum for the evolution of the moment coefficient for several cases. With rounded trailing edge
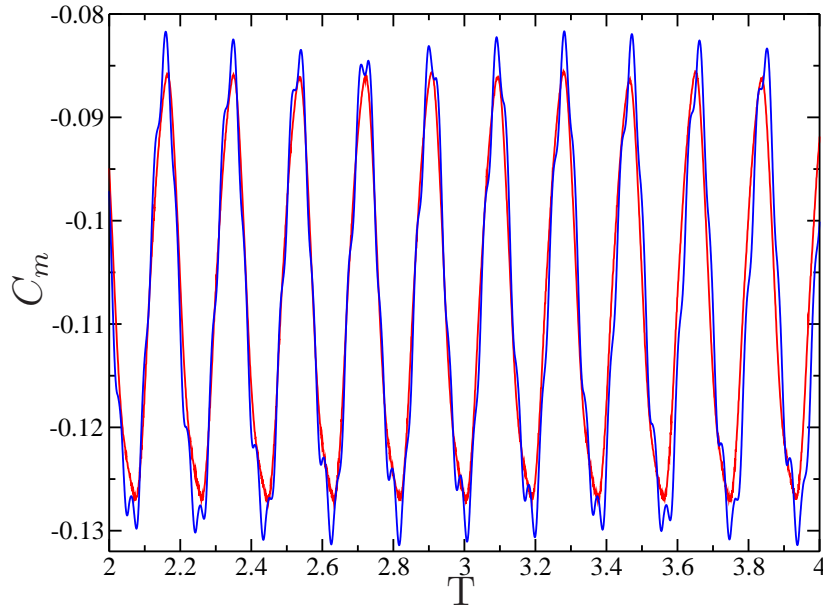
Figure 4.45: Evolution of C_m for the SS actuation. (Filtered detailed model — RSSJ model −−)

the shedding frequency in all cases occurs at $F \approx 4.3$. This result corroborates the effect of the trailing edge geometry on the stabilization of the wake and the magnitude of the shedding frequency relative to the unactuated case. The effect of this small trailing edge rounding on the mean aerodynamic properties is otherwise negligible as shown in table 4.2.

Figure 4.48 shows the time-averaged pressure coefficient along the airfoil at $\alpha = 0°$ and full actuation for both the detail and RSSJ models. Good agreement is found between the two models, despite the fact that the C_p spike is a little bit over predicted by the RSSJ model in both SS and PS actuation. It is also observed that the RSSJ model reproduces very well the pressure distribution along the synthetic jet actuator ramp which plays an important role in the performance of the RSSJ

117
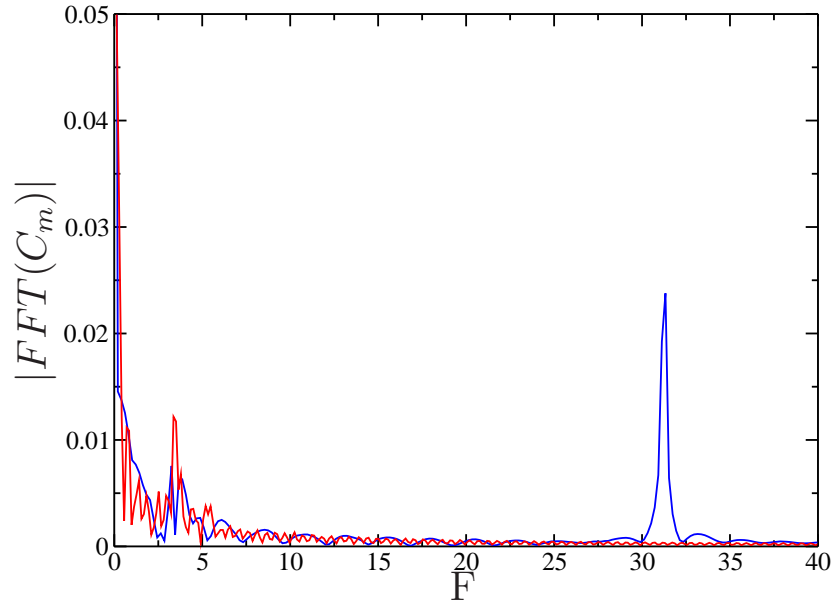
Figure 4.46: Fourier transform of the evolution of C_m for the PS actuation. (Detailed model − RSSJ model −)
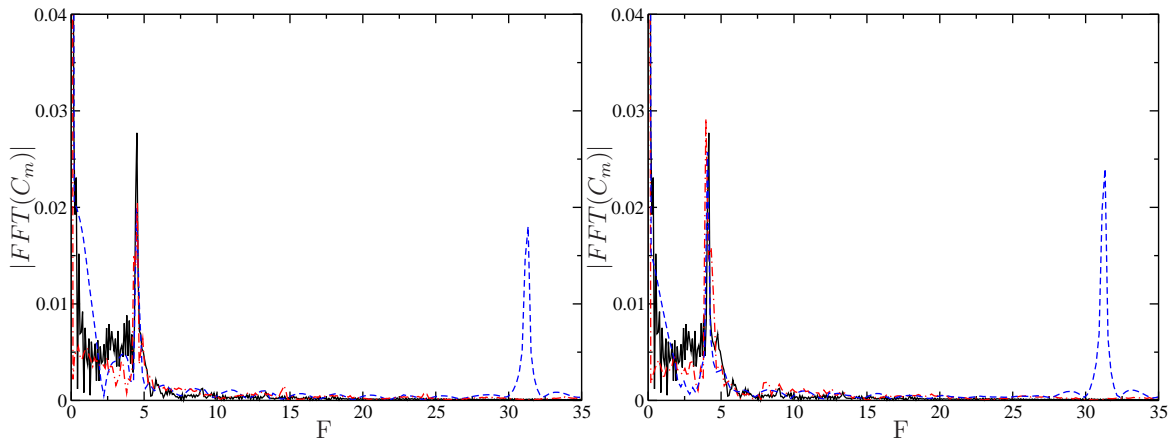
Figure 4.47: Fourier transform of the evolution of C_m for both SS actuation (left) and PS actuation (right) with rounded trailing edge. (no actuation − Detailed model −− RSSJ model −.)

C_m Detailed model

	Sharp			Rounded		
α	no act	SS	PS	no act	SS	PS
0°	-0.0910	-0.1066	-0.0759	-0.0905	-0.1065	-0.0761
6°	-0.0870	-0.0972	-0.0654	-0.0868	-0.0974	-0.0652

C_m RSSJ model

	Sharp			Rounded		
α	no act	SS	PS	no act	SS	PS
0°	-0.0908	-0.1075	-0.0767	-0.0901	-0.1068	-0.0750
6°	-0.0869	-0.0973	-0.0660	-0.0871	-0.0975	-0.06710

C_l Detailed model

	Sharp			Rounded		
α	no act	SS	PS	no act	SS	PS
0°	0.4471	0.5171	0.3830	0.4473	0.5172	0.3829
6°	1.1444	1.1939	1.0543	1.1445	1.2001	1.0543

C_l RSSJ model

	Sharp			Rounded		
α	no act	SS	PS	no act	SS	PS
0°	0.4451	0.5172	0.3804	0.4431	0.5171	0.3785
6°	1.1443	1.1932	1.0553	1.1450	1.1910	1.0487

Table 4.2: Aerodynamic properties for rounded and sharp trailing edge NACA4415.

model. Figure 4.49 shows a C_p comparison at the trailing edge ($\alpha = 0°$) between the detail and RSSJ model for three different levels of SS actuation. The time averaged C_p spike close to the synthetic jet outlet is well represented by the RSSJ model for the different levels of actuation but some differences can be observed in the pressure distribution on the trailing edge especially at 0.75 of full actuation.

The actuator effectiveness (ΔC_l and ΔC_m) was also computed for the RSSJ model at different angles of attack as shown in figures 4.50 and 4.51. A very good agreement was achieved between the RSSJ model and the detailed model not only
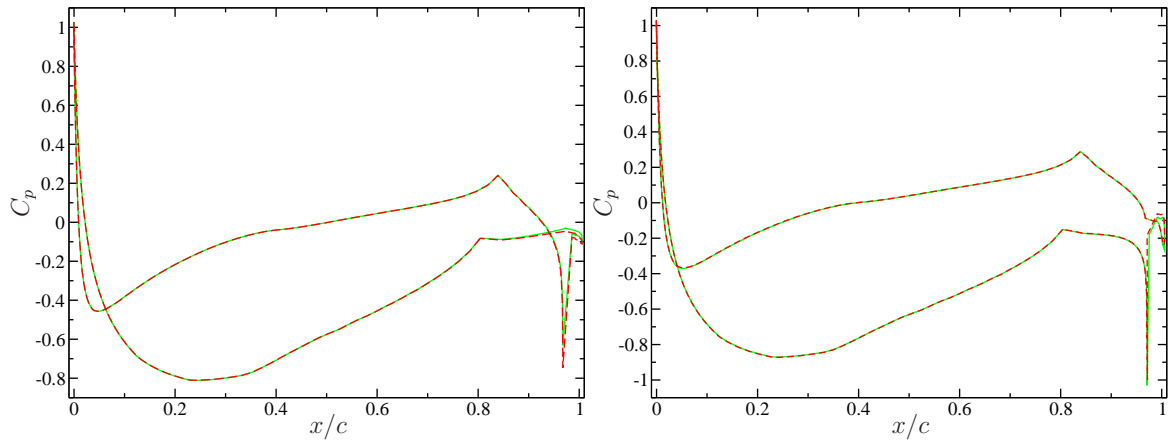
Figure 4.48: Pressure coefficient at $\alpha = 0°$ for the PS (left) and SS (right) actuation. (Detailed model — RSSJ model – –)

in the trends but also in the magnitude of the effectiveness. Even though the calibration of the RSSJ model was done for $0°$, $6°$ and $-6°$, the model performs well at intermediate angles of attack like $-2°$ and $3°$.

Finally, table 4.3 shows a ΔC_m comparison between the experimental and computational results for both actuators and both models at different levels of actuation. Jet strength (JS) in this computational study is defined as the nondimensional A (amplitude of boundary condition) while in the experiments is defined by the input voltage, so a mapping function between A and voltage to match the actuator effectiveness needs to be created to perform dynamic simulations with the controller. It is clear that in the computational results the actuator effectiveness is highly reduced at $JS = 0.25$ making a correct measurement of ΔC_m difficult. This reduction in the actuator performance is in agreement with the formation criteria for synthetic jets as described in section 4.3.3.1.

120
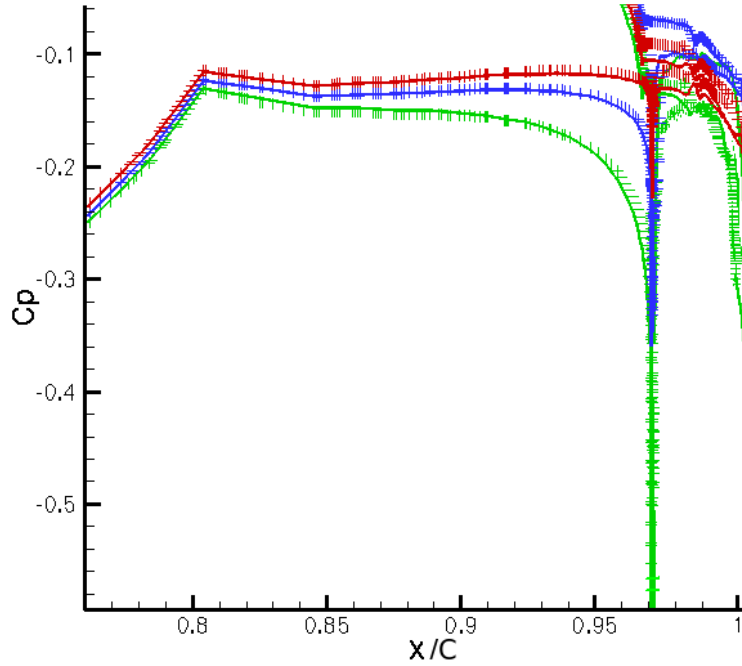
Figure 4.49: Time averaged C_p close to the trailing edge at $\alpha = 0°$ for the SS actuation and different levels of actuation. (Detailed model solid line and RSSJ model dashed line. Colors indicate: 0.75, 0.5 and 0.25 of full actuation)

4.3.4.3 Dynamic simulation

To test the capabilities of the RSSJ model, a dynamic simulation of the modified NACA4415 was performed using a moving mesh implementation in CDPv2.3[66]. This implementation is based on a conservative formulation of the Navier-Stokes equation in a non-inertial reference frame, and it does not require remeshing or volumetric source terms in the NS equation [72]. The dynamic test pursued in this study consists on forcing the airfoil to pitch with a frequency of $0.5U_\infty/c$ in a prescribed angle of attack given by

$$\alpha = -2.5(1 - \cos(\pi T)) \tag{4.14}$$

121
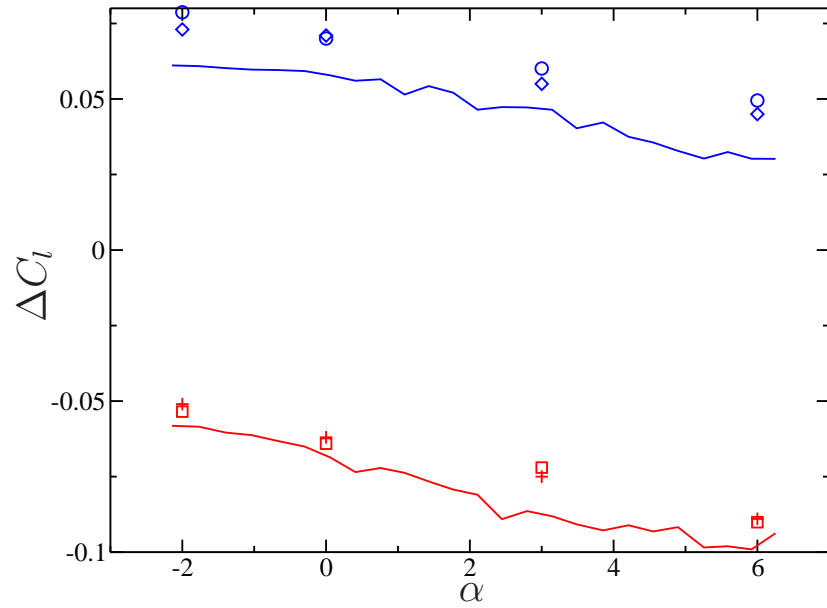
Figure 4.50: ΔC_l and as a function of α. (SS exp $-$ PS exp$-$ SS detailed model $\circ$ PS detailed model $+$ SS RSSJ model $\diamond$ PS RSSJ model $\square$)

The actual dynamic maneuver frequencies in the wind tunnel are about one order of magnitude slower than this test case, so that there are not experimental data available for comparison. The initial condition for the pitching airfoil simulation is a static airfoil at $\alpha = 0°$, and five different cases were pursued: dynamic no actuation, dynamic SS actuation (detailed model), dynamic SS actuation (RSSJ model), dynamic PS actuation (detailed model) and dynamic PS actuation (RSSJ model). All simulations were run for ten pitching cycles to compute estimates of the vorticity and aerodynamic properties phase averages. Figure 4.52 shows the instantaneous vorticity field in the wake after 9.5 pitching periods i.e $\alpha = -5°$ and $T = 19.5$ after the dynamic motion was initialized. The vortex street shows a sinusoidal undulation due to the motion of the airfoil and the vortices are weaker and smaller than in the static case. There are
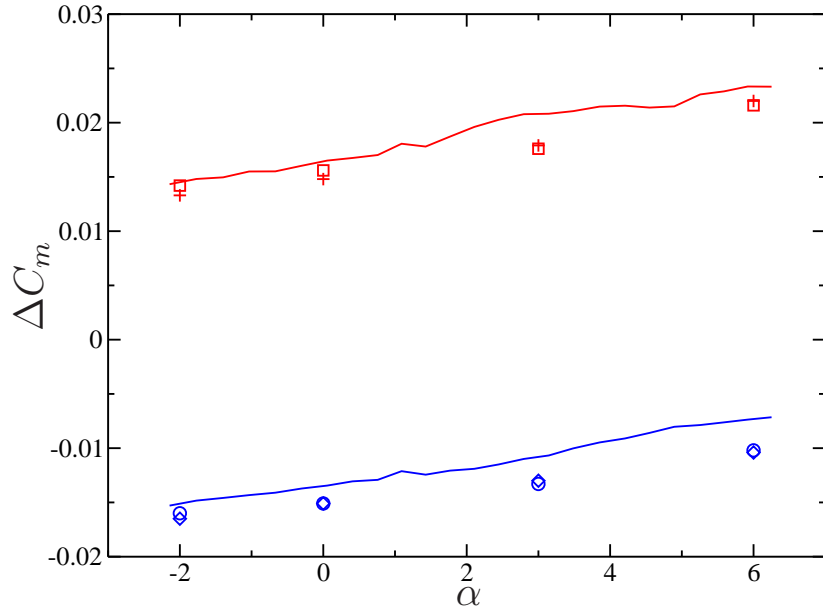
Figure 4.51: ΔC_m and as a function of α. (SS exp $-$ PS exp$-$ SS detailed model $\circ$ PS detailed model $+$ SS RSSJ model $\diamond$ PS RSSJ model $\square$)

no remarkable differences in the far wake due to the actuation, but in the near wake the PS actuation shows a minor stabilization of the vortex shedding at this specific moment in the airfoil maneuver.

The phase averaged vorticity in the near wake at the maximum pitch up case $(\alpha = -5°)$ is shown in figure 4.53 for all actuation cases and both models. As in the static case, there is a downwash of the near wake with SS actuation and an upwash with PS actuation. There are some differences in the vorticity distribution between the detailed and RSSJ models, similar to those observed in the static case, but in general the RSSJ model captures the effect of actuation reasonably well.

A more interesting result is the evolution of the aerodynamic properties, in

SS Exp			PS exp		
α JS / −6°	0°	6°	−6°	0°	6°
1/4	-0.0028	-0.0023	-0.002	0.002	0.0022	0.0027
1/2	-0.0084	-0.0066	-0.0041	0.0046	0.0063	0.0071
3/4	-0.012	-0.0116	-0.0066	0.008	0.011	0.0117
1	-0.018	-0.015	-0.010	0.011	0.015	0.022
SS detail			PS detail		
α JS / −6°	0°	6°	−6°	0°	6°
1/4	-0.0015	-0.0007	-0.0002	0.0021	0.0025	0.003
1/2	-0.0054	-0.0035	-0.0019	0.0038	0.0042	0.0043
3/4	-0.0155	-0.0114	-0.0091	0.0072	0.010	0.0102
1	-0.0245	-0.0173	-0.0114	0.0142	0.0152	0.0178
SS RSSJ			PS RSSJ		
α JS / −6°	0°	6°	−6°	0°	6°
1/4	-0.001	-0.0005	-0.0003	0.002	0.0022	0.0025
1/2	-0.0055	-0.0025	-0.0013	0.0037	0.0045	0.0047
3/4	-0.014	-0.012	-0.0074	0.0087	0.012	0.0123
1	-0.0239	-0.0167	-0.0113	0.0140	0.016	0.019

Table 4.3: ΔC_m comparison between experiments and synthetic jet models at different levels of actuation.

particular, C_l and C_m. Figure 4.54 shows the evolution of C_l for two pitching periods including both models and the unactuated case in which C_l varies between -0.25 and 0.5. The static values of C_l for $\alpha = -6°$ and $\alpha = 0°$ are $0 - 0.21$ and 0.45 respectively. For the detailed model the evolution of the aerodynamic properties is the superposition of three frequencies (actuation, shedding and pitching) while for the unactuated case and RSSJ model there is a superposition of two frequencies (shedding and pitching). As in the static case, a lift enhancement with respect to the unactuated case is observed for the SS actuation and a lift reduction for the PS actuation. The

124
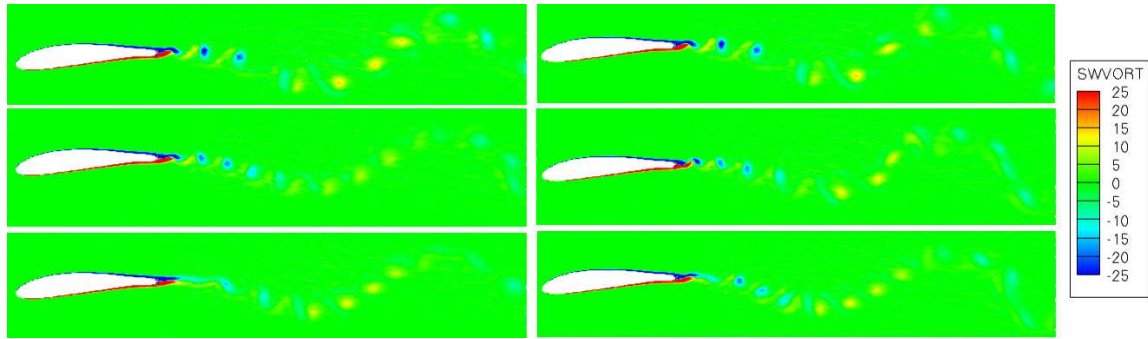
Figure 4.52: Instantaneous vorticity field on the wake for the dynamic test. Top to bottom: no actuation, SS actuation and PS actuation. Detailed model (left column) and RSSJ model (right column)

RSSJ model appears to follow the average behavior of the detailed model. Similar results were found for the evolution of C_m (not shown).

A phase average of the aerodynamic properties was performed using the data for 10 pitching periods and plotted against time and α (see figures 4.55 and 4.56). The shift between the actuated and unactuated curves is due to lift enhancement and moment reduction due to the SS actuation and lift reduction and moment enhancement due to the PS actuation, as in the static results. A hysteresis, typical in pitching airfoils, is observed in both aerodynamic properties and in these figures, the C_m loop is counterclockwise which is characteristic of high frequency pitching airfoils [21]. The RSSJ model performance in capturing the average values of the aerodynamic properties is good.

A comparison of the evolution of the aerodynamic properties (five pitching periods) of the RSSJ model and the low pass filtered detailed model is shown in figure 4.57. The RSSJ model has a larger amplitude oscillation at the shedding frequency

125
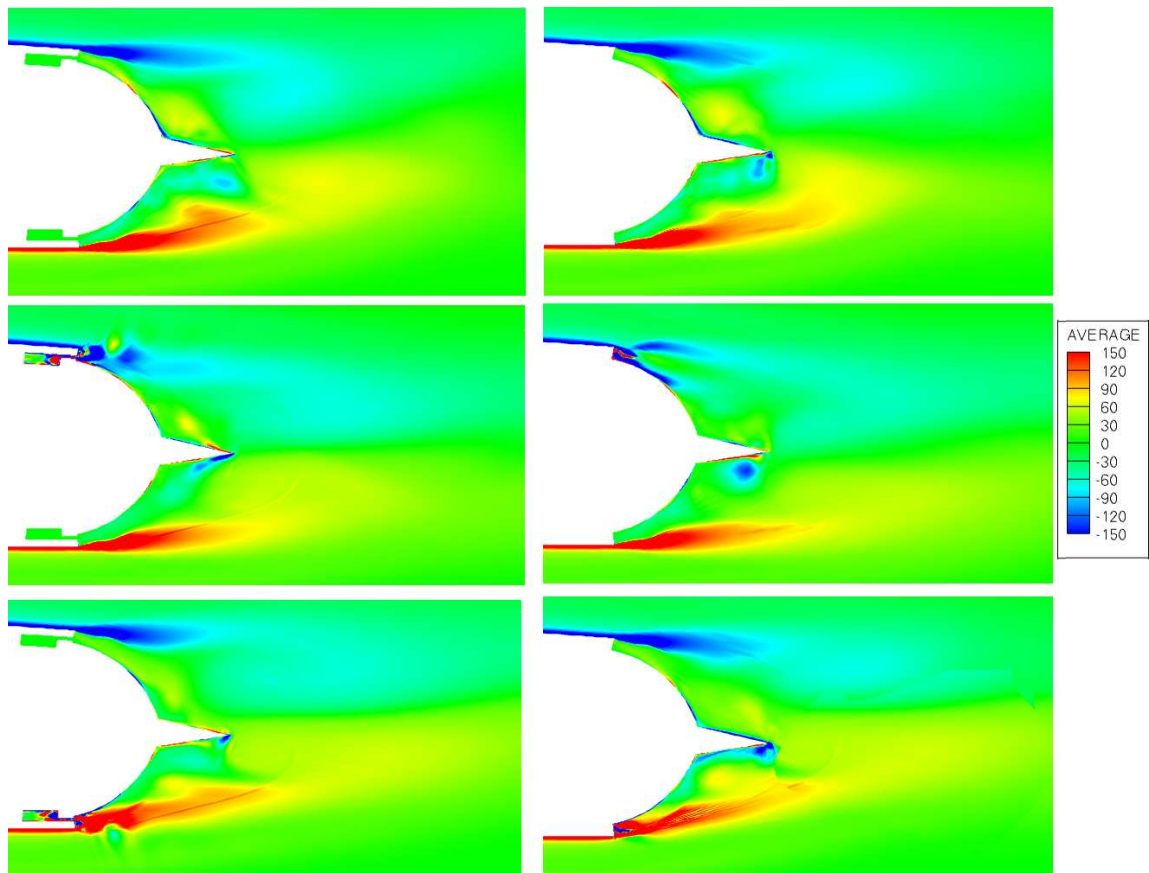
Figure 4.53: Near wake phase averaged vorticity field for a periodically pitching airfoil at maximum pith up ($\alpha = -5°$). Top to bottom: no actuation, SS actuation and PS actuation. Detailed model (left column) and RSSJ model (right column)

than the detailed model and a phase lag is also observed between the two models, which can be attributed to the initial conditions for the dynamic motion (which are slightly different).

Figure 4.58 shows the evolution of the effectiveness of the SS actuation in time for both models. Even though there is an initial phase lag between the two models, the RSSJ model is successful in representing the average behavior of the detailed

126
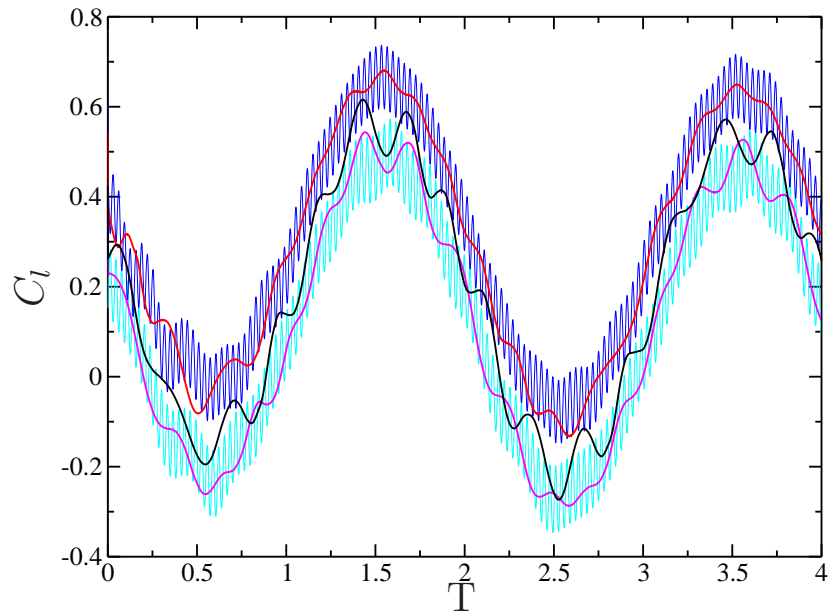
Figure 4.54: Lift coefficient as a function of T (dynamic test). No actuation − SS actuation detail − SS actuation RSSJ − PS actuation detail − PS actuation RSSJ −
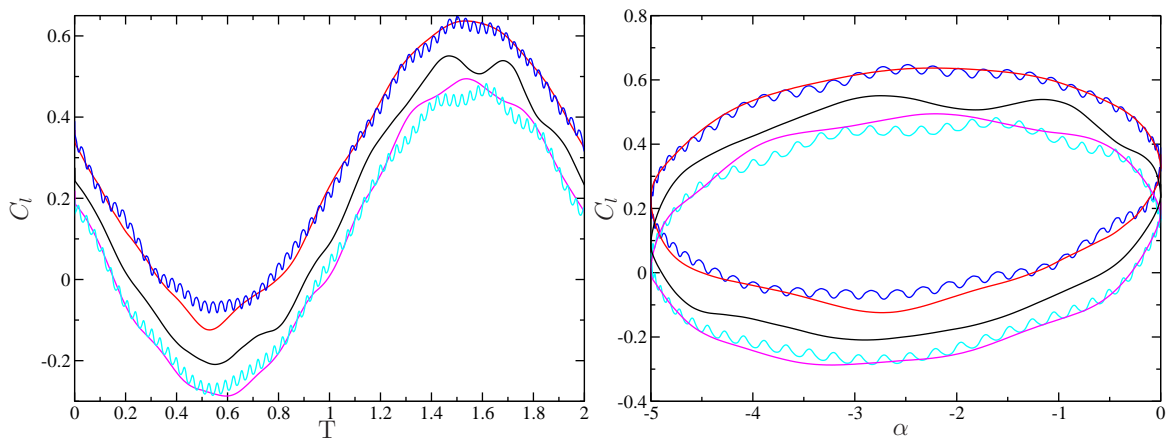
Figure 4.55: Phase average lift coefficient as a function of T (left) and α (right). No actuation − SS actuation detail − SS actuation RSSJ − PS actuation detail − PS actuation RSSJ −

127
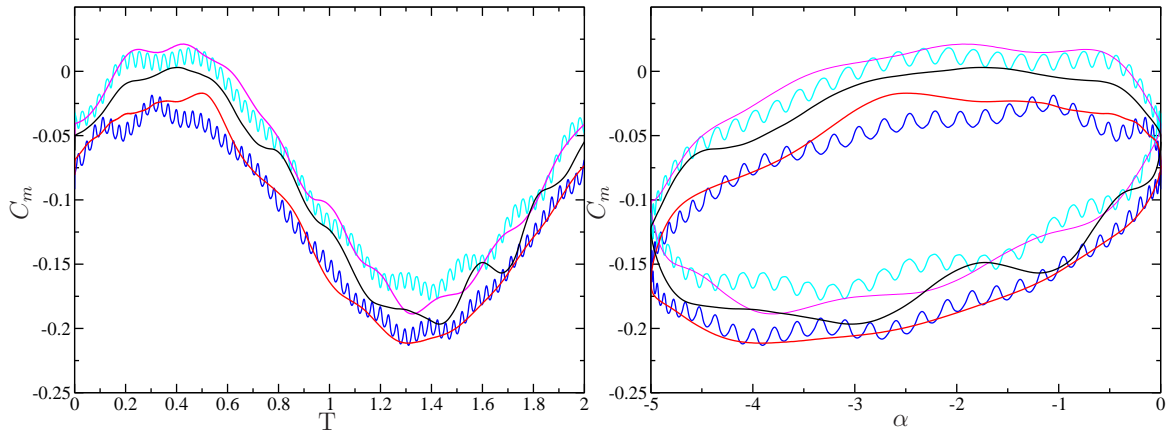
Figure 4.56: Phase average moment coefficient as a function of T (left) and α (right). No actuation − SS actuation detail − SS actuation RSSJ − PS actuation detail − PS actuation RSSJ −
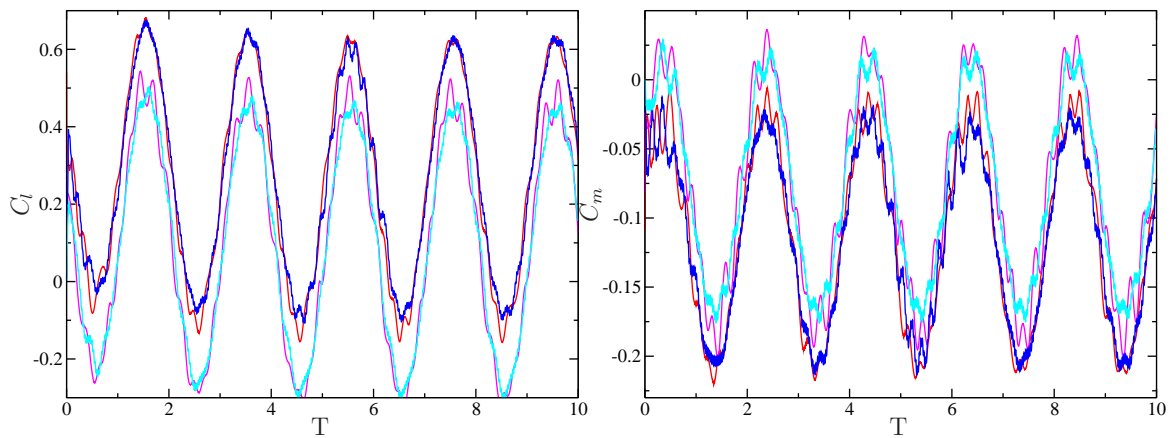
Figure 4.57: Comparison C_l and C_m between RSSJ model and low pass filtered detailed model. SS actuation detail − SS actuation RSSJ − PS actuation detail − PS actuation RSSJ −

128
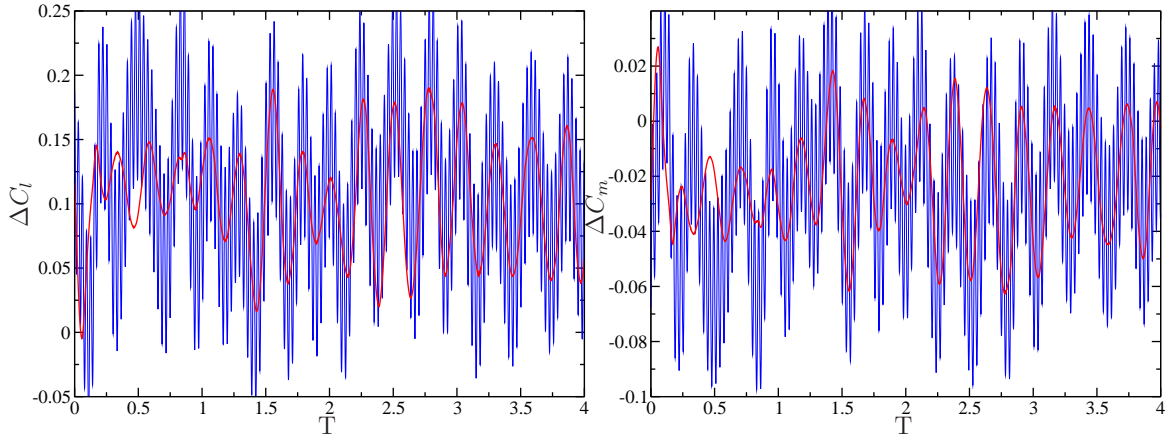
Figure 4.58: Evolution of the suction side actuation effectiveness. Detail — RSSJ —

Effectiveness	SS detail	SS RSSJ	PS detail	PS RSSJ
ΔC_m	-0.023	-0.022	0.0158	0.0155
ΔC_l	0.101	0.099	-0.073	-0.072

Table 4.4: Actuation effectiveness at full actuation in dynamic case

model. Table 4.4 shows the time average values of the effectiveness of both actuators and both models. The lift to moment effectiveness ratio (for both actuators) is about 4.7 which is very close to the static result.

Since the RSSJ model was created for static cases is important to check the performance and evolution of the RSSJ model numerical parameters in time. In order to compute the model control variable moving average, a time constant of $0.5c/U_\infty$ was used, this allows the shedding frequency $(4U_\infty/c)$ but not the pitching frequency $(0.5U_\infty/c)$ to be filtered out. Figure 4.59 shows the evolution of the RSSJ control variable moving average and the evolution of the numerical parameter Γ_1 for SS actuation. These two variables are in phase with the angle of attack and not with the aerodynamic properties, thus these numerical parameters do not show hysteresis.
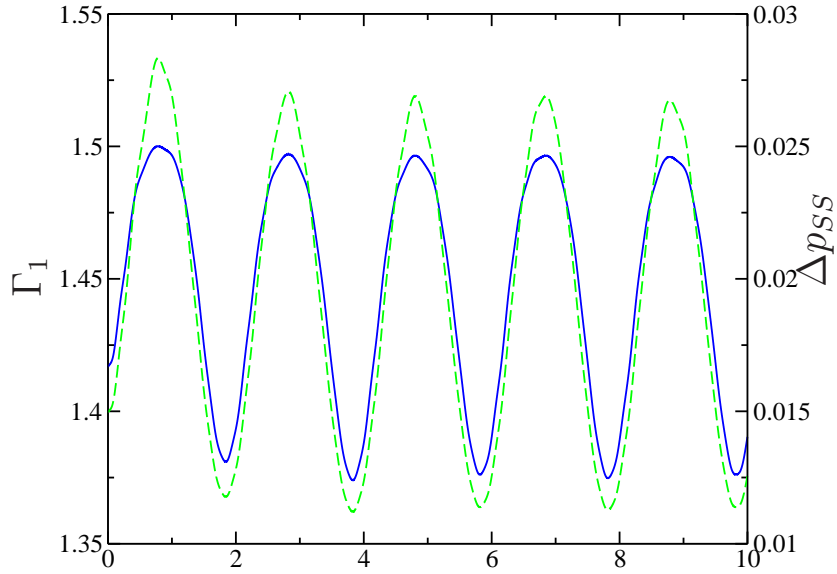
Figure 4.59: Evolution of Γ_1 $(-)$ and Δp for the suction side actuation $(--)$

4.3.4.4 Computational cost

The idea of developing a synthetic jet model by using the time-averaged Reynolds stress field induced by the jet is to reduce the computational cost of the detailed model. Time advancing with the detailed model is constrained by the frequency of actuation, the higher the actuation frequency the smaller the time step. On the other hand, the RSSJ model eliminates the actuation frequency, therefore it is constrained by the stability/accuracy of the numerical method. A cheaper synthetic jet model represents an advantage, particularly for dynamic simulations in which the frequency of plunging/pitching of the airfoil can be three to four orders of magnitude smaller than the frequency of actuation. Dynamic simulations performed with a detailed synthetic jet model must be run for many convective time units, with a very

130

Model	Time Step (TS)	CFL	CPU time per TS (sec)	CPU time per $\frac{c}{U_\infty}$ (min)
Detail	$3 \times 10^{-4} \frac{c}{U_\infty}$	9 *	1.5	84
RSSJ	$1.5 \times 10^{-3} \frac{c}{U_\infty}$ *	30	1.9 *	21
No act	$1.6 \times 10^{-3} \frac{c}{U_\infty}$ *	30	1.8 *	19

* Average value

Table 4.5: CPU time for static simulations

small time step, making the simulations very expensive. For example, forced pitching maneuvers in the wind tunnel are normally executed at a frequency of $0.5Hz$ or $0.007U_\infty/c$ [89], while the actuation frequency is $2050Hz$ or $31.24U_\infty/c$. Assuming that a simulation like this must extent for ten periods of simulation and that in order to correctly discretize an actuation period 100 steps are required, then the time step is about $3 \times 10^{-4}c/U_\infty$ while the simulation has to be run for $1313c/U_\infty$, this means that for a simple dynamic simulation about 4.5×10^6 time steps are needed.

Table 4.5 summarizes the computational cost (in CPU time) of a static simulation ($\alpha = 0°$, $Re = 9 \times 10^5$ and full actuation) for the detailed and RSSJ models. These results were obtained using 32 CPUs in parallel on a 264-CPU cluster machine called Reynolds [3]. Reynolds has 64 compute nodes each one with four Intel Xeon processor 5140 Woodcrest (64 bit at 2.33 GHz), 8Gb in RAM and infiniband interconnected.

In these tests the detailed model was advanced in time with a constant time step while the RSSJ model was advanced in time with a fixed CFL number. The RSSJ model spends more CPU time per time step in comparison to the detailed

---

[3]http://reynolds.ae.utexas.edu

model, because it takes a couple of more iterations in the Bi-CGSTAB solver. Even though the time step used in the RSSJ model is 5 times the time step used in the detailed model, the actual speed up achieved by the model is a factor of 4. This speed up is significant for dynamic simulations which are computationally expensive, for example: Performing detail simulations such as the actuated cases of the dynamic test shown in section 4.3.4.3, takes ≈ 3 hours per pitching cycle instead of ≈ 1 hour for the RSSJ model. Table 4.5 also shows a comparison between the RSSJ model and an unactuated simulation. It is clear that for a fixed CFL number, the RSSJ model is slightly more expensive than the unactuated case due to the momentum sources introduced in the Navier-Stokes equation.

4.4 Dragon Eye

The Dragon eye airfoil is the actual profile that will be used in the UAV at Georgia Tech, so it is important to test the different models used in the NACA4415 performance on this airfoil. Several simulations of a Dragon Eye profile were conducted for a wide range of angles of attack (section 4.4.1) and validated with available experimental data. Then, simulations of a modified Dragon Eye section (no actuation - section 4.4.2 - and with actuation using the detailed model -section 4.4.3) were performed but could not be validated due to the lack of experimental data. Finally, the capabilities of the Reynolds Stress Synthetic Jet model were tested with this modified Dragon Eye profile (section 4.4.4). The same grid generation guidelines followed for the NACA4415 were applied to the Dragon Eye airfoil, providing a mesh with the same regions and similar characteristics.

4.4.1 Unmodified

The angle of attack for this first set of simulation was set from $-6°$ up to $15°$ and a $Re = 3.6 \times 10^5$ to match the experimental conditions at the Georgia Tech Research Institute (GTRI). A complete validation of the computational results obtained in this study can not be performed since some details of the experimental set-up at GTRI were unknown. Nevertheless it is known that the facility at GTRI is a two-dimensional wind tunnel (Dragon Eye model spans through the entire tunnel) so even without the corrections it is expected to be a fairly good agreement between the computational and experimental data. Figure 4.60 shows lift and moment (at quarter chord) coefficients along with the experimental results at GTRI, with good agreement between the computational and experimental results specially for the C_m and C_l curve slopes. In fact,the positive magnitude of C_l curve slope and the negative value of C_m curve slope at low angle of attack was correctly predicted by the CFD model. Similar to the results for the NACA4415 (see section 4.3.1), in the stall region ($\alpha > 12°$) the computational aerodynamic properties highly depend on the spanwise domain length. The polar plot (figure 4.61) shows an underprediction of C_d relative to the experimental results which could be related to the lack of correction of C_d for wind tunnel effects and a possible underprediction of the skin friction coefficient by the DDES model. Due to the reflexed camber line of the Dragon Eye profile, at low angle of attack the attached boundary layer experiences adverse pressure gradients which can be inadequately modeled, affecting the prediction of the shear stress and C_d.

Computational and experimental results for the time average C_p along the

133
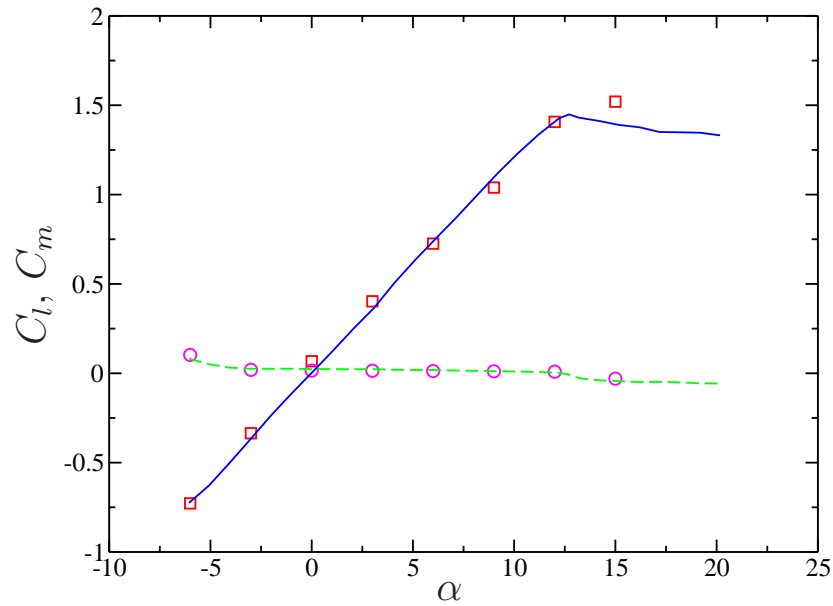
Figure 4.60: Comparison of lift and moment coefficient with experimental data for the Dragon Eye airfoil. C_l exp— C_l comp □ C_m exp-- C_m comp ○

airfoil surface also show very good agreement as shown in figure 4.62 for $\alpha = 0°$ (left) and $\alpha = 15°$ (right). It is clear that the peak value of the pressure close to the leading edge is well captured in the computational experiments at both angles of attack. At $\alpha = 15°$, C_p is over predicted especially in the pressure side of the airfoil, this could be attributed to the fact that at this angle of attack the flow is separated and it requires long simulations to correctly predict the average properties.

Even though there are not PIV measurements available from the experiments to compute the vorticity field, it is relevant to analyze the characteristics of the vorticity field for this wing section in special at a high angle of attack. Figure 4.63 shows an instantaneous vorticity field at $\alpha = 15°$, it is clear that the flow is separated at a location close to $x/c \approx 0.25$. After the flow is separated a shear layer is formed
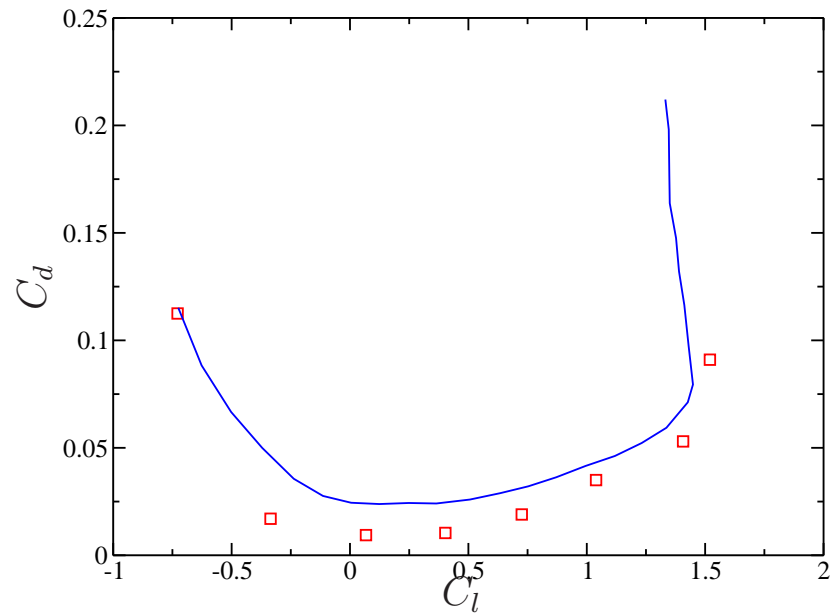
Figure 4.61: Comparison of the polar plot with experimental data for the Dragon Eye airfoil. Exp— Comp □
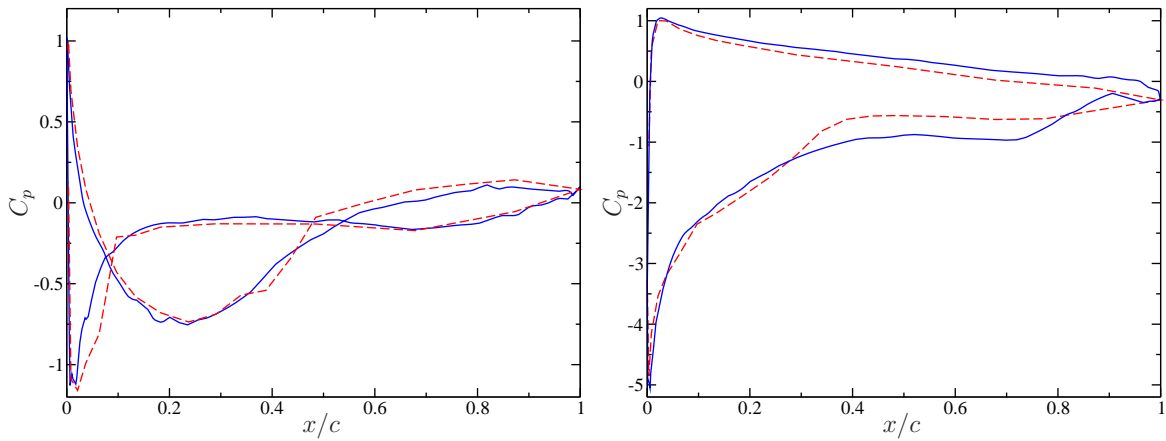
Figure 4.62: Comparison of pressure coefficient with experimental data for the Dragon Eye airfoil at $\alpha = 0°$ (left) and $\alpha = 15°$ (right). Comp — Exp——
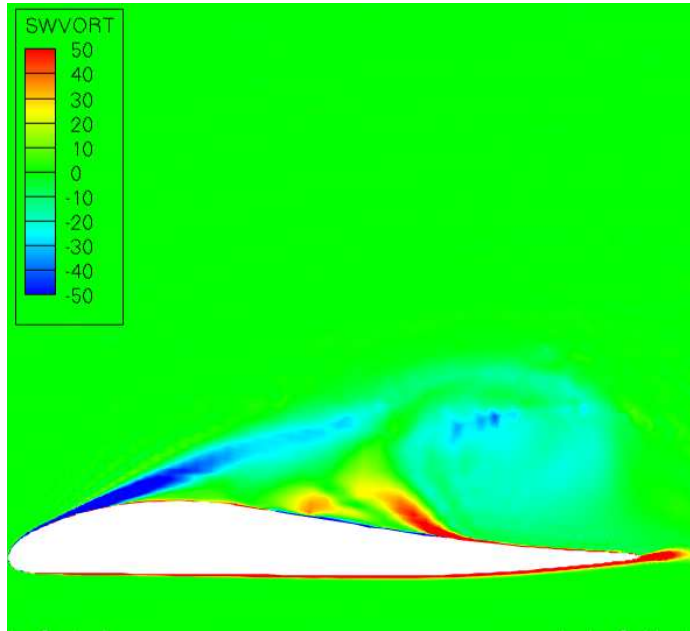
Figure 4.63: Instantaneous vorticity field at $\alpha = 15°$ (Dragon Eye)

and then it rolls up into a clockwise vortical structure that is later separated and convected downstream.

4.4.2 Modified unactuated

Though the modifications to the Dragon Eye profile to accommodate the actuators has not been designed yet by the experimental group at Georgia Tech, it was considered important to exercise DDES and the synthetic jet models for this airfoil. The modified Dragon Eye geometry was created using three inputs: the Dragon Eye profile, the actuator geometry and the position of the synthetic jet outlet relative to the trailing edge used in the NACA4415 case. The resulting geometry is shown in figure 4.64). Several computational experiments were performed for this geometry

136
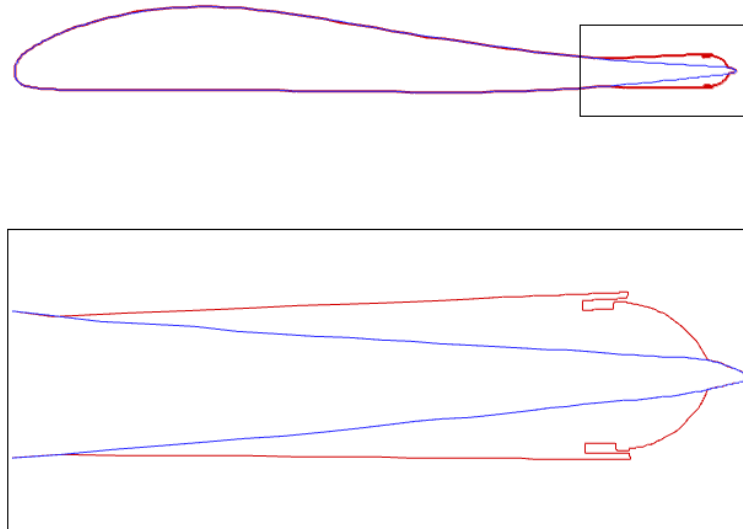
Figure 4.64: Modified Dragon Eye geometry. (Unmodified— modified—)

with $Re = 9 \times 10^5$ and a range of angles of attack between $-2°$ and $9°$.

Figure 4.65 shows the time average vorticity field close to the trailing edge for an angle of attack of $0°$. The size and magnitude of the vorticity in the recirculation region (downstream the trailing edge) are very similar to the modified NACA4415. But, the size and magnitude of the co-rotating vortices (that appear in each side of the airfoil close to the trailing edge) are larger for the modified Dragon Eye section.

The instantaneous spanwise vorticity in the wake of the Dragon Eye airfoil ($\alpha = 0°$) also shows a clear vortex street (see figure 4.66). In comparison to the NACA4415 this vortex street is thinner, the magnitude of the vortices is weaker and the distance between vortical structures slightly smaller ($\approx 0.21x/c$). A Fourier analysis of the evolution of C_m revealed that the dominant frequency is $St \approx 4.7$ which is to the strouhal number based on the chord.
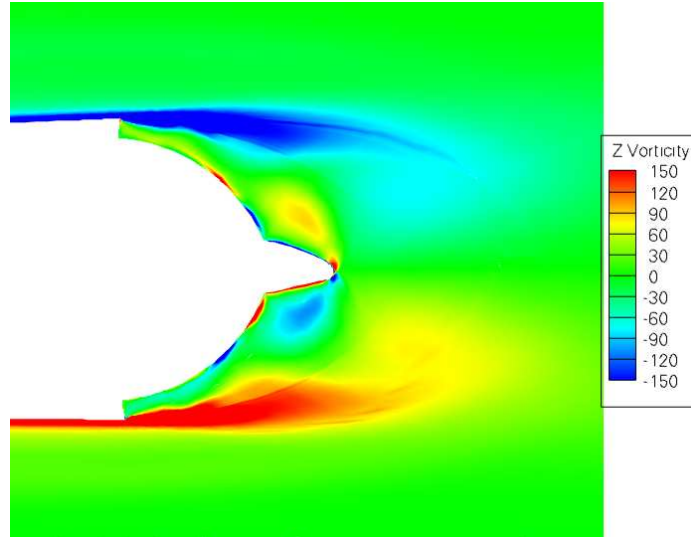
Figure 4.65: Time average vorticity field in the near wake (Dragon Eye).
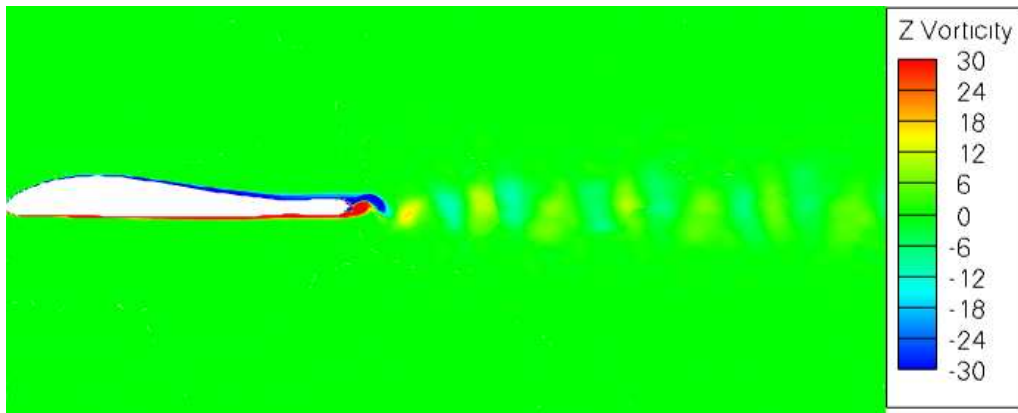
Figure 4.66: Instantaneous vorticity field for the Dragon Eye airfoil at $\alpha = 0°$.
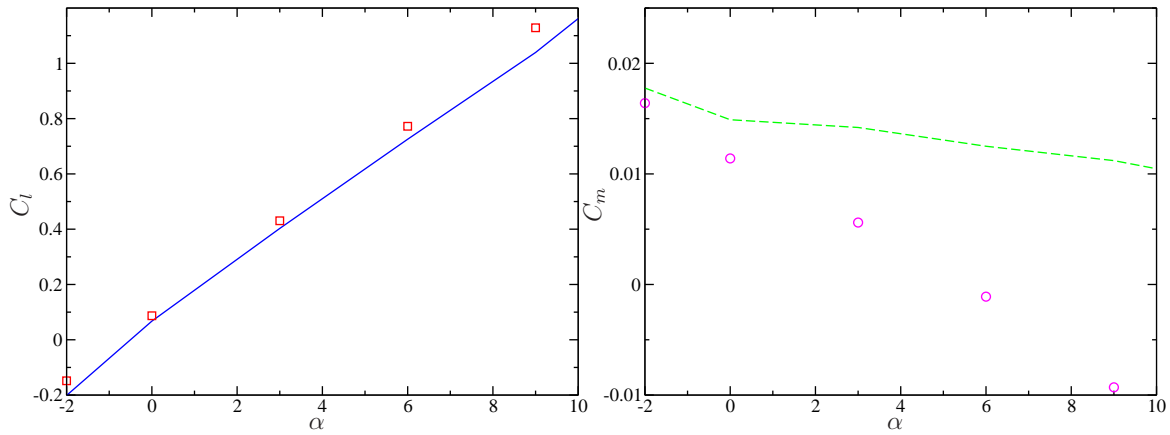
Figure 4.67: C_l and C_m vs α for the Dragon eye airfoil. C_l unmodified $-$ C_l modified $\square$ C_m unmodified $--$ C_m modified $\circ$

Figure 4.67 shows C_l and C_m for the modified Dragon Eye along with the unmodified profile for a range of angles of attack between $-2°$ to $9°$. The magnitude and slope of the C_l curve is slightly altered while the C_m curve is strongly affected by the modification. The C_m slope, in both unmodified and modified profiles, remains negative which is a primary requirement for static stability of the airfoil. $\frac{\partial C_m}{\partial C_l}$ is ≈ -0.007 and ≈ -0.018 for the unmodified and modified sections respectively, based on this calculation the Dragon Eye section has an aerodynamic center located at $x/c \approx 0.257$ while for the modified Dragon Eye is located at $x/c \approx 0.268$ so that the effect of the geometrical modification is the translation of the aerodynamic center towards the trailing edge. For both, the NACA4415 and Dragon Eye profiles, the displacement of the aerodynamic center was $O(10^{-2})$ which is consistent with the experimental results for different NACA profiles with increases in the airfoil thickness at $x/c = 0.9$ of the same order[97]
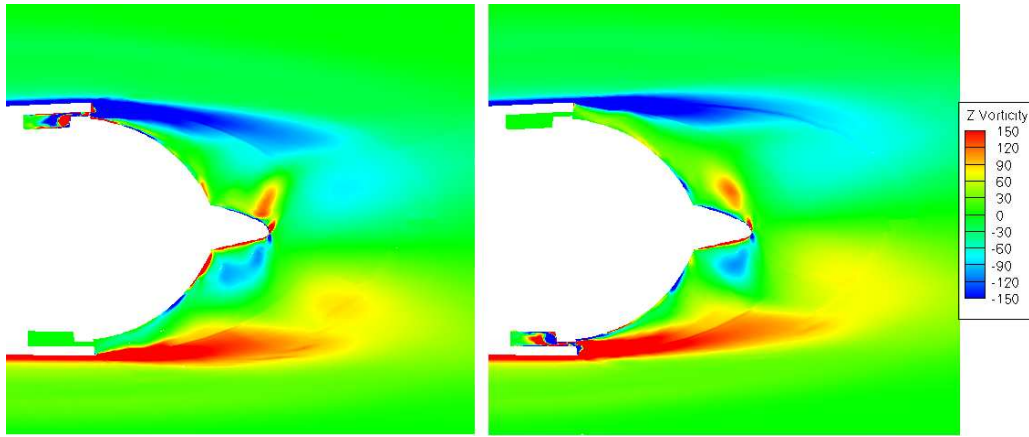
Figure 4.68: Time average vorticity field in the near wake for the dragon eye at $\alpha = 0°$. SS actuation (left) PS actuation (right)

4.4.3   Modified actuated - Detailed Model

This set of computational experiments were performed for full actuation only for a range of α between $-2°$ to $9°$. The non-dimensional frequency of actuation (F^+) was set to 31.24 and the amplitude of the boundary condition was set to $0.38U_\infty$ based on the average amplitude (between the PS and SS actuation) used in the NACA4415 case. The time step was also set to 3×10^{-4} to ensure ≈ 100 steps per actuation cycle. The effects of the actuation on the average spanwise vorticity close to the trailing edge for the Dragon Eye (see figure 4.68) is very similar to the ones observed in the modified NACA4415 (see figure 4.13). There is clear bending of the shear layer towards the coanda surface compared to the unactuated case. It is also appreciated a downwash of the near wake for the suction side actuation and an upwash of the near wake for the pressure side actuation. Similar to the NACA4415 with the rounded trailing edge, the vortical structures in the near wake are shorter than in the unactuated case.
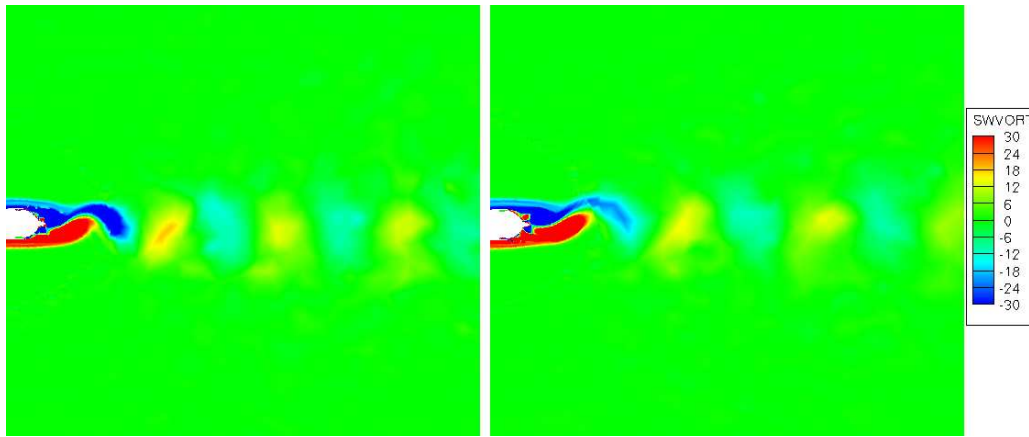
Figure 4.69: Instantaneous vorticity field of the wake for the dragon eye at $\alpha = 0°$. SS actuation (left) PS actuation (right)

Figure 4.69 shows the effects of the actuation in the instantaneous vorticity field in the wake at $\alpha = 0°$. A Fourier analysis of the evolution of the aerodynamic properties in time showed that the dominant frequency in both actuation cases was close to ≈ 4.8 and no stabilization of the wake was observed. This is consistent with the results obtained in the rounded trailing edge NACA4415 and gives support to the hypothesis that the stabilization of the wake in the actuated cases is associated to the geometry at the trailing edge.

The effects on the aerodynamic properties are the same as those observed for the NACA4415 airfoil i.e: for SS actuation a reduction of C_l associated with an increment of C_m and vice versa for the PS actuation. Figure 4.70 show the effectiveness of the actuation, computed as changes in the aerodynamic properties (ΔC_m and ΔC_l) including the NACA4415 results for comparison. The trends on these curves is very similar to the results in the NACA4415, except for the fact that the SS actuation
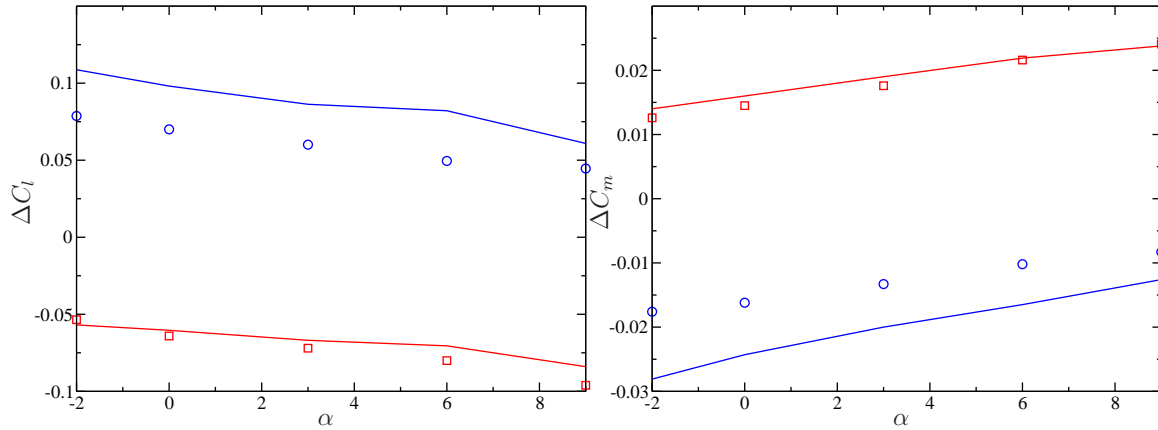
Figure 4.70: ΔC_l and ΔC_m as a function of α for the Dragon Eye airfoil. (SS $-$ PS $-$ SS NACA4415 $\circ$ PS NACA4415 $\square$)

effectiveness is stronger compared to the PS actuation and to the NACA4415 results. Similar differences between the SS and PS actuation have also been experimentally observed with the same type of actuators in the NACA4415 model with a different piezoelectric disks[89].

4.4.4 Modified actuated - RSSJ Model

The simplified (seven-parameters) RSSJ model was implemented for the Dragon Eye airfoil and tested over a range of angles of attack between $-2°$ and $6°$ and full actuation. Appendix E shows the values of the numerical parameters used to calibrate the model which are basically the same used for the NACA4415 except for some changes in the source locations and strength. Figures 4.71 and 4.72 show the time averaged vorticity in the near wake and the instantaneous vorticity field in the wake for both actuation. The similarity with the detailed model is remarkable (see figures 4.68 and 4.69).
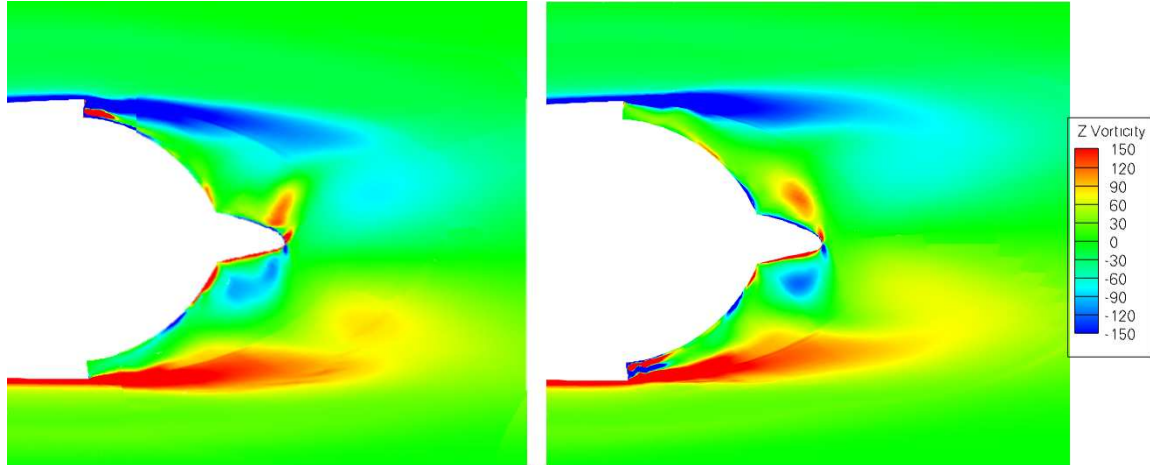
Figure 4.71: Time average vorticity field in the near wake for the dragon eye at $\alpha = 0°$ (RSSJ model). SS actuation (left) PS actuation (right)
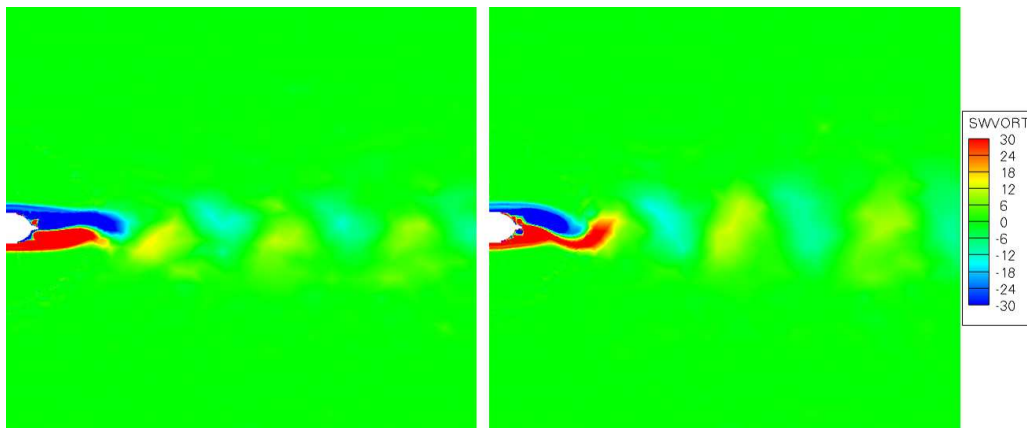
Figure 4.72: Instantaneous vorticity field of the wake for the dragon eye at $\alpha = 0°$ (RSSJ model). SS actuation (left) PS actuation (right)
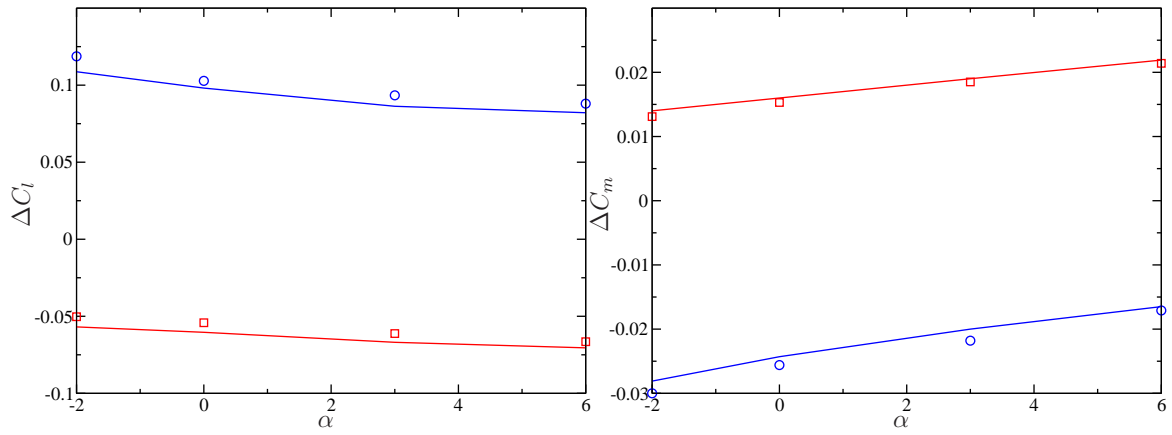
Figure 4.73: ΔC_l and ΔC_m as a function of α for the Dragon Eye airfoil. (SS detail — PS detail— SS RSSJ ∘ PS RSSJ □)

Finally, figure 4.73 shows the effectiveness of the actuation for the RSSJ model and a comparison with the detailed model, in which trends are similar between the two models. The RSSJ model capabilities to capture the average behavior of the detailed model is further demonstrated with this test.

144

Chapter 5

Conclusions and future work

5.1   Conclusions

A computational study of a NACA4415 airfoil with synthetic jet control was presented. For this study, an implementation of the delayed detached eddy simulation (DDES) turbulent model in a nearly kinetic energy conserving CFD code was developed. Two different synthetic jet models were presented and evaluated: detailed and RSSJ models, which were calibrated and validated with experimental data provided by Dr Glezer's group at Georgia Tech. Numerical results demonstrated the effects of the synthetic jets actuation on the flow field and on the aerodynamic properties of the airfoil. The performance and capabilities of the RSSJ model were tested in a dynamic simulation and static simulation on a different airfoil (the Dragon Eye).

5.1.1   CFD code, turbulent model and grid generation

CDPv2.3 a parallel unstructured grid incompressible flow solver developed in the Center of Integrated Turbulent Simulations at Stanford was selected as the CFD code because it satisfies the requirements needed in this dissertation in particular due to its kinetic energy conserving properties. CDPv2.3 as provided by CITS is an LES code, so the selection and implementation of a turbulent model was necessary. A hybrid RANS/LES turbulent model called Delayed detached eddy simulation (DDES)

145

was selected to be implemented on CDPv2.3. DDES is designed to use a RANS representation for boundary layers, and LES in separated regions and wakes. In implementing DDES, one of the hardest properties to preserve in the SA equation discretization is the positivity of $\tilde{\nu}$ which depends on different factors such as: time discretization, numerical solver and type of grid used. In hybrid RANS/LES models the transition from RANS to LES relies on the grid. A hybrid grid was generated with a structured grid close to the airfoil (RANS region) and unstructured grid elsewhere (LES and Euler regions). One important parameter in the grid generation is the LES filter size (Δ_o) which corresponds to the spanwise grid size to ensure an isotropic mesh in the LES region, here $\Delta_o = 0.02$. The mesh generation in the airfoil surface normal direction requires some prior knowledge of the flow such as: expected boundary layer thickness and transition location. Using a panel method with integral boundary layer representation was effective in determining these quantities leading to a successful grid generation process. The model was tested on a flat plate boundary layer and a massively separated flow. In the latter, it was discovered that in the wake the eddy viscosity was not reduced to values appropriated for LES. This was improved by extending the implementation to Extended DDES (EDDES)[99][98].

5.1.2 Validation and results of unactuated cases

Numerical results for the NACA4415 were satisfactory at low angle of attack in which C_l and C_m were in agreement with legacy data. At high angle of attack, some differences in the aerodynamic properties between the numerical results and legacy data were observed, which was likely due to spanwise domain size. Nevertheless

good agreement with experimental results at GA Tech were obtained at $\alpha = 19°$ for C_p distribution and time-average vorticity field. Better agreement was observed in the aerodynamic properties (including C_d) between the numerical and experimental results for the modified NACA4415 section. Regarding the time-averaged vorticity field in the near wake, computational results show good agreement in the size and magnitude of the recirculation regions. On the other hand, stronger concentrations of vorticity close to the airfoil surface was observed in the computational results that was attributed to higher resolution of the CFD in this part of the domain compared to the PIV measurements. Another validation observation is that the modification of the airfoil (due to the actuators) moves the aerodynamic center $\approx 0.025c$ towards the trailing edge consistent with legacy experiments on NACA profiles.

5.1.3 Synthetic jet models

The effect of the synthetic jet actuators was first represented using a temporally and spatially resolved model of the action of the jet. The oscillation of the piezoelectric disk is modeled with a sinusoidal velocity boundary condition normal to one of the cavity walls, using an amplitude and frequency that match the experimental conditions. The detailed model fully captures the dynamics of the synthetic jet actuator but it increases the complexity of the simulation due to the cavity geometry and high actuation frequency. A major disadvantage of this model is that resolving the jet frequency requires a 5 times smaller time step than would otherwise be necessary. A new synthetic jet model representing the Reynolds stress field arising from the jet was proposed. This model reduces the complexity of the simulation and the

required time step. In its simplest implementation, the RSSJ model required seven numerical parameters to completely model the effects of the synthetic jet strength and angle of attack.

5.1.4   Validation and results of actuated cases

Based on the numerical results obtained from the different actuated cases, it can be concluded that:

- Since the actuators are located close to the trailing edge, there is an important influence of the precise trailing edge geometry on the synthetic jet model prediction of S_t and the spanwise vorticity field in the wake. With a sharp trailing edge, changes in S_t were observed for both actuation, while with a rounded trailing edge these changes were not observed. Numerical results of the PS actuation showed a wake stabilization that could be related to the reduction of the turbulent kinetic energy already observed in experiments[17].

- Based on a simple three-dimensional synthetic jet model implemented here, the three dimensional effects of the synthetic jets already observed in experiments[9] were corroborated. This three-dimensionality has a stronger impact on the spanwise vorticity field in the wake than on the airfoil aerodynamic properties and synthetic jet effectiveness.

- The assumption of identical synthetic jets on both sides of the airfoil was not valid since the computational effectiveness of the PS actuation showed differences with experiments. A small geometrical modification in the angle between

148

the synthetic jet outlet and the coanda surface was need to effectively match the detailed model to experimental observations. It can be concluded that a correct validation of a tangential synthetic jet model requires a precise representation of the experimental actuator geometry.

- The evolution of the vorticity field close to the synthetic jet outlet at full actuation showed a clear formation of a synthetic jet in which a pair of counter rotating vortices that are created in each actuation cycle and convected downstream by the cross flow. These vortices interact with a shear layer that is formed at the end of the actuator ramp and with the vorticity close to the wall of the coanda surface. At 1/4 of full actuation the evolution of the vorticity field showed that the pair of counter rotating vortices were sucked back into the actuator cavity during the outstroke phase instead of separating from the synthetic jet outlet. These observations are consistent with the formation criteria for synthetic jets in which $1/F_h^+ >= 1$ in order to create a synthetic jet and with the reduction in the synthetic jet effectiveness at 1/4 of full actuation.

- A synthetic model based on Reynolds stress fields arising from the synthetic jet (RSSJ model), eliminates the high frequencies of actuation while retaining the shedding frequency and amplitude. Elimination of high frequencies is related to larger time steps, so that the time advancing is not constrained. These characteristics make the RSSJ model attractive for flow control simulations with synthetic jets, in which there is a difference of more than 3 orders of magnitude between maneuvering time scale and the actuation time scale.

149

- The simplified RSSJ model demonstrated that by only representing the Reynolds stress field close to the synthetic jet outlet, it is possible to capture the basic actuation effects on the flow field and particularly on the aerodynamic properties. A dynamic simulation of a pitching NACA4415 was used as test of the synthetic jet models used here and results were satisfactory.

5.1.5 Dragon Eye

The methodology followed in the NACA4415 airfoil was tested on a Dragon Eye profile, which is the actual section that will be used in the AVOCET project UAV. Except for some differences in C_d, the unmodified section C_l, C_m and C_p results showed good agreement with the experiments carried on at GTRI, particularly at low angle of attack. The modified Dragon Eye has a near wake similar to the NACA4415, with two main vortical structures and co-rotating vortices close to the airfoil surface. A clear vortex street was also observed with $S_t = 4.7$. A displacement of $\approx 0.011c$ towards the trailing edge in the aerodynamic center was observed due to the section geometrical modification. Similar effect of the actuation in the vorticity field and aerodynamic properties observed in the NACA4415 were also observed in the Dragon Eye profile. The most important observation is that the SS actuation effectiveness is stronger in comparison to the PS actuation and to the NACA4415 results. Minor changes in the NACA 44515 RSSJ model numerical parameters were required to used the model with the Dragon Eye to achieved satisfactory results regarding vorticity field and aerodynamic properties.

5.1.6 AVOCET

In the context of the AVOCET project, this study provided detailed information about the controlled flow that is relevant for the reduced-order model and the development of controllers, that are not available in experiments such as:

- Early evolution of the aerodynamic properties in an impulsive started flow used in the validation of the discrete vortex model.

- Evolution of the vorticity flux very close to the airfoil trailing edge used in the estimation of forces in the discrete vortex model

- Evolution of the aerodynamic properties in high frequency dynamic maneuvers, which are important for the validation of the discrete vortex model, and the development of the flow controller

- Two dimensional velocity fields for actuated and unactuated cases used to test the POD model.

This computational study also provides information relevant to the experimental group at Georgia Tech. For example: Computational experiments showed that moving both actuators to the trailing edge reduced the actuator effectiveness, this result was latter corroborated by experiments.

5.2   Recommendations and Future work

- In the context of DDES, several computational experiments can be performed to further explore and test its performance, for instance: A numerical study

of the influence of the spanwise length and discretization on the aerodynamic properties can be carried on especially with massive separation (high α). Since DDES is a model that is still evolving, new modifications such as a wall-modelled LES or Improved DDES (IDDES) [108] can be also implemented and tested.

- This computational study showed the importance of the trailing edge in determining S_t and the wake vorticity field, consistent with experimental observation. However, the trailing edge geometry used in this computational study does not exactly correspond to that actually presented in the experimental model which has not been documented. Further computational results for AVOCET should use realistic geometrical details of the trailing edge.

- The performance and parametrization of both detailed and RSSJ models could be improved by more precisely matching the experimental data, and for the reduced RSSJ model, using a principal component analysis to reduced the number of parameters.

- In the AVOCET context, implementation of the synthetic jet models used in this dissertation to controlled simulations of airfoils requires a mapping between jet strength and controller input voltage. The RSSJ model should be used in such simulations with a controller as testbed for further controller development.

- While the RSSJ model was developed for a tangential synthetic jet, the methodology used in this study can be extended to normal synthetic jet actuators. This will require computational experiments of normal actuation initially in to quiescent ambient fluid and then into a cross flow.

Appendices

Appendix A

Gradients in CDPv2.3

Applying the Green-Gauss theorem to an scalar ϕ in any interior control volume of the computational domain

$$\int_{cv} \frac{\partial \phi}{\partial x_i} = \int_s \phi ds \hat{n}_i \tag{A.1}$$

Where $\hat{n}_i$ represents a surface normal vector in the ith direction. Assuming that the gradient of ϕ is a constant within the control volume (cv), then

$$\overline{\frac{\partial \phi}{\partial x_i}} V_{cv} = \int_s \phi ds \hat{n}_i \tag{A.2}$$

The right hand side of this equation represents the summation of the fluxes of ϕ through all the faces of cv, which can be expressed as:

$$\int_s \phi ds \hat{n}_i = \sum_{f=1}^{nf} \phi_f A_f \hat{n}_i \tag{A.3}$$

Where ϕ_f is the average value of ϕ at the control volume face. Finally, the gradient of any scalar can be computed as:

$$\overline{\frac{\partial \phi}{\partial x_i}} = \frac{1}{V_{cv}} \sum_{f=1}^{nf} \phi_f A_f \hat{n}_i \tag{A.4}$$

Appendix B

Gridgen script file

```
# Gridgen Journal File to generate mesh for a modified NACA4415
# Developed by Omar Lopez
# Thesis title: "Computational study of a NACA4415 airfoil using synthetic jet control"
# Supervisor: Robert D. Moser
# Department of Mechanical Engineering.
# University of Texas at Austin. 2009
package require PWI_Glyph 1.6.9

# Delete any existing grids and database entities.
#Reset AS/W, defaults, and tolerances.
gg::memClear
gg::aswDeleteBC -glob "*"
gg::aswDeleteVC -glob "*"
gg::aswSet GENERIC -dim 3
gg::defReset
gg::tolReset
gg::updatePolicy DELAYED

#Read the grid file that contains the modified NACA4415 profile.
#Make sure the file is in the correct path.
set _ggTemp_(1) [gg::conImport "./modifiedNACA4415.grd"]
set _CN(1) [lindex $_ggTemp_(1) 0]
set _CN(2) [lindex $_ggTemp_(1) 1]
set _CN(3) [lindex $_ggTemp_(1) 2]
set _CN(4) [lindex $_ggTemp_(1) 3]
set _CN(5) [lindex $_ggTemp_(1) 4]
set _CN(6) [lindex $_ggTemp_(1) 5]
set _CN(7) [lindex $_ggTemp_(1) 6]
set _CN(8) [lindex $_ggTemp_(1) 7]
set _CN(9) [lindex $_ggTemp_(1) 8]
set _CN(10) [lindex $_ggTemp_(1) 9]
set _CN(11) [lindex $_ggTemp_(1) 10]
set _CN(12) [lindex $_ggTemp_(1) 11]
set _CN(13) [lindex $_ggTemp_(1) 12]
set _CN(14) [lindex $_ggTemp_(1) 13]
set _CN(15) [lindex $_ggTemp_(1) 14]
set _CN(16) [lindex $_ggTemp_(1) 15]
set _CN(17) [lindex $_ggTemp_(1) 16]
set _CN(18) [lindex $_ggTemp_(1) 17]
set _CN(19) [lindex $_ggTemp_(1) 18]
set _CN(20) [lindex $_ggTemp_(1) 19]
set _CN(21) [lindex $_ggTemp_(1) 20]
set _CN(22) [lindex $_ggTemp_(1) 21]
set _CN(23) [lindex $_ggTemp_(1) 22]
```

```
set _CN(24) [lindex $_ggTemp_(1) 23]
unset _ggTemp_(1)
#########################################################

#Create other connectors needed fot the RANS region
gg::conBegin
  gg::segBegin -type 3D_LINE
    gg::segAddControlPt [gg::conGetPt $_CN(6) -arc 0]
    gg::segAddControlPt [gg::conGetPt $_CN(5) -arc 0]
  gg::segEnd
set _CN(25) [gg::conEnd]
gg::conBegin
  gg::segBegin -type 3D_LINE
    gg::segAddControlPt [gg::conGetPt $_CN(6) -arc 1]
    gg::segAddControlPt [gg::conGetPt $_CN(5) -arc 1]
  gg::segEnd
set _CN(26) [gg::conEnd]
gg::conBegin
  gg::segBegin -type 3D_LINE
    gg::segAddControlPt [gg::conGetPt $_CN(8) -arc 0]
    gg::segAddControlPt [gg::conGetPt $_CN(7) -arc 0]
  gg::segEnd
set _CN(27) [gg::conEnd]
gg::conBegin
  gg::segBegin -type 3D_LINE
    gg::segAddControlPt [gg::conGetPt $_CN(8) -arc 1]
    gg::segAddControlPt [gg::conGetPt $_CN(7) -arc 1]
  gg::segEnd
set _CN(28) [gg::conEnd]
gg::dispSmallText FALSE
set _ggTemp_(1) [list 1.107 -7.52e-4 0]
gg::conBegin
  gg::segBegin -type 3D_LINE
    gg::segAddControlPt [gg::conGetPt $_CN(23) -arc 1]
    gg::segAddControlPt $_ggTemp_(1)
  gg::segEnd
set _CN(29) [gg::conEnd]
unset _ggTemp_(1)
set _ggTemp_(2) [list -0.1 0 0]
gg::conBegin
  gg::segBegin -type 3D_LINE
    gg::segAddControlPt [gg::conGetPt $_CN(1) -arc 1]
    gg::segAddControlPt $_ggTemp_(2)
  gg::segEnd
set _CN(30) [gg::conEnd]
unset _ggTemp_(2)
set _ggTemp_(1) [list 0.5 0.2638 0]
gg::conBegin
  gg::segBegin -type CONIC -rho 0.01
    gg::segAddControlPt [gg::conGetPt $_CN(30) -arc 1]
    gg::segAddControlPt [gg::conGetPt $_CN(29) -arc 1]
    gg::segAddControlPt $_ggTemp_(1)
  gg::segEnd
set _CN(31) [gg::conEnd]
unset _ggTemp_(1)
set _ggTemp_(1) [list 0.5 -0.2003 0]
```

156

```
gg::conBegin
  gg::segBegin -type CONIC -rho 0.01
    gg::segAddControlPt [gg::conGetPt $_CN(29) -arc 1]
    gg::segAddControlPt [gg::conGetPt $_CN(30) -arc 1]
    gg::segAddControlPt $_ggTemp_(1)
  gg::segEnd
set _CN(32) [gg::conEnd]
unset _ggTemp_(1)
set _CN(33) [gg::conSplit $_CN(31) [gg::conGetPt $_CN(31) -x 0.8356]]
set _CN(34) [gg::conSplit $_CN(33) [gg::conGetPt $_CN(33) -x 1.004]]
set _CN(35) [gg::conSplit $_CN(32) [gg::conGetPt $_CN(32) -x 0.8574]]
set _CN(36) [gg::conSplit $_CN(32) [gg::conGetPt $_CN(32) -x 0.9721]]
gg::conBegin
  gg::segBegin -type 3D_LINE
    gg::segAddControlPt [gg::conGetPt $_CN(1) -arc 0]
    gg::segAddControlPt [gg::conGetPt $_CN(31) -arc 1]
  gg::segEnd
set _CN(47) [gg::conEnd]
gg::conBegin
  gg::segBegin -type 3D_LINE
    gg::segAddControlPt [gg::conGetPt $_CN(4) -arc 0]
    gg::segAddControlPt [gg::conGetPt $_CN(33) -arc 1]
  gg::segEnd
set _CN(48) [gg::conEnd]
gg::conBegin
  gg::segBegin -type 3D_LINE
    gg::segAddControlPt [gg::conGetPt $_CN(3) -arc 1]
    gg::segAddControlPt [gg::conGetPt $_CN(35) -arc 0]
  gg::segEnd
set _CN(49) [gg::conEnd]
gg::conBegin
  gg::segBegin -type 3D_LINE
    gg::segAddControlPt [gg::conGetPt $_CN(10) -arc 1]
    gg::segAddControlPt [gg::conGetPt $_CN(32) -arc 1]
  gg::segEnd
set _CN(50) [gg::conEnd]
gg::conBegin
  gg::segBegin -type CONIC -rho 0.5
    gg::segAddControlPt [gg::conGetPt $_CN(10) -arc 1]
    gg::segAddControlPt [gg::conGetPt $_CN(4) -arc 0]
    gg::segAddControlPt [gg::conGetPt $_CN(23) -arc 1]
  gg::segEnd
set _CN(51) [gg::conEnd]
set _CN(52) [gg::conSplit $_CN(51) [gg::conGetPt $_CN(51) -arc 0.49249061616]]

#Create connectors needed for the LES and EULER regions
set _ggTemp_(1) [list 1 2.5 0]
set _ggTemp_(2) [list 6 2.5 0]
gg::conBegin
  gg::segBegin -type 3D_LINE
    gg::segAddControlPt $_ggTemp_(1)
    gg::segAddControlPt $_ggTemp_(2)
  gg::segEnd
set _CN(37) [gg::conEnd]
unset _ggTemp_(1)
unset _ggTemp_(2)
```

```
set _ggTemp_(3) [list 6 2 0]
gg::conBegin
  gg::segBegin -type 3D_LINE
    gg::segAddControlPt [gg::conGetPt $_CN(37) -arc 1]
    gg::segAddControlPt $_ggTemp_(3)
  gg::segEnd
set _CN(38) [gg::conEnd]
unset _ggTemp_(3)
set _ggTemp_(4) [list 6 -2 0]
gg::conBegin
  gg::segBegin -type 3D_LINE
    gg::segAddControlPt [gg::conGetPt $_CN(38) -arc 1]
    gg::segAddControlPt $_ggTemp_(4)
  gg::segEnd
set _CN(39) [gg::conEnd]
unset _ggTemp_(4)
set _ggTemp_(5) [list 6 -2.5 0]
gg::conBegin
  gg::segBegin -type 3D_LINE
    gg::segAddControlPt [gg::conGetPt $_CN(39) -arc 1]
    gg::segAddControlPt $_ggTemp_(5)
  gg::segEnd
set _CN(40) [gg::conEnd]
unset _ggTemp_(5)
set _ggTemp_(6) [list 1 -2.5 0]
gg::conBegin
  gg::segBegin -type 3D_LINE
    gg::segAddControlPt [gg::conGetPt $_CN(40) -arc 1]
    gg::segAddControlPt $_ggTemp_(6)
  gg::segEnd
set _CN(41) [gg::conEnd]
unset _ggTemp_(6)
set _ggTemp_(7) [list -1.5 0 0]
gg::conBegin
  gg::segBegin -type CIRCULAR_ARC
    gg::segAddControlPt [gg::conGetPt $_CN(41) -arc 1]
    gg::segAddControlPt [gg::conGetPt $_CN(37) -arc 0]
    gg::segAddControlPt $_ggTemp_(7)
  gg::segEnd
set _CN(42) [gg::conEnd]
unset _ggTemp_(7)
set _ggTemp_(1) [list 4 2 0]
gg::conBegin
  gg::segBegin -type 3D_LINE
    gg::segAddControlPt [gg::conGetPt $_CN(38) -arc 1]
    gg::segAddControlPt $_ggTemp_(1)
  gg::segEnd
set _CN(43) [gg::conEnd]
unset _ggTemp_(1)
set _ggTemp_(2) [list 4 -2 0]
gg::conBegin
  gg::segBegin -type 3D_LINE
    gg::segAddControlPt [gg::conGetPt $_CN(43) -arc 1]
    gg::segAddControlPt $_ggTemp_(2)
  gg::segEnd
set _CN(44) [gg::conEnd]
```

```
unset _ggTemp_(2)
gg::conBegin
  gg::segBegin -type 3D_LINE
    gg::segAddControlPt [gg::conGetPt $_CN(44) -arc 1]
    gg::segAddControlPt [gg::conGetPt $_CN(39) -arc 1]
  gg::segEnd
set _CN(45) [gg::conEnd]
set _ggTemp_(3) [list -0.172 0 0]
gg::conBegin
  gg::segBegin -type CONIC -rho 0.5
    gg::segAddControlPt [gg::conGetPt $_CN(43) -arc 1]
    gg::segAddControlPt [gg::conGetPt $_CN(44) -arc 1]
    gg::segAddControlPt $_ggTemp_(3)
  gg::segEnd
set _CN(46) [gg::conEnd]
unset _ggTemp_(3)
######################################################

#Set the number of nodes in the connectors
gg::conRedimBegin
  gg::conRedim $_CN(4) 50
  gg::conRedim $_CN(12) 20
  gg::conRedim $_CN(6) 25
  gg::conRedim $_CN(19) 25
  gg::conRedim $_CN(15) 29
  gg::conRedim $_CN(18) 25
  gg::conRedim $_CN(14) 15
  gg::conRedim $_CN(26) 15
  gg::conRedim $_CN(5) 25
  gg::conRedim $_CN(25) 15
  gg::conRedim $_CN(13) 10
  gg::conRedim $_CN(11) 50
  gg::conRedim $_CN(23) 43
  gg::conRedim $_CN(24) 43
  gg::conRedim $_CN(2) 50
  gg::conRedim $_CN(9) 10
  gg::conRedim $_CN(27) 15
  gg::conRedim $_CN(10) 20
  gg::conRedim $_CN(7) 25
  gg::conRedim $_CN(17) 15
  gg::conRedim $_CN(20) 25
  gg::conRedim $_CN(16) 29
  gg::conRedim $_CN(21) 25
  gg::conRedim $_CN(28) 15
  gg::conRedim $_CN(8) 25
  gg::conRedim $_CN(22) 50
  gg::conRedim $_CN(49) 75
  gg::conRedim $_CN(50) 75
  gg::conRedim $_CN(29) 75
  gg::conRedim $_CN(48) 75
  gg::conRedim $_CN(47) 75
  gg::conRedim $_CN(30) 75
  gg::conRedim $_CN(34) 50
  gg::conRedim $_CN(33) 50
  gg::conRedim $_CN(31) 80
  gg::conRedim $_CN(35) 80
```

159

```
  gg::conRedim $_CN(36) 50
  gg::conRedim $_CN(32) 50
  gg::conRedim $_CN(46) 1024
  gg::conRedim $_CN(44) 483
  gg::conRedim $_CN(43) 50
  gg::conRedim $_CN(45) 50
  gg::conRedim $_CN(39) 42
  gg::conRedim $_CN(38) 7
  gg::conRedim $_CN(40) 7
  gg::conRedim $_CN(41) 52
  gg::conRedim $_CN(37) 52
  gg::conRedim $_CN(42) 80
  gg::conRedim $_CN(51) 50
  gg::conRedim $_CN(52) 50
gg::conRedimEnd
#####################################################################

#Set the distribution of the nodes in each connector
#5e-5 corresponds to the first cell heigth in the SS of the airfoil.
gg::conBeginSpacing $_CN(4) -sub 1 5e-5
gg::conBeginSpacing $_CN(12) -sub 1 1e-4
gg::conEndSpacing $_CN(12) -sub 1 5e-5
gg::conBeginSpacing $_CN(6) -sub 1 5e-5
gg::conEndSpacing $_CN(6) -sub 1 5e-5
gg::dispSmallText FALSE
gg::conBeginSpacing $_CN(5) -sub 1 5e-5
gg::conEndSpacing $_CN(5) -sub 1 5e-5
gg::conEndSpacing $_CN(19) -sub 1 5e-5
gg::conEndSpacing $_CN(18) -sub 1 5e-5
gg::conBeginSpacing $_CN(15) -sub 1 5e-5
gg::conEndSpacing $_CN(15) -sub 1 5e-5
gg::conBeginSpacing $_CN(14) -sub 1 5e-5
gg::conEndSpacing $_CN(14) -sub 1 5e-5
gg::conBeginSpacing $_CN(26) -sub 1 5e-5
gg::conEndSpacing $_CN(26) -sub 1 5e-5
gg::dispSmallText FALSE
gg::conBeginSpacing $_CN(25) -sub 1 5e-5
gg::conEndSpacing $_CN(25) -sub 1 5e-5
gg::conBeginSpacing $_CN(13) -sub 1 5e-5
gg::conEndSpacing $_CN(13) -sub 1 5e-5
gg::conBeginSpacing $_CN(11) -sub 1 5e-5
gg::conEndSpacing $_CN(11) -sub 1 5e-5
gg::conBeginSpacing $_CN(52) -sub 1 5e-5
gg::conEndSpacing $_CN(52) -sub 1 5e-5
gg::conBeginSpacing $_CN(23) -sub 1 5e-5
gg::conEndSpacing $_CN(23) -sub 1 1e-3
gg::conBeginSpacing $_CN(24) -sub 1 5e-5
gg::conEndSpacing $_CN(24) -sub 1 1e-3
gg::conBeginSpacing $_CN(2) -sub 1 5e-5
gg::conEndSpacing $_CN(2) -sub 1 5e-5
gg::conBeginSpacing $_CN(51) -sub 1 5e-5
gg::conEndSpacing $_CN(51) -sub 1 5e-5
gg::conBeginSpacing $_CN(9) -sub 1 5e-5
gg::conEndSpacing $_CN(9) -sub 1 5e-5
gg::conBeginSpacing $_CN(7) -sub 1 5e-5
gg::conEndSpacing $_CN(7) -sub 1 5e-5
```

160

```
gg::conBeginSpacing $_CN(17) -sub 1 5e-5
gg::conEndSpacing $_CN(17) -sub 1 5e-5
gg::conBeginSpacing $_CN(20) -sub 1 5e-5
gg::conEndSpacing $_CN(21) -sub 1 5e-5
gg::conBeginSpacing $_CN(16) -sub 1 5e-5
gg::conEndSpacing $_CN(16) -sub 1 5e-5
gg::conBeginSpacing $_CN(8) -sub 1 5e-5
gg::conEndSpacing $_CN(8) -sub 1 5e-5
gg::conBeginSpacing $_CN(28) -sub 1 5e-5
gg::conEndSpacing $_CN(28) -sub 1 5e-5
gg::conBeginSpacing $_CN(27) -sub 1 5e-5
gg::conEndSpacing $_CN(27) -sub 1 5e-5
gg::conBeginSpacing $_CN(10) -sub 1 1e-4

#2e-5 corresponds to the first cell height in the PS of the airfoil.
gg::conEndSpacing $_CN(10) -sub 1 2e-5
gg::conEndSpacing $_CN(22) -sub 1 5e-5
gg::conBeginSpacing $_CN(29) -sub 1 7e-4
gg::conEndSpacing $_CN(29) -sub 1 7e-3
gg::conBeginSpacing $_CN(48) -sub 1 5e-5
gg::conEndSpacing $_CN(48) -sub 1 7e-3
gg::conBeginSpacing $_CN(47) -sub 1 5e-5
gg::conEndSpacing $_CN(47) -sub 1 7e-3
gg::conBeginSpacing $_CN(30) -sub 1 5e-5
gg::conEndSpacing $_CN(30) -sub 1 7e-3
gg::conBeginSpacing $_CN(49) -sub 1 2e-5
gg::conEndSpacing $_CN(49) -sub 1 7e-3
gg::conBeginSpacing $_CN(50) -sub 1 2e-5
gg::conEndSpacing $_CN(50) -sub 1 7e-3
gg::conBeginSpacing $_CN(31) -sub 1 5e-3
gg::conEndSpacing $_CN(31) -sub 1 1.5e-2
gg::conBeginSpacing $_CN(33) -sub 1 1.5e-2
gg::conEndSpacing $_CN(33) -sub 1 1e-3
gg::conBeginSpacing $_CN(34) -sub 1 1e-3
gg::conEndSpacing $_CN(34) -sub 1 2.6e-3
gg::conEndSpacing $_CN(32) -sub 1 1e-3
gg::conEndSpacing $_CN(32) -sub 1 1.5e-3
gg::conBeginSpacing $_CN(32) -sub 1 3.935e-3
gg::conEndSpacing $_CN(36) -sub 1 7e-3
gg::conBeginSpacing $_CN(36) -sub 1 1e-3
gg::conEndSpacing $_CN(35) -sub 1 5e-3
gg::conBeginSpacing $_CN(35) -sub 1 1e-2

#0.02 is the expected characteristic size of the mesh
#in the LES region i.e.\Delta_o
gg::conDim $_CN(46) -spacing 0.02
gg::conDim $_CN(44) -spacing 0.02
gg::conBeginSpacing $_CN(45) -sub 1 8e-3
gg::conEndSpacing $_CN(45) -sub 1 1e-1
gg::conEndSpacing $_CN(43) -sub 1 8e-3
gg::conBeginSpacing $_CN(43) -sub 1 1e-1
gg::conDim $_CN(42) -spacing 0.1
gg::conDim $_CN(37) -spacing 0.1
gg::conDim $_CN(38) -spacing 0.1
gg::conDim $_CN(39) -spacing 0.1
gg::conDim $_CN(40) -spacing 0.1
```

```
gg::conDim $_CN(41) -spacing 0.1

########################################################
#DOMAIN CREATION
#Create RANS region (structured) mesh
gg::domBegin -type STRUCTURED
  gg::edgeBegin
    gg::edgeAddCon $_CN(18)
  gg::edgeEnd
  gg::edgeBegin
    gg::edgeAddCon $_CN(14)
    gg::edgeAddCon $_CN(26)
  gg::edgeEnd
  gg::edgeBegin
    gg::edgeAddCon $_CN(19)
  gg::edgeEnd
  gg::edgeBegin
    gg::edgeAddCon $_CN(15)
  gg::edgeEnd
set _DM(1) [gg::domEnd]
gg::dispConGPS FALSE
gg::dispSmallText FALSE
gg::domBegin -type STRUCTURED
  gg::edgeBegin
    gg::edgeAddCon $_CN(5)
  gg::edgeEnd
  gg::edgeBegin
    gg::edgeAddCon $_CN(25)
  gg::edgeEnd
  gg::edgeBegin
    gg::edgeAddCon $_CN(6)
  gg::edgeEnd
  gg::edgeBegin
    gg::edgeAddCon $_CN(26)
  gg::edgeEnd
set _DM(2) [gg::domEnd]
gg::domBegin -type STRUCTURED
  gg::edgeBegin
    gg::edgeAddCon $_CN(11)
  gg::edgeEnd
  gg::edgeBegin
    gg::edgeAddCon $_CN(13)
    gg::edgeAddCon $_CN(25)
    gg::edgeAddCon $_CN(12)
  gg::edgeEnd
  gg::edgeBegin
    gg::edgeAddCon $_CN(52)
  gg::edgeEnd
  gg::edgeBegin
    gg::edgeAddCon $_CN(23)
  gg::edgeEnd
set _DM(3) [gg::domEnd]
gg::domBegin -type STRUCTURED
  gg::edgeBegin
    gg::edgeAddCon $_CN(24)
  gg::edgeEnd
```

162

```
  gg::edgeBegin
    gg::edgeAddCon $_CN(51)
  gg::edgeEnd
  gg::edgeBegin
    gg::edgeAddCon $_CN(10)
    gg::edgeAddCon $_CN(27)
    gg::edgeAddCon $_CN(9)
  gg::edgeEnd
  gg::edgeBegin
    gg::edgeAddCon $_CN(2)
  gg::edgeEnd
set _DM(4) [gg::domEnd]
gg::domBegin -type STRUCTURED
  gg::edgeBegin
    gg::edgeAddCon $_CN(7)
  gg::edgeEnd
  gg::edgeBegin
    gg::edgeAddCon $_CN(28)
  gg::edgeEnd
  gg::edgeBegin
    gg::edgeAddCon $_CN(8)
  gg::edgeEnd
  gg::edgeBegin
    gg::edgeAddCon $_CN(27)
  gg::edgeEnd
set _DM(5) [gg::domEnd]
gg::domBegin -type STRUCTURED
  gg::edgeBegin
    gg::edgeAddCon $_CN(28)
    gg::edgeAddCon $_CN(17)
  gg::edgeEnd
  gg::edgeBegin
    gg::edgeAddCon $_CN(20)
  gg::edgeEnd
  gg::edgeBegin
    gg::edgeAddCon $_CN(16)
  gg::edgeEnd
  gg::edgeBegin
    gg::edgeAddCon $_CN(21)
  gg::edgeEnd
set _DM(6) [gg::domEnd]
gg::domBegin -type STRUCTURED
  gg::edgeBegin
    gg::edgeAddCon $_CN(29)
  gg::edgeEnd
  gg::edgeBegin
    gg::edgeAddCon $_CN(34)
  gg::edgeEnd
  gg::edgeBegin
    gg::edgeAddCon $_CN(48)
  gg::edgeEnd
  gg::edgeBegin
    gg::edgeAddCon $_CN(52)
  gg::edgeEnd
set _DM(7) [gg::domEnd]
gg::domBegin -type STRUCTURED
```

163

```
    gg::edgeBegin
       gg::edgeAddCon $_CN(4)
    gg::edgeEnd
    gg::edgeBegin
       gg::edgeAddCon $_CN(47)
    gg::edgeEnd
    gg::edgeBegin
       gg::edgeAddCon $_CN(33)
    gg::edgeEnd
    gg::edgeBegin
       gg::edgeAddCon $_CN(48)
    gg::edgeEnd
set _DM(8) [gg::domEnd]
gg::domBegin -type STRUCTURED
    gg::edgeBegin
       gg::edgeAddCon $_CN(1)
    gg::edgeEnd
    gg::edgeBegin
       gg::edgeAddCon $_CN(30)
    gg::edgeEnd
    gg::edgeBegin
       gg::edgeAddCon $_CN(31)
    gg::edgeEnd
    gg::edgeBegin
       gg::edgeAddCon $_CN(47)
    gg::edgeEnd
set _DM(9) [gg::domEnd]
gg::domBegin -type STRUCTURED
    gg::edgeBegin
       gg::edgeAddCon $_CN(3)
    gg::edgeEnd
    gg::edgeBegin
       gg::edgeAddCon $_CN(49)
    gg::edgeEnd
    gg::edgeBegin
       gg::edgeAddCon $_CN(35)
    gg::edgeEnd
    gg::edgeBegin
       gg::edgeAddCon $_CN(30)
    gg::edgeEnd
set _DM(10) [gg::domEnd]
gg::domBegin -type STRUCTURED
    gg::edgeBegin
       gg::edgeAddCon $_CN(49)
    gg::edgeEnd
    gg::edgeBegin
       gg::edgeAddCon $_CN(36)
    gg::edgeEnd
    gg::edgeBegin
       gg::edgeAddCon $_CN(50)
    gg::edgeEnd
    gg::edgeBegin
       gg::edgeAddCon $_CN(22)
    gg::edgeEnd
set _DM(11) [gg::domEnd]
gg::domBegin -type STRUCTURED
```

```
  gg::edgeBegin
    gg::edgeAddCon $_CN(50)
  gg::edgeEnd
  gg::edgeBegin
    gg::edgeAddCon $_CN(32)
  gg::edgeEnd
  gg::edgeBegin
    gg::edgeAddCon $_CN(29)
  gg::edgeEnd
  gg::edgeBegin
    gg::edgeAddCon $_CN(51)
  gg::edgeEnd
set _DM(12) [gg::domEnd]

#Create the LES region (unstructured) mesh
gg::domBegin -type UNSTRUCTURED
  gg::edgeBegin
    gg::edgeAddCon $_CN(46)
    gg::edgeAddCon $_CN(44)
    gg::edgeReorient
  gg::edgeEnd
  gg::edgeBegin
    gg::edgeAddCon $_CN(35)
    gg::edgeAddCon $_CN(31)
    gg::edgeAddCon $_CN(33)
    gg::edgeAddCon $_CN(34)
    gg::edgeAddCon $_CN(32)
    gg::edgeAddCon $_CN(36)
  gg::edgeEnd
set _DM(13) [gg::domEnd]
gg::domBegin -type UNSTRUCTURED
  gg::edgeBegin
    gg::edgeAddCon $_CN(45)
    gg::edgeAddCon $_CN(39)
    gg::edgeAddCon $_CN(43)
    gg::edgeAddCon $_CN(44)
  gg::edgeEnd
set _DM(14) [gg::domEnd]
gg::domBegin -type UNSTRUCTURED
  gg::edgeBegin
    gg::edgeAddCon $_CN(41)
    gg::edgeAddCon $_CN(40)
    gg::edgeAddCon $_CN(45)
    gg::edgeAddCon $_CN(46)
    gg::edgeAddCon $_CN(43)
    gg::edgeAddCon $_CN(38)
    gg::edgeAddCon $_CN(37)
    gg::edgeAddCon $_CN(42)
  gg::edgeEnd
set _DM(15) [gg::domEnd]
set _ggTemp_(1) [list $_DM(14)]
gg::domUnsSolverBegin $_ggTemp_(1)
  gg::domUnsSolverAtt $_DM(14) -boundary_decay 0.92
  gg::domUnsSolverRun REFINE
gg::domUnsSolverEnd
unset _ggTemp_(1)
```

165

```
##########################################################

#Create blocks by extrusion of the domains.
gg::blkExtrusionBegin [list \
    $_DM(1) \
    $_DM(2) \
    $_DM(3) \
    $_DM(4) \
    $_DM(5) \
    $_DM(6) \
    $_DM(7) \
    $_DM(8) \
    $_DM(9) \
    $_DM(10) \
    $_DM(11) \
    $_DM(12) \
    $_DM(13) \
    $_DM(14) \
    $_DM(15) \
  ]  -default HYPERBOLIC
  gg::blkExtrusionMode TRANSLATE
  gg::blkExtrusionAtt -distance 1
  gg::blkExtrusionAtt -direction [list 0 0 1]

  #50 is the number of nodes in the spanwise direction.
  #If 2D the set the number of steps to 1.
  gg::blkExtrusionStep 50
set _ggTemp_(1) [gg::blkExtrusionEnd]
set _BL(1) [lindex $_ggTemp_(1) 0]
set _BL(2) [lindex $_ggTemp_(1) 1]
set _BL(3) [lindex $_ggTemp_(1) 2]
set _BL(4) [lindex $_ggTemp_(1) 3]
set _BL(5) [lindex $_ggTemp_(1) 4]
set _BL(6) [lindex $_ggTemp_(1) 5]
set _BL(7) [lindex $_ggTemp_(1) 6]
set _BL(8) [lindex $_ggTemp_(1) 7]
set _BL(9) [lindex $_ggTemp_(1) 8]
set _BL(10) [lindex $_ggTemp_(1) 9]
set _BL(11) [lindex $_ggTemp_(1) 10]
set _BL(12) [lindex $_ggTemp_(1) 11]
set _BL(13) [lindex $_ggTemp_(1) 12]
unset _ggTemp_(1)
```

Appendix C

RSSJ model numerical parameters (NACA 4415)

The sources used in the simplified RSSJ model follow the numeration given in figure 4.34. Sources 1 defines the u'u' component; Sources 4 and 5 define the u'v' component and source 6 defines the v'v' component. JS stands for Jet Strength and it indicates a fraction of the full actuation.

SUCTION SIDE

α \ JS	1/4	1/2	3/4	1
$-6°$	0.065	0.32	0.82	1.5
$0°$	0.06	0.3	0.77	1.4
$6°$	0.04	0.21	0.55	1.0
PRESSURE SIDE				
$-6°$	0.043	0.21	0.55	1.0
$0°$	0.035	0.17	0.44	0.8
$6°$	0.031	0.15	0.38	0.7

Table C.1: Strength of source 1 (Γ_1)

α \ JS	All levels SS	All levels PS
$-6°$	-0.3	-0.4
$0°$	-0.2	-0.1
$6°$	0.0	0.15

Table C.2: Angle of source 1 (θ_1) in radians

167

	λ_1	ω_1	X_1	Y_1
SS	1×10^5	5×10^6	0.97	0.026
PS	1×10^5	5×10^6	0.967	-0.018

Table C.3: Unaltered parameters of source 1

JS α	1/4	1/2	3/4	1
$-6°$ to $6°$ (SS)	0.01	0.03	0.06	0.09
$-6°$ to $6°$ (PS)	-0.004	-0.033	-0.1	-0.2

Table C.4: Strength of source 4 (Γ_4)

	θ_4	λ_4	ω_4	X_4	Y_4
SS	-0.2	1×10^6	1×10^8	0.974	0.0263
PS	0.0	2×10^5	8×10^5	0.971	-0.0187

Table C.5: Unaltered parameters of source 4

JS α	1/4	1/2	3/4	1
$-6°$ to $6°$ (SS)	-0.007	-0.051	-0.17	-0.3
$-6°$ to $6°$ (PS)	0.008	0.02	0.04	0.07

Table C.6: Strength of source 5 (Γ_5)

	θ_5	λ_5	ω_5	X_5	Y_5
SS	-0.2	1×10^6	5×10^8	0.971	0.026
PS	0.0	2×10^5	8×10^5	0.9675	-0.0178

Table C.7: Unaltered parameters of source 5

SUCTION SIDE

JS α	1/4	1/2	3/4	1
$-6°$	0.013	0.06	0.16	0.3
$0°$	0.011	0.05	0.13	0.25
$6°$	0.004	0.02	0.05	0.1

PRESSURE SIDE

$-6°$	0.01	0.05	0.14	0.26
$0°$	0.009	0.04	0.12	0.22
$6°$	0.008	0.03	0.1	0.18

Table C.8: Strength of source 6 (Γ_6)

JS α	All levels SS and PS
$-6°$	2×10^4
$0°$	5×10^4
$6°$	8×10^4

Table C.9: Size control parameter of source 6 (λ_6)

JS α	All levels SS and PS
$-6°$	6×10^5
$0°$	8×10^5
$6°$	1×10^6

Table C.10: Size control parameter of source 6 (ω_6)

	θ_6	X_6	Y_6
SS	0.0	0.974	0.027
PS	-0.2	.971	-0.019

Table C.11: Unaltered parameters of source 6

169

Appendix D

RSSJ model radial basis function interpolation weights (NACA 4415)

	$\Gamma_1 \times 10^{-9}$	$\theta_1 \times 10^{-10}$	$\Gamma_4 \times 10^{-6}$	$\Gamma_5 \times 10^{-5}$	$\Gamma_6 \times 10^{-9}$	$\lambda_6 \times 10^{-15}$	$\omega_6 \times 10^{-16}$
W_1	-0.98226	0.30637	0.50022	-0.33974	-0.44979	0.57380	0.38253
W_2	1.72840	-0.53907	-0.87976	0.59752	0.79147	-1.00956	-0.67305
W_3	-0.74642	0.23278	0.38000	-0.25809	-0.34181	0.43593	0.29062
W_4	-1.01703	0.31528	0.51733	-0.3541	-0.46937	0.59437	0.39625
W_5	1.68148	-0.52123	-0.85500	0.59235	0.77604	-0.98257	-0.65505
W_6	-0.66474	0.20603	0.33813	-0.23426	-0.30680	0.38836	0.25891
W_7	-4.57624	1.43375	2.36674	-1.64811	-2.10923	2.69606	1.79738
W_8	8.81842	-2.76265	-4.55846	3.17435	4.06455	-5.19462	-3.46311
W_9	-4.24368	1.32937	2.19418	-1.52795	-1.9560	2.49945	1.66631
W_{10}	3.35062	-1.04872	-1.72436	1.8814	1.5399	-1.96850	-1.31234
W_{11}	-5.93032	1.85605	3.05045	-2.10185	-2.7256	3.48370	2.32248
W_{12}	2.58074	-0.80765	-1.32777	0.91488	1.18616	-1.51580	-1.01054
W_{13}	3.61669	-1.13004	-1.86499	1.3033	1.66957	-2.12811	-1.41875
W_{14}	-6.10887	1.90860	3.14880	-2.20045	-2.82007	3.59411	2.39608
W_{15}	2.493215	-0.77888	-1.28549	0.89833	1.15097	-1.46660	-0.97774

Table D.1: Radial basis function interpolation weights for the suction side actuator

	$\Gamma_1 \times 10^{-10}$	$\theta_1 \times 10^{-10}$	$\Gamma_4 \times 10^{-5}$	$\Gamma_5 \times 10^{-5}$	$\Gamma_6 \times 10^{-9}$	$\lambda_6 \times 10^{-16}$	$\omega_6 \times 10^{-16}$
W_1	0.14243	-0.63793	0.36477	-0.31456	0.51411	-0.08006	-0.53374
W_2	-0.40321	1.80623	-1.03254	0.89043	-1.45549	0.226685	1.51122
W_3	0.26082	-1.16846	0.66807	-0.57612	0.94151	-0.14664	-0.97762
W_4	0.21959	-0.85408	0.20777	-0.40110	0.75118	-0.10682	-0.71213
W_5	-0.45368	1.76473	-0.42916	0.81849	-1.55197	0.22071	1.47141
W_6	0.23413	-0.91082	0.22152	-0.42764	0.80094	-0.11391	-0.75942
W_7	0.73797	-3.08473	1.42544	-1.52333	2.60337	-0.38669	-2.57796
W_8	-2.11504	8.84219	-4.08463	4.36513	-7.46151	1.10843	7.38950
W_9	1.37728	-5.75837	2.66048	-2.84319	4.85891	-0.72185	-4.81230
W_{10}	-0.51154	2.21441	-1.16857	1.09702	-1.82687	0.27779	1.85195
W_{11}	1.55577	-6.73583	3.55359	-3.33598	5.55634	-0.84499	-5.63324
W_{12}	-1.04437	4.52204	-2.38603	2.23992	-3.72998	0.56727	3.78181
W_{13}	-0.62381	2.51604	-0.92955	1.22328	-2.16953	0.31509	2.10061
W_{14}	1.66519	-6.71724	2.48085	-3.26481	5.79151	-0.84121	-5.60807
W_{15}	-1.04154	4.20182	-1.55202	2.01216	-3.62252	0.52620	3.50799

Table D.2: Radial basis function interpolation weights for the pressure side actuator

Appendix E

RSSJ model numerical parameters (Dragon Eye)

The sources used in the simplified RSSJ model follow the numeration given in figure 4.34. Sources 1 defines the u'u' component; Sources 4 and 5 define the u'v' component and source 6 defines the v'v' component. This model was calibrated for full actuation only.

SUCTION SIDE

α	Γ_1	θ_1	λ_1	ω_1	X_1	Y_1
$-2°$	0.98	-0.25	1×10^5	5×10^6	0.966	0.023
$0°$	0.9	-0.2	1×10^5	5×10^6	0.966	0.023
$6°$	0.7	-0.1	1×10^5	5×10^6	0.966	0.023

PRESSURE SIDE

$-2°$	0.5	0.05	1×10^5	5×10^6	0.9675	-0.02
$0°$	0.6	0.1	1×10^5	5×10^6	0.9675	-0.02
$6°$	0.9	0.2	1×10^5	5×10^6	0.9675	-0.02

Table E.1: Parameters for source 1

	Γ_4	θ_4	λ_4	ω_4	X_4	Y_4
SS	-0.25	-0.2	1×10^6	1×10^7	0.967	0.023
PS	0.2	0.0	2×10^5	8×10^5	0.967	-0.0198

Table E.2: Parameters for source 4 for all α

	Γ_5	θ_5	λ_5	ω_5	X_5	Y_5
SS	0.08	-0.2	1×10^6	1×10^8	0.97	0.0236
PS	-0.1	0.1	1×10^7	1×10^7	0.97	-0.0204

Table E.3: Parameters for source 5 for all α

SUCTION SIDE

α	Γ_6	θ_6	λ_6	ω_6	X_6	Y_6
$-2°$	0.19	0.0	4×10^4	7.5×10^5	0.971	0.024
$0°$	0.18	0.0	5×10^4	8×10^5	0.971	0.024
$6°$	0.14	0.0	7×10^4	9×10^5	0.971	0.024

PRESSURE SIDE

$-2°$	0.11	0.0	4×10^4	7.5×10^5	0.971	-0.02
$0°$	0.12	0.0	5×10^4	8×10^5	0.971	-0.02
$6°$	0.15	0.0	7×10^4	9×10^5	0.971	-0.02

Table E.4: Parameters for source 6

Bibliography

[1] I. Abbott and A. Von Doenhoff. *Theory of wing sections*. Dover Publications, 1949.

[2] I. Abbott, A. Von Doenhoff, and L. Stivers. Summary of airfoil data. Technical Report 824, NACA, 1945. p. 400.

[3] M. Amitay, V. Kibens, D. Parekh, and A. Glezer. The dynamics of flow reattachment over a thick airfoil controlled by a synthetic jet actuator. *AIAA paper 99-1001*, 1999.

[4] M. Amitay, D. Smith, V Kibens, D. Parekh, and A. Glezer. Aerodynamic flow control over an unconventional airfoil using synthetic jets actuators. *AIAA journal*, 39:361–370, 2001.

[5] J. Baker, C. Van Dam, and B. Gilbert. Flatback airfoil wind tunnel experiments. Technical Report SAND2008-2008, Sandia National Lab, 2008.

[6] B. Baldwin and H. Lomax. Thin layer approximation and algebraic model for separated turbulent flows. *AIAA paper 78-257*, 1978.

[7] J. Barrow, W. Rae, and A. Pope. *Low-Speed Wind tunnel testing*. John Wiley and Sons, 1999.

174

[8] T. Barth, J. Jerspensen, and C. Dennis. The design and application of upwind schemes on unstructured meshes. In *AIAA 27th Aerospace sciences meeting*, 1989. AIAA-1989-366.

[9] G. Ben-Dov, A. Pearlstein, D. Brzozowski, and A. Glezer. Low-order modeling of airfoil pitch control effected by trapped vorticity concentrations. In *Bulletin of the American Physical Society - APS DFD 2008*, 2008.

[10] N. Beratlis and M. Smith. Optimization of synthetic jet cooling for microelectronics applications. In *Annual IEEE semiconductor thermal measurement and management symposium*, pages 66–73, 2003.

[11] P. Bernard and J. Wallace. *Turbulent Flows. Analysis, measurement and prediction*. John Wiley and sons, 2003.

[12] A. Braslow. *A history of suction-type laminar-flow control with emphasis on flight research*. NASA, 1999.

[13] M. Breuer and N. Jovicic. Separated flow around a flat plate at high incidence: an les investigation. *Journal of turbulence*, 2:01–15, 2001.

[14] M. Breuer, N. Jovicic, and K. Mazaev. Comparison of des, rans and les for the separated flow around a flat plate at high incidence. *International Journal for Numerical Methods in Fluids*, 41:357–388, 2003.

[15] D. Brzozowski and A.Glezer. Transient separation control using pulse-combustion actuation. *AIAA-2002-3166*, 2002.

[16] D. Brzozowski, J. Culp, and A. Glezer. Airfoil pitch control using trapped vorticity concentrations. In *Bulletin of the American Physical Society-APS DFD 2007*, 2007.

[17] D. Brzozowski, J. Culp, A. Kutay, J. Muse, and A. Glezer. Closed-loop aerodynamic flow control of a free airfoil. In *AIAA 4th flow control conference*, 2008. AIAA-2008-4323.

[18] U. Bunge, C. Mockett, and F. Thiele. Guidelines for implementing detached-eddy simulation using different models. *Aerospace science and technology*, 11:376–385, 2007.

[19] T. Cebeci and P. Bradshaw. *Momentum transfer in boundary layers*. McGraw Hill, 1977.

[20] T. Cebeci and J. Cousteix. *Modeling and Computation of boundary-layer flows*. Springer, 2005.

[21] T. Cebeci, M. Platzer, H. Chen, K. Chang, and J. Shiao. *Analysis of low-speed unsteady airfoil flows*. Springer, 2005.

[22] T. Cebeci, J. Shao, F. Kafyeke, and E. Laurendeau. *Computational Fluid Dynamics for engineers*. Springer, 2005.

[23] Y. Chen, S. Liang, K. Aung, A. Glezer, and J. Jagoda. Enhanced mixing in a simulated combustor using synthetic jet actuators. *AIAA paper 99-0449*, 1999.

[24] H. Choi, P. Moin, and J. Kim. Direct numerical simulation of turbulent flow over riblets. *Journal of fluid mechanics*, 255:503–539, 1993.

[25] H. Choi, P. Moin, and J. Kim. Active turbulence control for drag reduction in wall bounded flows. *Journal of fluid mechanics*, 262:75–110, 1994.

[26] A. Chorin. Numerical solution of the navier-stokes equations. *Mathematics of computation*, 22:745–762, 1968.

[27] H. Coanda. Propelling device, 1938.

[28] A. Crook, M. Sadri, and N. Wood. The development and implementation of synthetic jets for control of separated flow. *AIAA paper 99-3176*, 1999.

[29] L. Davidson and S.Peng. Hybrid les-rans modelling: A one-equation sgs model combined with a $\kappa - \omega$ model for predicting recirculating flows. *International Journal for Numerical Methods in Fluids*, 43:1003–1018, 2003.

[30] S. Deck. Zonal-detached-eddy simulation of the flow around a high-lift configuration. *AIAA journal*, 43:2372–2384, 2005.

[31] S. Deck. Delayed detached-eddy simulation of self sustained unsteadiness and side-loads in an over expanded nozzle. submitted to shock waves, 2008.

[32] S. Deck, P. Duveau, P. d'Espiney, and P. Guillen. Development and application of spalart-allmaras one equation turbulence model to three-dimensional supersonic complex configurations. *Aerospace science and technology*, 6:171–183, 2002.

[33] H. Van der Vorst. Bi-cgstab: A fast and smoothly converging variant of bi-cg for the solution of nonsymmetric linear systems. *SIAM Journal on Scientific Computing (SISC)*, 13:631–644, 1992.

[34] M. DeSalvo. Private communication, 2008. Georgia Tech Research Institute.

[35] M. DeSalvo, M. Amitay, and A. Glezer. Modification of the aerodynamic performance of airfoil at low angle of attack: Trailing edge trapped vortices. *AIAA paper 2002-3165*, 2002.

[36] M. DeSalvo and A. Glezer. Airfoil aerodynamic performance modification using hybrid surface actuators. In *AIAA 43th Aerospace sciences meeting and exhibit*, 2005. AIAA-2005-0872.

[37] M. DeSalvo and A. Glezer. Control of airfoil aerodynamic performance using distributed trapped vorticity. In *AIAA 45th Aerospace sciences meeting and exhibit*, 2007. AIAA-2007-708.

[38] M.E. DeSalvo and A. Glezer. Aerodynamic performance modification at low angles of attack by trailing edge vortices. In *2nd AIAA flow control conference*, 2004. AIAA-2004-2118.

[39] J. Donovan and M. Selig. Low reynolds number airfoil design and wind tunnel testing at princeton university. In *Low Reynolds number aerodynamics*, volume 54, pages 39–57, 1989.

[40] S. Eisenbach and R. Friedrich. Les of the flow around an airfoil at $re = 1x10^5$ and high angle of attack using cartesian grids. *Theoretical and computational fluid dynamics*, 22:213–225, 2008.

[41] R. Englar and G. Huson. Development of advanced circulation control wing lift airfoils. *AIAA paper 83-1847*, 1983.

[42] R. Englar, M. Smith, M. Kelley, and R. Rover. Development of circulation control technology for application to advanced subsonic aircrafts. *AIAA paper 93-0644*, 1993.

[43] J. Forsythe, W. Strang, and K. Squires. Six degree of freedom computation of the f-15e entering a spin. In *AIAA 44th Aerospace science meeting and exhibition*, 2006. AIAA-2006-0858.

[44] M. Gad-El-Hak. *Flow Control: Passive, Active, and Reactive Flow Management*. Cambridge University press, 2007.

[45] M. Gad-El-Hak, A. Polland, and J. Bonnet. *Flow Control: Fundamentals and practices*. Springer, 1998.

[46] Q. Gallas, R. Holman, T. Nishida, B. Carroll, M. Sheplak, and L. Cattafesta. Lumped element modeling of piezoelectric-driven synthetic jet actuators. *AIAA journal*, 41, 2003.

[47] H. Glauert. *The elements of aerofoil and airscrew theory*. Cambridge University Press, 1947.

[48] A. Glezer, M. Allen, D. Coe, B. Smith, M. Trautman, and J. Wiltse. Synthetic jet actuator and applications thereof, 1998.

[49] A. Glezer, M. Amitay, and A. Honohan. Aspects of low and high frequency actuation for aerodynamic flow control. *AIAA journal*, 43:1501–1511, 2005.

[50] A. Gross and H. Fasel. Cfd for investigating active flow control. In *AIAA 4th flow control conference*, 2008. AIAA-2008-4310.

[51] F. Ham. Cdp user documentation v2.3. 2005.

[52] F. Ham and G. Iaccarino. Energy conservation in collocated discretization schemes on unstructured meshes. Technical report, Center for Turbulent Research, Stanford University, 2004.

[53] F. Ham, G. Iaccarino, S. Apte, X. Wu, M. Herrmann, G. Contasntinescu, K. Mahesh, and P. Moin. Unstructured les of reacting multiphase flows in realistic gas turbine combustors. Technical report, Center for Turbulent Research, Stanford University, 2003.

[54] F. Harlow and B. Daly. Transport equations in turbulence. *Physics of fluids*, 13:2634–2649, 1970.

[55] F. Harlow and P. Nakayama. Transport of turbulence energy decay rate. Technical Report Los Alamos Scientific Laboratory report LA-3854, LANL, 1968.

[56] F. Harlow and J. Welch. Numerical calculation of time-dependent viscous incompressible flow of fluid with free surface. *Physics of fluid*, 8:2182–2189, 1965.

[57] J. Hefner and D. Bushnell. *Viscous drag reduction in boundary layers*, volume 123 of *Progress in astronautics and aeronautics*. American institute of aeronautics and astronautics, 1990.

[58] J. Hefner, L. Weinstein, and D. Bushnell. Large-eddy break-up scheme for turbulent drag reduction. In *AIAA Prog. Astro. Aero.*, volume 72, pages 447–463, 1979.

[59] R. Holman, Y. Utturkar, R. Mittal, B. Smith, and L. Cattafesta. Formation criterion for synthetic jets. *AIAA journal*, 43:2110–2116, 2005.

[60] G.R. Hough. *Viscous flow drag reduction*. AIAA, 1980.

[61] L. Huang, P. G. Huang, R. P. LeBeau, and T. Hauser. Numerical study of blowing and suction control mechanism on naca0012 airfoil. *Journal of Aircraft*, 41:1005–1013, 2004.

[62] G. Iaccarino and F. Ham. Automatic mesh generation for les in complex geometries. Technical report, Center for Turbulent Research, Stanford University, 2005.

[63] U. Ingard. On the theory and design of acoustic resonators. *The journal of the acoustical society of America*, 25:1037–1061, 1953.

[64] E. Jacobs and R. Anderson. Large-scale aerodynamic characteristics of airfoils as tested in the variable density wind tunnel. Technical Report 352, NACA, 1931.

[65] E. Jacobs, K. Ward, and R. Pinkerton. The characteristics of 78 related airfoil sections from tests in the variable density wind tunnel. Technical Report 460, NACA, 1968.

[66] S. Jee, O. Lopez, J. Muse, A. Calise, and R. Moser. Unsteady flow simulation of a controlled airfoil. In *Bulletin of the American Physical Society - APS DFD 2008*, 2008.

[67] I. Jollife. *Principal Component Analysis*. Springer, 2002.

[68] R. Joslin and G. Jones. *Applications of circulation control technology*, volume 214 of *Progress in astronautics and aeronautics*. American institute of aeronautics and astronautics, 2006.

[69] N. Jovicic and M. Breuer. *High Performance Computing in Science and Engineering Munich 2004 - separated flow past an airfoil at high angles of attack*. Springer, 2004.

[70] G. Karypis and V. Kumar. Parmetis: Parallel graph partitioning and sparse matrix ordering library. Technical Report 97-060, Department of Computer Science, Univ. of Minnesota, 1997.

[71] V. Katam, R. LeBeau Jr, and J. Jacob. Experimental and computational investigation of a modified naca4415 in low-re flows. In *22nd Applied Aerodynamics Conference and Exhibit*, 2004. AIAA-2004-4972.

[72] D. Kim and H. Choi. Immersed boundary method for flow around an arbitrarily moving body. *Journal of Computational Physics*, 212:662–680, 2005.

[73] L. Kral, J. Donovan, A. Cain, and A. Cary. Numerical simulation of synthetic jet actuators. *AIAA paper 97-1824*, 1997.

[74] A. Kutay, J. Culp, J. Muse, D. Brzozowski, A. Glezer, and A. Calise. A closed-loop flight control experiment using active flow control actuators. In *45th AIAA Aerospace Sciences Meeting and Exhibit*, 2007. AIAA-2007-0114.

[75] A. Kutay, J. Muse, and A. Calise. A 1-dof wind tunnel experiment in adaptive flow control. In *AIAA Guidance, Navigation, and Control Conference and Exhibit*, 2006. AIAA-2006-6430.

[76] E. Lorin, A. Hajlai, and A Soulaimani. An accurate positivity preserving scheme for the spalart-allmaras turbulence model. application to aerodynamics. In *36th AIAA Fluid Dynamics conference and exhibit*, 2006. AIAA-2006-3743.

[77] K. Mahesh, G. Constantinescu, and P. Moin. A numerical method for large-eddy simulation in complex geometries. *Journal of Computational Physics*, 197:215–240, 2004.

[78] E. Maskell. *A Theory of the Blockage Effects on Bluff Bodies and Stalled Wings in a Closed Wind Tunnel*. Aeronautical Research Council, 1965.

[79] R. McCallen, F. Browand, and J. Ross. *The aerodynamics of heavy vehicles: trucks, buses and trains*. Springer, 2004.

[80] F. Mendoca, R. Allen, J. de Charentenay, and M. Lewis. Towards understanding les and des for industrial aeroacoustic predictions. In *International Workshop on LES for Acoustics*, 2006.

[81] R. Michel. Etude de la transition sur les profiles d'aile. Technical Report Report 1/1578A, ONERA, 1951.

[82] R. Von Mises. *Theory of Flight*. Dover Publications, 1959.

[83] R. Mittal and L. Cattafesta. Actuator flow physics and its implication for cfd modeling of znmf jet based separation control. In *AIAA 4th flow control conference*, 2008.

[84] R. Mittal and P. Moin. Suitability of upwind biased schemes for large-eddy simulation. *AIAA journal*, 30:1415–1417, 1997.

[85] P. Moin and S. Apte. Large-eddy simulation of realistic gas turbine combustors. In *42nd AIAA Aerospace Sciences Meeting and Exhibit*, 2004. AIAA-2004-330.

[86] P. Moin and J. Kim. Application of a fractional-step method to incompressible navier-stokes equations. *Journal of Computational Physics*, 59:308–323, 1985.

[87] J. Moran. *An introduction to theoretical and computational aerodynamics.* John Wiley and Sons, 1984.

[88] Y. Morishini, T. Lund, O. Vasilyev, and P. Moin. Fully conservative higher order finite difference schemes for incompressible flow. *Journal of Computational Physics*, 143:90–124, 1998.

[89] J. Muse, A. Kutay, D. Brzozowski, D. Calise, and A. Glezer. Dynamic flight maneuvering using trapped vorticity flow control. In *AIAA 46th Aerospace Sciences Meeting and Exhibit*, 2008. AIAA-2008-0522.

[90] D. Parekh, S. Williams, M. Amitay, A. Glezer, A. Washburn, I. Gregory, and R. Scott. Active flow control on the stingray uav: Aerodynamic forces and moments. In *33rd Fluid dynamics conference and exhibit*, 2003. AIAA-2003-4002.

[91] S. Peng. Towards detached eddy simulation modelling using a k-equation turbulence model. In *ECCOMAS CFD*, 2006.

[92] B. Perot. Conservative properties of unstructured staggered mesh schemes. *Journal of Computational Physics*, 175:764–791, 2002.

[93] L. Prandtl. Uber flussigkeitsbewegung bei sehr kleiner reibung. In *Third International Mathematical Congress at Heidelberg*, 1904.

[94] L. Prandtl. Applications of modern hydrodynamics to aeronautics. Technical Report 116, NACA, 1921.

[95] W. Press, S. Teukolsky, W. Vetterling, and B. Flannery. *Numerical recipes: the art of scientific computing*. Cambridge University Press, 2007.

[96] V. Przulj and B. Basara. Bounded convection schemes for unstructured grids. In *AIAA 15th Computational fluid dynamics conference*, 2001. AIAA-2001-2593.

[97] P. Purser and H. Johnson. Effects of trailing-edge modifications on pitching-moment characteristics of airfoils. Technical Report NACA WR CB L4130 (L664), NACA, 1944.

[98] J. Riou, E. Garnier, and C. Basdevant. Study of the separated flow over a moderately swept missile fin in transonic regime. In *AIAA 38th fluid dynamics conference and exhibit*, 2008. AIAA-2008-4304.

[99] J. Riou, E. Garnier, S. Deck, and C. Basdevant. An extension of ddes to the computation of a generic missile fin in transonic regime. In *7th International Symposium on Engineering Turbulence Modelling and Measurements - ETMM7*, 2007.

[100] C. Rumsey. Successes and challenges for flow control simulations. In *AIAA 4th flow control conference*, 2008. AIAA-2008-4311.

[101] S. Saddoughi. Synthetic jet actuators, 2004.

[102] A. Santhanakrishnan, N. Pern, K. Ramakumar, A. Simpson, and J. Jacob. Enabling flow control technology for low speed uavs. In *5th Aviation, Technology, Integration, and Operations Conference*, 2005. AIAA-2005-6960.

[103] J. Schetz. *Boundary Layer Analysis*. Prentice Hall, 1993.

[104] L. Shampine and S. Thompson. Moving averages of solutions of odes. *Applied mathematics and computation*, 193:175–182, 2007.

[105] R. Sharma. Fluid-dynamic-based analytical model for synthetic jet actuation. *AIAA journal*, 45:1841, 2007.

[106] M. Shur, P. Spalart, M. Strelets, and A. Travin. Navier-stokes simulation of shedding turbulent flow past a circular cylinder and a cylinder with backward

splitter plate. In *Computational Fluid Dynamics'96*, 1996. Proceedings of the third ECCOMAS computational fluid dynamics conference.

[107] M. Shur, P Spalart, M. Strelets, and A. Travin. Detached-eddy simulation of an airfoil at high angle of attack. In *4th international symposium on engineering turbulence modelling and measurements*, pages 669–678, 1999.

[108] M. Shur, P. Spalart, M. Strelets, and A. Travin. A hybrid rans-les approach with delayed-des and wall-modelled les capabilities. *International journal of heat and fluid flow*, 29:1638–1649, 2008.

[109] J. Smagorinsky. General circulation experiments with the primitive equations. *Monthly weather review*, 91:99–164, 1963.

[110] B. Smith and A. Glezer. The formation and evolution of synthetic jets. *Physics of fluids*, 10:2281–2297, 1998.

[111] B. Smith and A. Glezer. Jet vectoring using synthetic jets. *Journal of Fluid Mechanics*, 458:1–34, 2002.

[112] P. Spalart. Strategies for turbulence modelling and simulations. *International journal of heat and fluid flow*, 21:252–263, 2000.

[113] P. Spalart. Young-person's guide to des grids. Technical Report CR-2001-211032, NASA, 2001.

[114] P. Spalart. Detached-eddy simulation. *Annual review of fluid mechanics*, 41:181–202, 2009.

[115] P. Spalart and R. Allmaras. A one-equation turbulence model for aerodynamics flows. *La Recherche Aerospatiale*, 1:5–21, 1994.

[116] P. Spalart, S. Deck, M. Shur, K Squires, M. Strelets, and A. Travin. A new version of des resistant to ambiguous grid densities. *Theoretical and computational fluid dynamics*, 2006.

[117] P. Spalart, L. Hedges, M. Shur, and A. Travin. Simulation of active flow control on a stalled airfoil. *Flow, turbulence and combustion*, 71:361–373, 2003.

[118] P. Spalart, W. Jou, M Strelets, and S. Allmaras. Comments on the feasibility of les for wings, and on a hybrid rans/les approach. In *Advances in DNS/LES*, pages 137–147, 1998. First AFSOR international conference on DNS/LES.

[119] K. Squires, J. Forsythe, S. Morton, D. Blake, M. Serrano, K. Wurtzler, W. Strang, R. Tomaro, and P. Spalart. Analysis of full aircraft with massive separation using detached-eddy simulation. In *Department of Defense High Performance Computing User Group Conference*, 2002.

[120] M. Strelets. Detached eddy simulation of massively separated flows. In *AIAA 39th Aerospace sciences meeting and exhibit*, 2001. AIAA-2001-0879.

[121] L. Tavares, P. Henriques, R. Utsch, M. Vinicius, and M. da Silva. Comparison between modern procedures for aerodynamic calculation of subsonic airfoils for application in light aircraft designs. In *18th International Congress of Mechanical Engineering*, 2005.

[122] A. Tchieu, A. Kutay, J. muse, A. Calise, and A. Leonard. Validation of a low-order model for closed-loop flow control enable flight. In *AIAA 4th flow control conference*, 2008. AIAA-2008-3863.

[123] D. Von Terzi, J. Frohlich, and I Mary. Zonal coupling of les with downstream rans calculations. Submitted to theoretical and computational fluid dynamics, 2006.

[124] J. Thompson, B. Soni, and N. Weatherill. *Handbook of grid generation*. CRC press, 2000.

[125] E. Touber and R. Moser. Modeling approach for a 2d synthetic jet. In *Bulletin of the American Physical Society - APS DFD 2006*, 2006.

[126] A. Travin, M. Shur, M. Strelets, and P. Spalart. Detached-eddy simulations past a circular cylinder. *Flow, turbulence and combustion*, 63:293–313, 1999.

[127] B. Twaites. Approximate calculation of the laminar boundary layer. *Aeronautical Quarterly*, 1:245–280, 1949.

[128] K. Squires U. Piomelli, E. Balaras and P. Spalart. Zonal approaches to wall-layer models for large-eddy simulations. In *AIAA 3th Theoretical fluid mechanics meeting*, 2002. AIAA-2002-3083.

[129] J. Vadillo and R. Agarwal. Numerical study of aerodynamic performance of airfoils at low angles of attack by active flow control of trailing edge vortices. *AIAA-2006-1058*, 2006.

189

[130] B. Vukasinovic and A. Glezer. Control of a separating flow over a turret. *AIAA paper 2007-4506*, 2007.

[131] M. Walsh and L. Weinstein. Drag and heat transfer on surfaces with small longitudinal fins. *AIAA paper 78-1161*, 1978.

[132] N. Yamaleev and M. Carpenter. Quasi-one dimensional model for realistic three dimensional synthetic jet actuators. *AIAA journal*, 44:208–216, 2006.

[133] D. You and P. Moin. Active control of flow separation over an airfoil using synthetic jets. *Journal of fluids and structures*, 24:1349–1357, 2008.

[134] P.J. Zwart. *The integrated space-time finite volume method*. PhD thesis, University of Waterloo, 1999.

Index

Vita

Omar Dario Lopez Mejia was born in Cartagena, Colombia on 28 February 1976. He received a Bachelor of Science degree in Mechanical Engineering from Universidad Industrial de Santander. After working for a couple of years in the Colombian industry, he decided to apply for graduate school at Universidad de los Andes where he finished his Msc degree in Mechanical engineering in 2001. After graduation he was hired as a full time professor of the mechanical engineering department at Universidad de los Andes where he worked for 3 years. In 2004, he was granted with a Fulbright scholarship and began his PhD at University of Texas at Austin.

Permanent address: Cra 19 N 29 c 72 Pie de la Popa
Cartagena, Colombia

This dissertation was typeset with LaTeX[†] by the author.

[†]LaTeX is a document preparation system developed by Leslie Lamport as a special version of Donald Knuth's TeX Program.